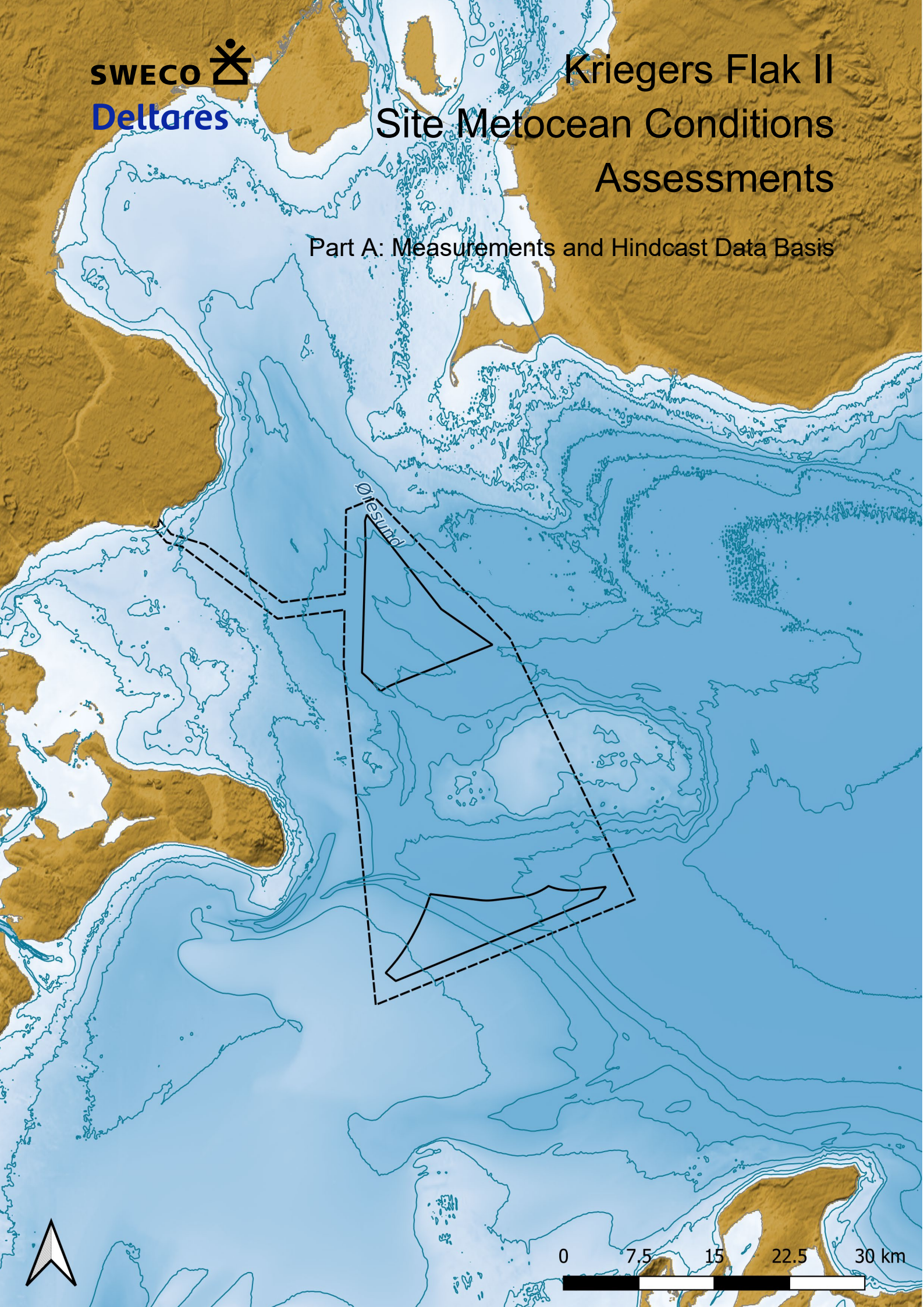




Kriegers Flak II Site Metocean Conditions Assessments

Part A: Measurements and Hindcast Data Basis



Change list

Ver	Date	Description of the change	Author	Reviewed	Approved by
1	2024-07-12	New Document	Bas Reijmerink, Antonios Emmanouil, Maria Georgiou, Marco Viteri Mendoza	Sofia Caires	Jan-Joost Schouten
2	2024-10-01	Revised to address review comments.			
3	2024-10-18	Revised to address final review comments.	Bas Reijmerink, Antonios Emmanouil, Maria Georgiou, Marco Viteri Mendoza	Sofia Caires 	Jan-Joost Schouten 

Project Name MetOcean Assessment for Kriegers
Flak II North and South

Project Manager Anders Helkjær, anders.helkjaer@sweco.dk, +4527233341

Client Energinet Eltransmission A/S

Author Bas Reijmerink, Antonios Emmanouil, Maria Georgiou, Marco Viteri Mendoza

Controlled by Sofia Caires

Approved by Jan-Joost Schouten

Date 2024-10-18

Ver 3

Document number 41011328B

Document reference 41011328B_KFII_PartA_Measurements_and_Hindcast_Data_Basis

Table of contents

1	Summary	15
2	Introduction.....	16
2.1	Background	16
2.2	Objectives	17
2.3	Approach	20
2.4	Report outline.....	22
3	Data basis.....	23
3.1	Measurement data	23
3.2	Wind and atmospheric data	25
3.2.1	Introduction	25
3.2.2	Wind downscaling.....	26
3.2.3	Conversion to hub-height	26
3.2.4	Data validation and calibration	27
3.2.5	The Kriegers Flak II North and South (KFII) OWF datasets	41
3.3	Hydrodynamic data	42
3.3.1	Introduction	42
3.3.2	Hydrodynamic modelling	43
3.3.3	Data validation and calibration	48
3.3.4	Determination of vertical current profiles and extension of the 3D data.....	72
3.3.5	Validation of temperature and salinity	76
3.3.6	The Kriegers Flak II North and South (KFII) OWF water level and current dataset	79
3.4	Wave data	80
3.4.1	Wave modelling	81
3.4.2	Data validation and calibration	86
3.4.3	The Kriegers Flak II North and South (KFII) OWF wave dataset.....	102
3.5	Climate change effects.....	103
3.6	Selection of reference locations.....	105
3.6.1	Kriegers Flak II North.....	106
3.6.2	Kriegers Flak II South	110
4	References	112
Appendix A Error statistics		115
	Introduction.....	115
	Linear variables	115
	Circular variables.....	115
	References	117
Appendix B Delft3D flexible mesh flow module.....		118
	General.....	118
	Vertical discretization	118
	References	119
Appendix B Description of SWAN		120
	General.....	120
	Drag coefficient.....	121
	Whitecapping.....	122

Numerics 123
References 123

List of Figures

Figure 2-1 Overview of the windfarm area Kriegers Flak II. The dashed line indicates the full data delivery area, and the hatched areas indicate the OWFs. 16

Figure 2-2 Overview of the reference locations within each OWF. The dashed line indicates the full data delivery area, and the full line indicate the OWFs. Contour lines are seabed levels in metres below MSL. 19

Figure 2-3 Bathymetrical survey data of the KFII OWF area. 21

Figure 3-1 Aerial overview of the considered observation stations. 23

Figure 3-2 Wind speed (top 9 panels) and direction (lower panel) density scatter comparisons between the KFII-1-LB observations at 12 m (converted to 10 m) and the downscaled ERA5 data at 10 m. The middle panel of the top 9 shows the omni-directional comparisons and the panels surrounding it show the comparisons for the corresponding directional sectors (from top left, clockwise: NW, N, NE, E, SE, S, SW and W). The symmetric fit to the data is given by the red dotted line and the linear fits through the data percentiles (blue pluses) is given by the dashed blue line. The statistics of the comparisons are printed in the panels. 29

Figure 3-3 Wind speed (top 9 panels) and direction (lower panel) density scatter comparisons between the KFII-1-LB observations at 150 m and the ERA5 data at 150 m. The middle panel of the top 9 shows the omni-directional comparisons and the panels surrounding it show the comparisons for the corresponding directional sectors (from top left, clockwise: NW, N, NE, E, SE, S, SW and W). 30

Figure 3-4 Wind speed (top 9 panels) and direction (lower panel) density scatter comparisons between the KFII-2-LB observations at 12 m (converted to 10 m) and the downscaled ERA5 data at 10 m. The middle panel of the top 9 shows the omni-directional comparisons and the panels surrounding it show the comparisons for the corresponding directional sectors (from top left, clockwise: NW, N, NE, E, SE, S, SW and W). 31

Figure 3-5 Wind speed (top 9 panels) and direction (lower panel) density scatter comparisons between the KFII-2-LB observations at 150 m and the ERA5 data at 150 m. The middle panel of the top 9 shows the omni-directional comparisons and the panels surrounding it show the comparisons for the corresponding directional sectors (from top left, clockwise: NW, N, NE, E, SE, S, SW and W). 32

Figure 3-6 Wind speed (top 9 panels) and direction (lower panel) density scatter comparisons between the BHI-1-LB observations at 4 m (converted to 10 m) and the downscaled ERA5 data at 10 m. The middle panel of the top 9 shows the omni-directional comparisons and the panels surrounding it show the comparisons for the corresponding directional sectors (from top left, clockwise: NW, N, NE, E, SE, S, SW and W). 33

Figure 3-7 Wind speed (top 9 panels) and direction (lower panel) density scatter comparisons between the BHII-1-LB observations at 4 m (converted to 10 m) and the downscaled ERA5 data at 10 m. The middle panel of the top 9 shows the omni-directional comparisons and the panels surrounding it show the comparisons for the corresponding directional sectors (from top left, clockwise: NW, N, NE, E, SE, S, SW and W). 34

Figure 3-8 Wind speed (top 9 panels) and direction (lower panel) density scatter comparisons between the FINO2 observations at 32 m (converted to 10 m) and the downscaled ERA5 data at 10 m. The middle panel of the top 9 shows the omni-directional comparisons and the panels surrounding it show the

comparisons for the corresponding directional sectors (from top left, clockwise: NW, N, NE, E, SE, S, SW and W). 35

Figure 3-9 Wind speed (top 9 panels) and direction (lower panel) density scatter comparisons between the FINO2 observations at 102/91 m and the ERA5 data at 102/91 m. The middle panel of the top 9 shows the omni-directional comparisons and the panels surrounding it show the comparisons for the corresponding directional sectors (from top left, clockwise: NW, N, NE, E, SE, S, SW and W). 36

Figure 3-10 Wind speed (top 9 panels) and direction (lower panel) density scatter comparisons between the Arkona Basin (AB) observations at 10 m and the downscaled ERA5 data at 10 m. The middle panel of the top 9 shows the omni-directional comparisons and the panels surrounding it show the comparisons for the corresponding directional sectors (from top left, clockwise: NW, N, NE, E, SE, S, SW and W). 37

Figure 3-11 Wind speed (top 9 panels) and direction (lower panel) density scatter comparisons between the Darsser-Sill (DS) observations at 9 m (converted to 10 m) and the downscaled ERA5 data at 10 m. The middle panel of the top 9 shows the omni-directional comparisons and the panels surrounding it show the comparisons for the corresponding directional sectors (from top left, clockwise: NW, N, NE, E, SE, S, SW and W). 38

Figure 3-12 Density scatter plots of atmospheric pressure at mean sea level (top left), air temperature (top right) and relative humidity (lower left) for ERA5 vs measurements at the Kriegers Flak II N buoy (KFII-2-LB). 40

Figure 3-13 Density scatter plots of atmospheric pressure at mean sea level (top left), air temperature (top right) and relative humidity (lower left) for ERA5 vs measurements at the Kriegers Flak II South buoy (KFII-1-LB). 41

Figure 3-14 Domain and bathymetry (top) and resolution (bottom) of the DCSM-FM model with Baltic extension. 44

Figure 3-15 Zoom in of the bathymetry (top) and resolution (bottom) of the DCSM-FM model with Baltic extension in the Kriegers Flak II North and South area. 45

Figure 3-16 Comparisons between the Køge and the 2DH model water levels. 49

Figure 3-17 Comparisons between the Rødvig and the 2DH model water levels. 49

Figure 3-18 Comparisons between the Skanör and the 2DH model water levels. 50

Figure 3-19 Comparisons between the FINO2 and the 2DH model water levels. 50

Figure 3-20 Comparisons between the KFII-1-LB and the 2DH model water levels. 50

Figure 3-21 Comparisons between the KFII-1-CP and the 2DH model water levels. 50

Figure 3-22 Comparisons between the BHI-1-LB and the 2DH model water levels. 51

Figure 3-23 Comparisons between the BHI-1-CP and the 2DH model water levels. 51

Figure 3-24 Comparisons between the BHII-1-LB and the 2DH model water levels. 51

Figure 3-25 Comparisons between the BHII-1-CP and the 2DH model water levels. 51

Figure 3-26 Comparisons between the Darsser-Sill and the 2DH model current speeds and directions. 53

Figure 3-27 Comparisons between the FINO2 and the 2DH model current speeds and directions.....	53
Figure 3-28 Comparisons between the KFII-1-LB and the 2DH model current speeds and directions.....	54
Figure 3-29 Comparisons between the KFII-1-CP and the 2DH model current speeds and directions.....	54
Figure 3-30 Comparisons between the KFII-2-LB and the 2DH model current speeds and directions.....	55
Figure 3-31 Comparisons between the KFII-2-CP and the 2DH model current speeds and directions.....	55
Figure 3-32 Comparisons between the Køge and the 3D model water levels. .	56
Figure 3-33 Comparisons between the Rødvig and the 3D model water levels.	56
Figure 3-34 Comparisons between the Skanör and the 3D model water levels.	57
Figure 3-35 Comparisons between the FINO2 and the 3D model water levels.	57
Figure 3-36 Comparisons between the KFII-1-LB and the 3D model water levels.....	57
Figure 3-37 Comparisons between the KFII-1-CP and the 3D model water levels.....	57
Figure 3-38 Comparisons between the KFII-2-LB and the 3D model water levels.....	58
Figure 3-39 Comparisons between the KFII-2-CP and the 3D model water levels.....	58
Figure 3-40 Comparisons between the BHI-1-LB and the 3D model water levels.	58
Figure 3-41 Comparisons between the BHI-1-CP and the 3D model water levels.....	58
Figure 3-42 Comparisons between the BHII-1-LB and the 3D model water levels.....	59
Figure 3-43 Comparisons between the BHII-1-CP and the 3D model water levels.....	59
Figure 3-44 Comparisons between the Darsser-Sill and the 3D model current speeds and directions (depth-averaged).....	61
Figure 3-45 Comparisons between the FINO2 and the 3D model current speeds and directions (depth-averaged).....	61
Figure 3-46 Comparisons between the KFII-1-LB and the 3D model current speeds and directions (depth-averaged).....	62
Figure 3-47 Comparisons between the KFII-1-CP and the 3D model current speeds and directions (depth-averaged).....	62
Figure 3-48 Comparisons between the KFII-2-LB and the 3D model current speeds and directions (depth-averaged).....	63
Figure 3-49 Comparisons between the KFII-2-CP and the 3D model current speeds and directions (depth-averaged).....	63
Figure 3-50 Comparisons between the Darsser-Sill and the 3D model current speeds and directions at 2 meters from surface (top) at 9 meters from surface (middle) and at 18 meters from surface (bottom).	65
Figure 3-51 Comparisons between the KFII-1-CP and the 3D model current speeds and directions at 4.5 meters from surface (top), at 18.5 meters from surface (middle) and at 35.5 meters from surface (bottom).	66
Figure 3-52 Comparisons between the KFII-2-CP and the 3D model current speeds and directions at 4.2 meters from surface (top), at 11.2 meters from surface (middle) and at 23.2 meters from surface (bottom).	67

Figure 3-53 Top panel: Current magnitude 3D profile plots comparisons between measurements (full lines) and calibrated 3D model results (dashed lines) at Darsser-Sill. Bottom panel: Comparisons between the corresponding depth-averaged current speeds..... 69

Figure 3-54 Top panels: Current magnitude 3D profile plots comparisons between measurements (full lines) and calibrated 3D model results (dashed lines) at KFII-1-CP (left) and KFII-2-CP (right). Bottom panels: Comparisons between the corresponding depth-averaged current speeds. 70

Figure 3-55 KFII-1-CP vertical current speed (left, ratio between the current speed of the layer and the depth-averaged current speed) and direction (middle, rotation between the current direction of the layer and the depth-averaged current direction) profiles and rose of the depth-averaged velocities (right). Only speeds above 0.05 are considered. 71

Figure 3-56 KFII-2-CP vertical current speed (left, ratio between the current speed of the layer and the depth-averaged current speed) and direction (middle, rotation between the current direction of the layer and the depth-averaged current direction) profiles and rose of the depth-averaged velocities (right). Only speeds above 0.05 are considered. 71

Figure 3-57 Darsser-Sill vertical current speed (left, ratio between the current speed of the layer and the depth-averaged current speed) and direction (middle, rotation between the current direction of the layer and the depth-averaged current direction) profiles and rose of the depth-averaged velocities (right). Only speeds above 0.05 are considered. 71

Figure 3-58 KFII-2 vertical current speed (left, ratio between the current speed of the layer and the depth-averaged current speed) and direction (middle, rotation between the current direction of the layer and the depth-averaged current direction) profiles and rose of the depth-averaged velocities (right). The top two panels show the results for the 2 directional sectors and depth-averaged current speed class 0.1-0.2 m/s and the bottom two panels show the results for the 2 directional sectors and depth-averaged current speed above 0.2 m/s. 74

Figure 3-59 KFII-2 vertical current speed (left, ratio between the current speed of the layer and the depth-averaged current speed) and direction (middle, rotation between the current direction of the layer and the depth-averaged current direction) profiles and rose of the depth-averaged velocities (right). The top two panels show the results for the 2 directional sectors and depth-averaged current speed class 0.1-0.2 m/s and the bottom two panels show the results for the 2 directional sectors and depth-averaged current speed above 0.2 m/s. 75

Figure 3-60 Hovmöller diagrams of the 3D temperature model results (background colour map) and near-bottom and near-surface temperature observations (coloured circles) from KFII-1-CP and KFII-1-LB, respectively, from 2023 (top panel) and 2024 (bottom panel)..... 76

Figure 3-61 Hovmöller diagrams of the 3D temperature model results (background colour map) and near-bottom and near-surface temperature observations (coloured circles) from KFII-2-CP and KFII-2-LB, respectively, from 2023 (top panel) and 2024 (bottom panel)..... 77

Figure 3-62 Hovmöller diagrams of the 3D model results (background colour map) and observations (coloured circles) of temperature (top) and salinity (bottom) at Arkona during 2014..... 78

Figure 3-63 Hovmöller diagrams of the 3D model results (background colour map) and observations (coloured circles) of temperature (top) and salinity (bottom) at Arkona during 2020..... 78

Figure 3-64 Hovmöller diagrams of the 3D model results (background colour map) and observations (coloured circles) of temperature (top) and salinity (bottom) at Darsser-Still during 2022..... 79

Figure 3-65 Computational SWAN wave model domain and grid. 82

Figure 3-66 Bed levels relative to MSL as used in the computational grid of the wave model including wave observation locations..... 83

Figure 3-67 Bed levels relative to MSL as used in the surroundings of KFII. Zoom of Figure 3-66 83

Figure 3-68 Density scatter comparisons (all data) between the buoy observations and the (raw) SWAN results at KFII-1-LB (Kriegers Flak II South OWF). Top left: significant wave height, top right: peak wave period, middle left: zero-crossing wave period (full frequency range, 0.03-1.0 Hz), middle right: mean wave direction, bottom left: zero-crossing wave period (limited frequency range, 0.04-0.5 Hz). The symmetric fit to the data is given by the red dotted line and the linear fit through the data percentiles (blue pluses) is given by the dashed blue line. The statistics of the comparisons are printed in the panels. . 89

Figure 3-69 Density scatter comparisons (all data) between the buoy observations and the (raw) SWAN results at KFII-2-LB (Kriegers Flak II North OWF). Top left: significant wave height, top right: peak wave period, middle left: zero-crossing wave period (full frequency range, 0.03-1.0 Hz), middle right: mean wave direction, bottom left: zero-crossing wave period (limited frequency range, 0.04-0.5 Hz)..... 90

Figure 3-70 Density scatter comparisons (all data) between the buoy observations and the (raw) SWAN results at KFII-3-LB (Kriegers Flak II North OWF). Top left: significant wave height, top right: peak wave period, bottom left: mean wave direction..... 91

Figure 3-71 Density scatter comparisons (all data) between the buoy observations and the (raw) SWAN results at KFI-WR (Kriegers Flak I OWF). Top left: significant wave height, top right: peak wave period, bottom left: zero-crossing wave period, bottom right: mean wave direction..... 92

Figure 3-72 Density scatter comparisons (all data) between the buoy observations and the (raw) SWAN results at BHI-1-LB. Top left: significant wave height, top right: peak wave period, bottom left: zero-crossing wave period, bottom right: mean wave direction..... 93

Figure 3-73 Density scatter comparisons (all data) between the buoy observations and the (raw) SWAN results at BHII-1-LB. Top left: significant wave height, top right: peak wave period, bottom left: zero-crossing wave period, bottom right: mean wave direction. 94

Figure 3-74 Density scatter comparisons (all data) between the buoy observations and the (raw) SWAN results at FINO2 (buoy). Top left: significant wave height, top right: peak wave period, bottom left: zero-crossing wave period, bottom right: mean wave direction. 95

Figure 3-75 Density scatter comparisons (all data) between the buoy observations and the (raw) SWAN results at FINO2 (wave radar). Top left: significant wave height, top right: peak wave period, bottom left: zero-crossing wave period. 96

Figure 3-76 Density scatter comparisons (all data) between the buoy observations and the (raw) SWAN results at Darsser-Schwelle. Top left: significant wave height, top right: peak wave period, bottom left: zero-crossing wave period, bottom right: mean wave direction. 97

Figure 3-77 Density scatter comparisons (all data) between the buoy observations and the (raw) SWAN results at Arkona. Top left: significant wave

height, top right: peak wave period, bottom left: zero-crossing wave period,
bottom right: mean wave direction..... 98

Figure 3-78 Density scatter comparisons (all data) between the buoy
observations and the corrected SWAN results at KFII-1-LB (Kriegers Flak II
South OWF). Top left: significant wave height, top right: peak wave period,
bottom left: zero-crossing wave period (full frequency range, 0.03-1.0 Hz),
bottom right: zero-crossing wave period (limited frequency range, 0.04-0.5 Hz).
..... 99

Figure 3-79 Density scatter comparisons (all data) between the buoy
observations and the corrected SWAN results at KFII-2-LB (Kriegers Flak II
North OWF). Top left: significant wave height, top right: peak wave period,
bottom left: zero-crossing wave period (full frequency range, 0.03-1.0 Hz),
bottom right: zero-crossing wave period (limited frequency range, 0.04-0.5 Hz).
..... 100

Figure 3-80 Density scatter comparisons (all data) between the buoy
observations and the corrected SWAN results at KFII-3-LB (Kriegers Flak II
North OWF). Left: significant wave height, right: peak wave period. 100

Figure 3-81 Timeseries of the observations and the raw and calibrated SWAN
output at KFII-1-LB during the Storm Babet (Oct. 2023). 101

Figure 3-82 Timeseries of the observations and the raw and calibrated SWAN
output at KFII-2-LB during the Storm Babet (Oct. 2023). 101

Figure 3-83 Comparison of raw wave spectral data at location KFII-1-LB during
the peak of storm Babet (20 October 2023). 102

Figure 3-84 Comparison of raw wave spectral data at location KFII-2-LB during
the peak of storm Babet (20 October 2023). 102

Figure 3-85 Global mean sea level change from 1900 to 2150, observed (1900–
2018) and projected under the SSP scenarios (2000–2150), relative to a 1995–
2014 baseline. Solid lines show median projections. Shaded regions show likely
ranges for SSP1-2.6 and SSP3-7.0. Dotted and dashed lines show respectively
the 83rd and 95th percentile low-confidence projections for SSP5-8.5. Bars on
the right show, left to right, likely ranges for SSP1-1.9, SSP1-2.6, SSP2-4.5,
SSP3-7.0, and SSP5-8.5 in 2150. Lightly shaded thick/thin bars show 17th–
83rd/5th–95th percentile low-confidence ranges in 2150 for SSP1-2.6 and SSP5-
8.5. Low-confidence range for SSP5-8.5 in 2150 extends to 4.8/5.4 m at the
83rd/95th percentile. (from: IPCC, 2021, Box TS.4, Figure 1a). 104

Figure 3-86 Sea level change (in m) relative to 2020 for the Kriegers Flak region
for SSP1-2.6, SSP2- 4.5, SSP3- 7.0 and SSP5- 8.5 according to IPCC (2021).
The full lines indicate the 50th percentiles and the shadows the 5th to 95th
percentile range. 104

Figure 3-87 95th Percentile of the significant wave height, H_s , of the hourly data
from 1979 until 2023 for Kriegers Flak II North OWF. 106

Figure 3-88 95th Percentile of the wave load proxy, $H_s \cdot \sqrt{T_p}$, of the hourly data
from 1979 until 2023 for Kriegers Flak II North OWF. 107

Figure 3-89 95th Percentile of the depth-averaged current speed, CS, of the
hourly data from 1979 until 2023 for Kriegers Flak II North OWF. 108

Figure 3-90 Selected reference locations Kriegers Flak II North OWF. 109

Figure 3-91 95th Percentile of the significant wave height, H_s , of the hourly data
from 1979 until 2023 for Kriegers Flak II South OWF. 110

Figure 3-92 95th Percentile of the wave load proxy, $H_s \cdot \sqrt{T_p}$, of the hourly data
from 1979 until 2023 for Kriegers Flak II South OWF. 110

Figure 3-93 95th Percentile of the depth-averaged current speed, CS, of the
hourly data from 1979 until 2023 for Kriegers Flak II South OWF. 111

Figure 3-94 Selected reference locations Kriegers Flak II South OWF. 111

List of Tables

Table 2-1 List of the reference points for the combined area for Kriegers Flak II North and South OWFs with name, coordinates and depth.	18
Table 3-1 Considered observation datasets.	24
Table 3-2 Considered observation datasets (continuation of Table 3-1).	25
Table 3-3 ERA5 wind speed calibration factors.	39
Table 3-4 Settings of the DCSM with Baltic extension model parameters.	47
Table 3-5 Water level statistics based on 2DH model results.	52
Table 3-6 Current magnitude statistics based on 2DH model results.	56
Table 3-7 Water level statistics based on 3D model results.	59
Table 3-8 Raw 3D model water level calibration factor.	60
Table 3-9 Depth averaged current magnitude statistics based on 3D model results.	64
Table 3-10 Raw 3D model current speed calibration factors.	72
Table 3-11 Raw wave model calibration factors.	88
Table 3-12 Overview of selected reference locations Kriegers Flak II North OWF.	108
Table 3-13 Overview of selected reference locations Kriegers Flak II South OWF.	111

Nomenclature

Variable	Abbreviation	Unit
Atmosphere		
Wind speed @ 10 m height	U_{10mag}	m/s
Wind direction @ 10 m height	U_{10dir}	°N (clockwise from)
Wind speed @ 150 m height	U_{150mag}	m/s
Wind direction @ 150 m height	U_{150dir}	°N (clockwise from)
Air pressure @ mean sea level	P	Pa
Air temperature @ 2 m height	T_{2m}	°C
Relative humidity @ 2 m height	RH	-
Surface solar radiation	SSR	J/m ²
Ocean		
Water level	WL or SWL	mMSL
Current speed	CS or u or $u_{yy,xx}$ (yy=total, tide, res, xx=level or DA)	m/s
Current direction	CD or u_{dir} or $u_{dir,yy,xx}$ (yy=total, tide, res, xx=level or DA)	°N (clockwise to)
Sea surface temperature	SST	°C
Water temperature @ {x} m depth	$T_{sw\{x\}}$	°C
Water Salinity	Salinity	PSU (practical salinity unit)
Waves		
Significant wave height	H_{m0} or H_s	m
Maximum wave height	H_{max}	m
Maximum wave crest height	C_{max}	m
Peak wave period	T_p	s
Wave energy period	T_{m10}	s
Mean wave period	T_{m01}	s
Zero-crossing wave period	T_{m02}	s
Wave period associated with the maximum wave height	T_{Hmax}	s
Peak wave direction	PWD	°N (clockwise from)
Mean wave direction	MWD	°N (clockwise from)
Direction standard deviation	DSpr	°

Definitions	
Coordinate System	WGS84 EPSG 4326 (unless specified differently)
Direction	Clockwise from North
Wind	°N coming from
Current	°N going to
Waves	°N coming from
Time	Times are relative to UTC
Vertical Datum	MSL (unless specified differently)
Statistics	
RMSE	root-mean-square error
ρ	correlation coefficient
σ	standard deviation
R	symmetric slope
n	sample size
Abbreviations	
2D	2-dimensional
3D	3-dimensional
DMI	Danish Meteorological Institute
DNV	Det Norske Veritas
ECMWF	European Centre for Medium-Range Weather Forecasts
EMODnet	The European Marine Observation and Data Network
ERA5	ECMWF Re-analysis v5
FEED	Front-End Engineering Design
IEC	International Electrotechnical Commission
ISO	International Organization for Standardization
KFII	Kriegers Flak II North and South
mMSL	Metres above Mean Sea Level
MSL	Mean Sea Level
OWF	Offshore Wind Farm
UTC	Coordinated Universal Time
WGS84	World Geodetic System 1984

1 Summary

The Danish Energy Agency has tasked Energinet (the Client) with undertaking site metocean conditions assessments for the development of the offshore wind farm areas Kriegers Flak II North and South. This report presents the derivation of the metocean data to be used as input in the assessments of the metocean site conditions.

The study involved downscaling of wind data and detailed high-resolution hydrodynamic and wave numerical modelling. The delivered data consist of validated and calibrated long term timeseries of atmospheric, hydrodynamic and wave data.

The data are categorized by spatial, temporal, and spectral dimensions and is delivered in two packages: one for detailed analysis at reference locations and another for a fine-gridded overview across the entire data delivery area.

2 Introduction

2.1 Background

The Danish Energy Agency has tasked Energinet (ENDK, the Client) with undertaking site metocean conditions assessments for the development of the offshore wind farm areas Kriegers Flak II North and South. The offshore wind farms are to be in the Southwestern part of the Baltic Sea east of Sjælland. An overview is shown in Figure 2-1.

The site metocean conditions assessments, which are to be certified, will form part of the larger site conditions assessment work (also including site wind and ice conditions assessments) and will be a part of the technical basis for the future public tender on the development of offshore wind farms within the areas. The site metocean conditions assessment must be suitable for the Front-End Engineering and Design (FEED) of offshore WTG and other support structures for the offshore wind farms.



Figure 2-1 Overview of the windfarm area Kriegers Flak II. The dashed line indicates the full data delivery area, and the hatched areas indicate the OWFs.

The full study consists of several deliverables:

- Part A: Description and Verification of Data Basis (this report).

- Part B: Data Analyses and Results (report).
- Long-term hindcast data (digital timeseries, delivered with Part A).
- Measurement data (digital timeseries).
- Hindcast revalidation note.

The study refers to the following common practices and guidelines:

- DNV-RP-C205
- IEC 61400-3-1

2.2 Objectives

The objective of Part A of the study is to provide the Client with metocean data to be used as input for their assessment of the MetOcean site conditions to support the design of the various structures within the area of KFII. For this a preliminary hub-height of 150 mMSL is considered. As requested by the Client, the main goal is to provide the following metocean data:

I. Hindcast timeseries at three reference locations per offshore wind farm (six in total) for a period of up to 45 years (01-01-1979 00:00 – 31-12-2023 23:00) with an hourly interval and including the following parameters:

- Wind: speed and direction at 10 m above MSL and at hub-height (150 m above MSL),
- Waves: significant wave height H_s , maximum wave height H_{max} , maximum wave crest height C_{max} , peak wave period T_p , wave energy period $T_{m-1,0}$, mean wave period $T_{m0,1}$, spectral zero-crossing wave period $T_{m0,2}$, peak wave direction PWD, mean wave direction MWD, one-sided directional spreading (standard deviation) DSpr;
- Water level WL (total, tidal and residual);
- Current speed CS and current direction CD (total, tidal and residual) at near-surface, near-bottom and mid-depth;
- Current speed CS and current direction CD (total only) at all depth layers;
- Sea water parameters: temperature and salinity at all depth layers (10 years only, 2014 to 2023);
- Atmospheric parameters: air temperature at 2m T_{2m} , surface air pressure P, surface solar radiation SSR and relative humidity RH (one point per offshore wind farm).

II. Hindcast timeseries on a mesh within the data delivery area covering the KFII OWFs for a period of up to 45 years (01-01-1979 00:00 – 31-12-2023 23:00) with an hourly interval and including the following parameters:

- Wind: speed and direction at 10 m above MSL (0.005°E by 0.0025°N);
- Waves: significant wave height H_s , maximum wave height H_{max} , maximum wave crest height C_{max} , peak wave period T_p , wave energy period $T_{m-1,0}$, mean wave period $T_{m0,1}$, spectral zero-crossing wave period $T_{m0,2}$, peak wave direction PWD, mean wave direction MWD, one-sided directional spreading (standard deviation) DSpr (0.005°E by 0.0025°N);

- Water level WL (total, tidal and surge) (0.005°E by 0.0025°N);
- Current speed CS and current direction CD (total only) at all depth layers (0.005°E by 0.0025°N);
- Sea water parameters: temperature and salinity at all depth layers (0.005°E by 0.0025°N, 10 years only, 2014 to 2023);
- Atmospheric parameters: air temperature at 2m T_{2m} , surface air pressure P, surface solar radiation SSR and relative humidity RH (0.1°E by 0.1°N).

III. Assessment of climate change effects on the metocean conditions.

For KFII six reference locations have been chosen in agreement between Deltares, Sweco and the Client. The selection of the reference locations was made aiming at a reasonable spatial coverage of in the OWF areas and considering the most severe conditions. Namely, the variations in H_s , T_p and CS across each OWF area, with most attention towards their 95th percentile value in the time domain. Details on the selection assessment, including spatial variation plots, are presented in Section 3.6. The chosen 6 reference locations are listed in Table 2-1 and their location is shown in the overview map given in Figure 2-2.

Table 2-1 List of the reference points for the combined area for Kriegers Flak II North and South OWFs with name, coordinates and depth.

Reference location	Latitude WGS84 [°N]	Longitude WGS84 [°E]	Seabed level [mMSL]
KFIIS-1	54.9197	12.9998	-39.71
KFIIS-2	54.9200	12.7802	-31.40
KFIIS-3	54.8498	12.7096	-18.43
KFIIN-1	55.1252	12.8199	-32.02
KFIIN-2	55.2345	12.6905	-23.69
KFIIN-3	55.0940	12.6997	-29.66

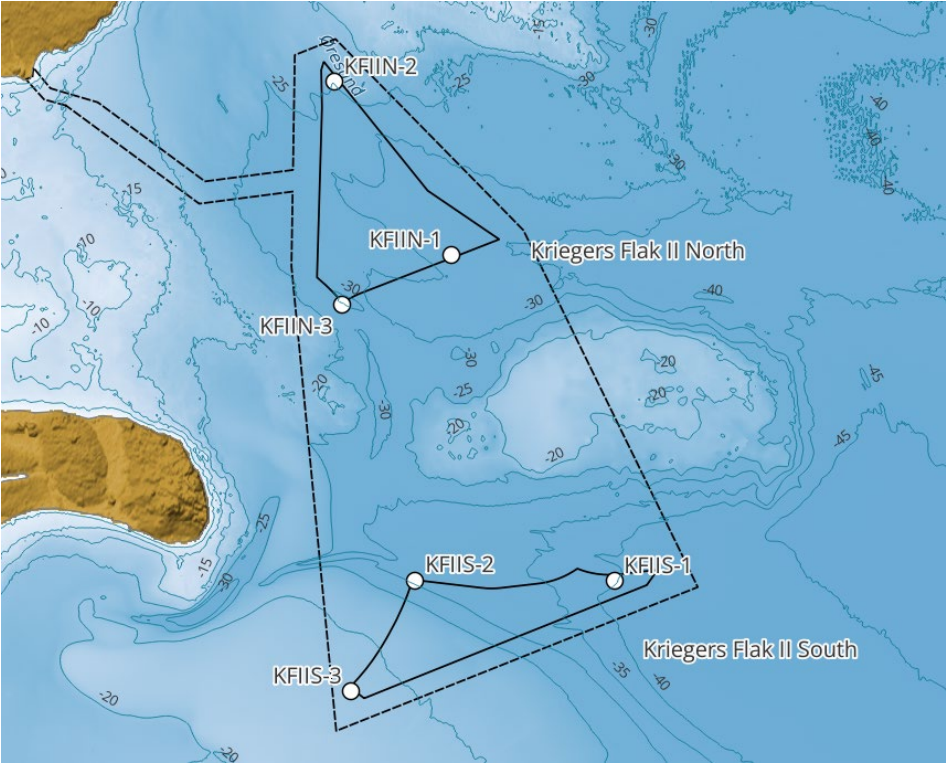


Figure 2-2 Overview of the reference locations within each OWF. The dashed line indicates the full data delivery area, and the full line indicate the OWFs. Contour lines are seabed levels in metres below MSL.

2.3 Approach

In order to fulfil the study objectives, the following activities have been carried out:

- Activity 1 – Retrieval, downscaling and validation of the atmospheric data,
- Activity 2 – Hydrodynamic modelling and
- Activity 3 – Wave modelling.

The determination of the metocean timeseries is based on available hindcast, reanalysis, climate projection and observation datasets, detailed numerical modelling, validation and post-processing.

Numerical modelling

Detailed numerical modelling has been carried out to derive the requested timeseries of wave, hydrodynamic (including water property) parameters. The hydrodynamics (water levels, currents, salinity, water temperature and water density) have been modelled using a locally adjusted version of the Deltares' 3D/2DH Dutch Continental Shelf Flexile Mesh (DCSM-FM) hydrodynamic model with Baltic extension and the waves have been modelled with a purposely built high-resolution model covering the KFII area using the shallow-water phase-averaging wave model SWAN. The models have been validated and calibrated using observations made available by the Client and from public sources. Both the hydrodynamic and the wave model results have been output hourly at the output locations for further assessments. In total 9,324 (9,328 overall + 6 reference) output locations are considered in the KFII area.

Data sources

The atmospheric data and boundary wave conditions needed to force the wave and hydrodynamic models were retrieved from the dataset of the most recent and accurate reanalysis of the European Centre for Medium-range Weather Forecast (ECMWF), ERA5. The ERA5 dataset currently covers the period from 1950 until now on a global model grid of about 0.25° x 0.25° (~30 km) at an hourly interval and has unprecedented accuracy in terms global atmospheric and wave data. The data from 1950 until 1978 are considered to be of lower quality than the data after that period given that more observations are available from 1979 for the applied data assimilation. In this study therefore the higher quality data from 01-01-1979 00:00 – 31-12-2023 23:00 are used.

Data from the Copernicus CMEMS Global Forecast¹ and Baltic Sea Reanalysis² datasets (CMEMS, 2021a,b) were used as boundary conditions for the hydrodynamic model .

Observation data (wind, atmospheric, wave, hydrodynamics and seawater properties) from measurement campaigns (e.g. Fugro, 2023a,b), which have been made available by the Client, and public data, available from the various BSH databases³ and the Copernicus Marine In Situ portal⁴, were used to validate and calibrate the metocean model data.

¹ <https://doi.org/10.48670/moi-00016>

² <https://doi.org/10.48670/moi-00013>

³ <https://login.bsh.de/fachverfahren/>

⁴ <https://marineinsitu.eu/dashboard/>

Intergovernmental Panel on Climate Change (IPCC⁵) provides a comprehensive summary on the current state of knowledge about the environmental consequences of projected climate change. Data from IPCC's newest Assessment Report (AR6) forms the basis for the assessment of sea level rise, sea water temperature changes and their potential effects on the metocean conditions.

The bathymetry data that were used as basis for the depth schematization of the hydrodynamic and wave models are from bathymetrical survey datasets provided by the Client (GEOxyz, 2024 and Ramboll, 2013a,b), see Figure 2-3, supplemented by the publicly available bathymetry dataset of the European Marine Observation and Data Network, EMODnet⁶ from 2022.

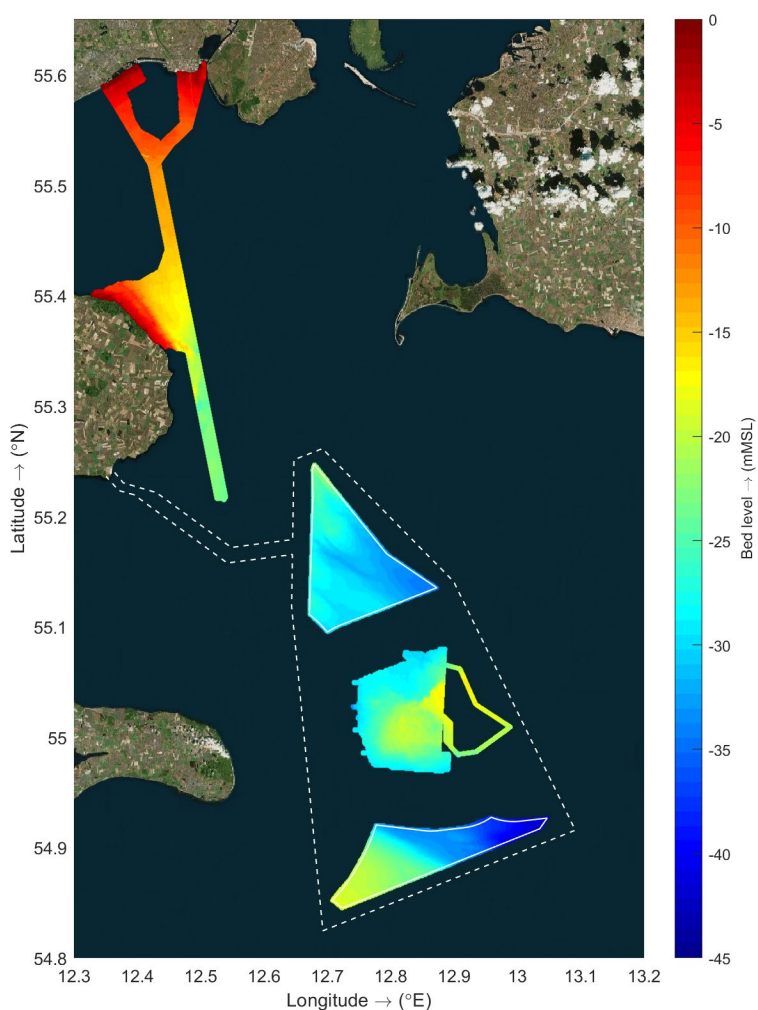


Figure 2-3 Bathymetrical survey data of the KFII OWF area.

⁵ <https://www.ipcc.ch/>

⁶ <http://portal.emodnet-bathymetry.eu/>

2.4 Report outline

The next chapter describes the data basis. The chapter contains 6 main sections. The first section presents the considered measurement data. Section 3.2 presents the wind and atmospheric data, focusing on the data validation and the downscaling and conversion of the wind data. Section 3.3 focuses on the description and validation of the hydrodynamic modelling and 3.4 on the description and validation of the wave modelling. Section 3.5 presents an overview of the projected effects of climate change in the winds, waves and hydrodynamics of the area. The chapter ends with the selection of the reference locations in Section 3.6. Within each wind farm, three locations are chosen for the detailed analysis of the metocean data and determination of the metocean conditions in Part B (SWECO, 2024) of the study.

A detailed description of the considered error statistic, of the hydrodynamic model and of the wave model is given in appendices A, B and C, respectively.

3 Data basis

3.1 Measurement data

In this section an overview is given of all observation datasets considered within this study for validation of the numerically derived data. In Table 3-1 and Table 3-2 an overview is given of the considered locations and observation datasets (including the periods covered by the datasets and their provenience). Figure 3-1 shows an aerial overview of the locations of the considered observation datasets.



Figure 3-1 Aerial overview of the considered observation stations.

Table 3-1 Considered observation datasets.

Station	Considered variables and sensors	Period	Reference/owner
KFII-1-LB	<i>Wind</i> : ZephIR ZX300M CW LiDAR (heights 12 m and 150 m, 10-min interval) <i>Air pressure</i> : Vaisala PTB330A (10-min interval) <i>Air temperature and relative humidity</i> : Vaisala HMP155 (10-min interval) <i>WL (bottom pressure)</i> : Thelma Biotel TBR700 (10-min interval) <i>Current</i> : Nortek Aquadopp 400 kHz (multiple levels, 10 min interval) <i>Waves</i> : Wavesense 3 (H_s , T_p , $T_{m0,2}$, MWD, 10-min interval ⁷)	09-2023 – 02-2024	Fugro (2023a)
KFII-1-CP	<i>WL (Bottom pressure) and Current</i> : Nortek Signature 500, (multiple levels, 10-min interval)	09-2023 – 04-2024	
KFII-2-LB	<i>Wind</i> : ZephIR ZX300M CW LiDAR (heights 12 m and 150 m, 10-min interval) <i>Air pressure</i> : Vaisala PTB330A (10-min interval) <i>Air temperature and relative humidity</i> : Vaisala HMP155 (10-min interval) <i>Current</i> : Nortek Aquadopp 400 kHz (multiple levels, 10 min interval) <i>Waves</i> : Wavesense 3 (H_s , T_p , $T_{m0,2}$, MWD, 10-min interval ⁷)	09-2023 – 02-2024	
KFII-2-CP	<i>Current</i> : Nortek Signature 500, (multiple levels, 10-min interval)	09-2023 – 03-2024	
KFII-3-LB	<i>Waves</i> : Wavesense 3 (H_s , T_p , $T_{m0,2}$, MWD, 10-min interval ⁷)	11-2023 – 12-2023	
BHI-1-LB	<i>Wind</i> : Gill Windsonic M acoustic wind sensor (height 4 m, 10-min interval) <i>WL (bottom pressure)</i> : Thelma Biotel TBR700 (10-min interval) <i>Current</i> : Nortek Aquadopp 600 kHz (multiple levels, 10 min interval) <i>Waves</i> : Wavesense 3 (H_s , T_p , $T_{m0,2}$, MWD, 10-min interval ⁷)	11-2021 – 11-2022	Fugro (2023b)
BHI-1-CP	<i>WL (Bottom pressure)</i> : Nortek Signature 500, (multiple levels, 10-min interval)	02-2022 – 11-2022	
BHII-1-LB	<i>Wind</i> : Gill Windsonic M acoustic wind sensor (height 4 m, 10-min interval) <i>WL (bottom pressure)</i> : Thelma Biotel TBR700 (10-min interval) <i>Current</i> : Nortek Aquadopp 600 kHz (multiple levels, 10 min interval) <i>Waves</i> : Wavesense 3 (H_s , T_p , $T_{m0,2}$, MWD, 10-min interval ⁷)	11-2021 – 11-2023	
BHII-1-CP	<i>WL (Bottom pressure)</i> : Nortek Signature 500, (multiple levels, 10-min interval)	11-2021 – 11-2023	
KFI-WR	<i>Waves</i> : Datawell Wave Rider (H_s , T_p , $T_{m0,2}$, MWD, 30-min interval)	03-2020– 05-2022	Vattenfall

⁷ Based on the spectral analysis of 17.06 min records.

Table 3-2 Considered observation datasets (continuation of Table 3-1).

Station	Considered variables and sensors	Period	Reference/owner
FINO2	<i>Wind</i> : Cup anemometer (heights 32 m and 102 m, 1h interval) <i>WL and Current</i> : Bottom mounted ADCP (multiple levels, 10-min interval) <i>Waves</i> : Separate wave buoy (H_s , T_p , $T_{m0,2}$, MWD, 30-min interval) and Wave radar (H_s , T_p , $T_{m0,2}$, MWD, 1-min interval)	12-2007 – 12-2023 (varies per sensor)	BSH Insitu data portal
Arkona Basin	<i>Wind</i> : Cup anemometer (height 10 m, 1h interval) <i>Waves</i> : Separate wave buoy (H_s , T_p , $T_{m0,2}$, MWD, 30-min interval)	02-2002 – 04-2024 (varies per sensor)	
Darsser Sill/Schwelle	<i>Wind</i> : Cup anemometer (height 9 m, 1h interval) <i>Current</i> : Bottom mounted ADCP (multiple levels, 1h interval) <i>Waves</i> : Separate wave buoy (H_s , T_p , $T_{m0,2}$, MWD, 30-min interval)	01-1995 – 04-2024 (varies per sensor)	
Køge	<i>WL</i> : Tide station (1h interval)	01-2012 – 02-2022	Copernicus Marine Service (In Situ) data portal
Rødvig	<i>WL</i> : Tide station (1h interval)	08-1991 – 12-2022	
Skanör	<i>WL</i> : Tide station (1h interval)	02-1992 – 12-2022	

3.2 Wind and atmospheric data

3.2.1 Introduction

In this section the data sources for wind speed and wind direction and other atmospheric data are described in more detail. These data are validated and (when deemed necessary) calibrated against the KFII-1-LB and KFII-2-LB measurements to arrive at the wind and atmospheric datasets for the KFII OWF area which formed the input for the analyses described in the report of Part B (SWECO, 2024) of the study (SWECO, 2024). The wind and atmospheric data used as basis for this study are from the ERA5 dataset. The hourly, 1-hour averaged data from 1979 until 2023 (45 years) were downloaded from the ERA5 repository in NetCDF format.

For input to the hydrodynamic model (Section 3.3), the wave model (Section 3.4) and for the wind data validation and calibration discussed in this section, ERA5 wind data at 10 m height and atmospheric data (air pressure, relative humidity, air temperature at 2m height and solar radiation) were downloaded for the region going from 15°W to 31°E and from 41.5°N to 67°N with a resolution of 0.1° x 0.1°⁸. Furthermore, for different vertical levels in the OWF areas ERA5 data were also downloaded. Namely, wind velocities at 100 m level, as well as at the heights of the 875, 900, 925, 950, 975 and 1000 hPa pressure layers. The retrieved ERA5 wind velocity components have been converted to wind

⁸ The resolution at which data are available from ERA5 for downloading is 0.25° by 0.25°. The interpolation to the 0.1° by 0.1° resolution is done by internal procedures on the ECMWF servers before downloading. It should be noted that the native model resolution of ERA5 is about 0.3° by 0.3°.

speed and direction⁹, and for each timestep the height of the pressure layers was also determined.

3.2.2 Wind downscaling

In order to force the wave model, open water 10 metre wind speeds are needed. However, given the topography of the area and the native resolution of the ERA5 atmospheric model, about 0.3° x 0.3°, the retrieved ERA5 10 metre wind data above water are at certain locations still affected by the land roughness, as the data are being interpolated into a grid of 0.1° x 0.1° from model 0.3° x 0.3° grid points above land or with partial land coverage. The retrieved hourly raw ERA5 10 m wind speeds on a spatial grid of 0.1° x 0.1° have been downscaled to open water by means of a 1-layer model assuming a blending height of 60 m (Caires et al., 2012). The surface roughness of the raw ERA5 data from a location with a land-sea mask value of 1 (land) has been assumed to be 25 cm and to decrease linearly to 3 mm for a land-sea mask value of 0 (open-water). The roughness correction is only applied when the land-sea-mask value is above zero, with the respective hourly wind speeds being adjusted from the determined roughness to an open water roughness of 3 mm.

3.2.3 Conversion to hub-height

Except at the 10 m and 100 m levels, the ERA5 wind data are not directly available at fixed vertical levels but at pressure levels¹⁰. Next to the data at the fixed levels, wind data were therefore also downloaded at various pressure levels (1000, 975, 950, 925, 900 and 875 hPa). The retrieved ERA5 wind velocity components were converted to wind speed and direction. In order to interpolate the wind speed data to the vertical levels at which the observations are available and to hub height, it is first necessary to determine the hourly heights (vertical levels) of the pressure levels. These are determined using:

$$h = h_b + \frac{T_b}{L_b} \left[\left(\frac{P}{P_b} \right)^{\frac{-R \cdot L_b}{g \cdot M}} - 1 \right]$$

where, h is the height above sea level in m, h_b is height at the bottom of the 2 m atmospheric layer, P is the atmospheric pressure at pressure level in hPa, P_b is the atmospheric pressure at sea level in hPa, T_b is the temperature at sea level in K, L_b is the standard temperature lapse rate, equal to -0.0065 K/m, R is the universal gas constant, equal to 8.31432 (Nm/molK), g is the acceleration of gravity, equal to 9.81 (m/s²) and M is the molar mass of Earth's air, equal to 0.0289644 (kg/mol). Using the ERA5 timeseries of P, P_b and T_b, the hourly timeseries of the heights corresponding to the pressure levels are determined using the expression above. On average there is the following correspondence between levels: 1,000 hPa ≈ 110 m, 975 hPa ≈ 328 m, 950 hPa ≈ 552 m, 925 hPa ≈ 780 m, 900 hPa ≈ 1,012 m and 875 hPa ≈ 1,250 m. The ERA5 wind

⁹ Using the nautical convention, i.e. the direction the wind is coming from in degrees clockwise from the North and referred to as °N. The direction of wind blowing from the North is 0°N, from the East is 90°N, from the South is 180°N and from the West is 270°N.

¹⁰ Wind data at the native model layers (fixed heights) can theoretically be downloaded from the ECMWF archive server, however this server is very slow and it was considered too inefficient to download the data there for the requested period of 45 years within the available time frame of the project.

speeds at the hub height and observation levels are determined by means of linear interpolation of the values at the adjacent levels.

In the next section the validation and calibration of the ERA5 wind data are presented.

3.2.4 Data validation and calibration

3.2.4.1 Wind

The ERA5 10 m (downscaled) and 150 m wind speed and direction data were validated against available wind speed and direction observations (10-min averages) from the floating LiDAR buoys (150 m and 12 m) that are currently deployed in the Kriegers Flak II areas during a one-year measurement campaign. Furthermore, the ERA5 10 m (downscaled), 150 and 102 m wind speed and 10 m, 150 m and 91 m direction data were validated against observation data at the BSH FINO2 metmast (102, 91 and 32 m). Last the ERA5 10 m (downscaled) wind speed and direction data were validated against observation data at Arkona Basin (10 m), Darsser-Sill (9 m), BHI-1-LB (4 m) and BHII-1-LB (4 m). An overview of the considered wind observation datasets is given in Table 3-1 and Table 3-2.

Before being applied, all wind observation data were first quality controlled. This means that data gaps were filled with dummy values and outliers to the data were removed from the data based on deviations from the (running) mean and standard deviations over a period of about a month. All quality-checked wind observation data were subsequently converted to hourly-averaged data by averaging the 10-min averages from 50 minutes before the hour until the hour.

Furthermore, for the validation of the 10 m downscaled model data, the observed wind speed data from the lowest (or only) observation levels (32, 12, 9 and 4 m) were converted to 10 m height assuming a neutral wind profile (Komen et al, 1994). This profile has been chosen, instead of extrapolating the observations from the measured levels, because the 10 m level is below and relatively close to the lowest LiDAR observation levels.

The near-surface vertical logarithmic wind profile is given by:

$$U(z) = \frac{u_x}{\kappa} \ln\left(\frac{z}{z_0}\right), \quad \text{with } z_0 = \alpha \frac{u_x^2}{g}, \quad z_0 = \alpha \frac{u_x^2}{g} \text{ and}$$

where z is the height, u_x is the friction velocity in m/s, z_0 is the surface roughness in m, κ is the von Karman constant, $g = 9.81 \text{ m/s}^2$ is the acceleration due to gravity and α is the Charnock 'constant'. An iterative algorithm or the approximation of Wu (1982) can be used to determine the friction velocity from the measurements. Hereafter, the corresponding wind velocity at 10 m (U_{10}) can be computed. There are different estimates for α available in the literature varying from 0.004 to 0.032 (see e.g. Komen et al., 1994). In line with other projects and as is also done in the modelling, α is set equal to 0.018. Assuming that the wind directions vary little over the lower levels of the vertical profile, the wind directions at 10 m have been assumed to be equal to the wind directions at the lower observation levels.

Figure 3-2 and Figure 3-3 (Figure 3-4 and Figure 3-5) show the density scatter (darker colours indicating higher data density) and percentile comparisons and the main statistics of the data comparisons such as the correlation coefficient,

root-mean-square errors, bias and standard deviation between the hourly ERA5 and KFII-1-LB (KFII-2-LB) data at 10 m and at 150 m, respectively. See Appendix A for a description of how these statistics were computed. In this and all other density scatter plots in this report, the presented statistics depend on whether linear (speeds, heights and periods) or circular (directions) variables are plotted. In the plots of circular variables, such as the bottom panel of Figure 3-2, no linear fits are given. In the plots of linear variables, such as the top panels of Figure 3-2 two fits are given: a symmetric fit (red dotted line) to the whole data (plotted in terms of density) and a linear fit (dashed blue line) through the data percentiles (the blue pluses, with each one corresponding to one percentile pair, 101 pluses in total, indicating the 1.00th to the 99.00th with increases of 1 and the 99.90th and the 99.99th). The red line provides an indication of the relation between the bulk of the data. The symmetric slope is given as it provides a direct measure of the (percentage of) over- or underestimation. The blue line provides an indication of the linear relation between the data extremes, with the considered percentiles being the plotted 1st to the 99.99th. For the relation between the percentiles the symmetric slope is not shown as the intersect is often different from zero and the linear relation between the percentiles is often used in the data calibration. Figure 3-6 to Figure 3-11 do the same for the other locations/heights listed in Table 3-1 and Table 3-2.

In this section an overview is given of all observation datasets considered within this study for validation of the numerically derived data. In Table 3-1 and Table 3-2 an overview is given of the considered locations and observation datasets (including the periods covered by the datasets and their provenience). Figure 3-1 shows an aerial overview of the locations of the considered observation datasets.

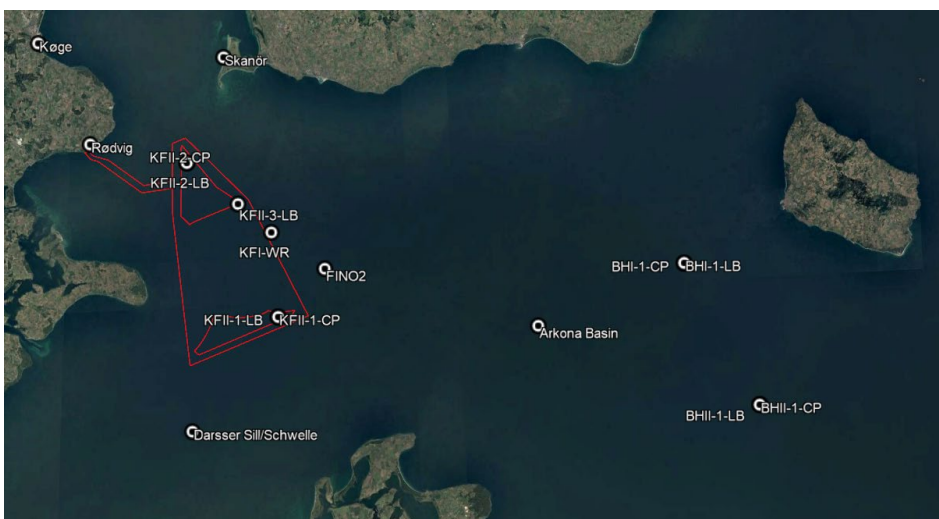


Figure 3-1 Aerial overview of the considered observation stations.

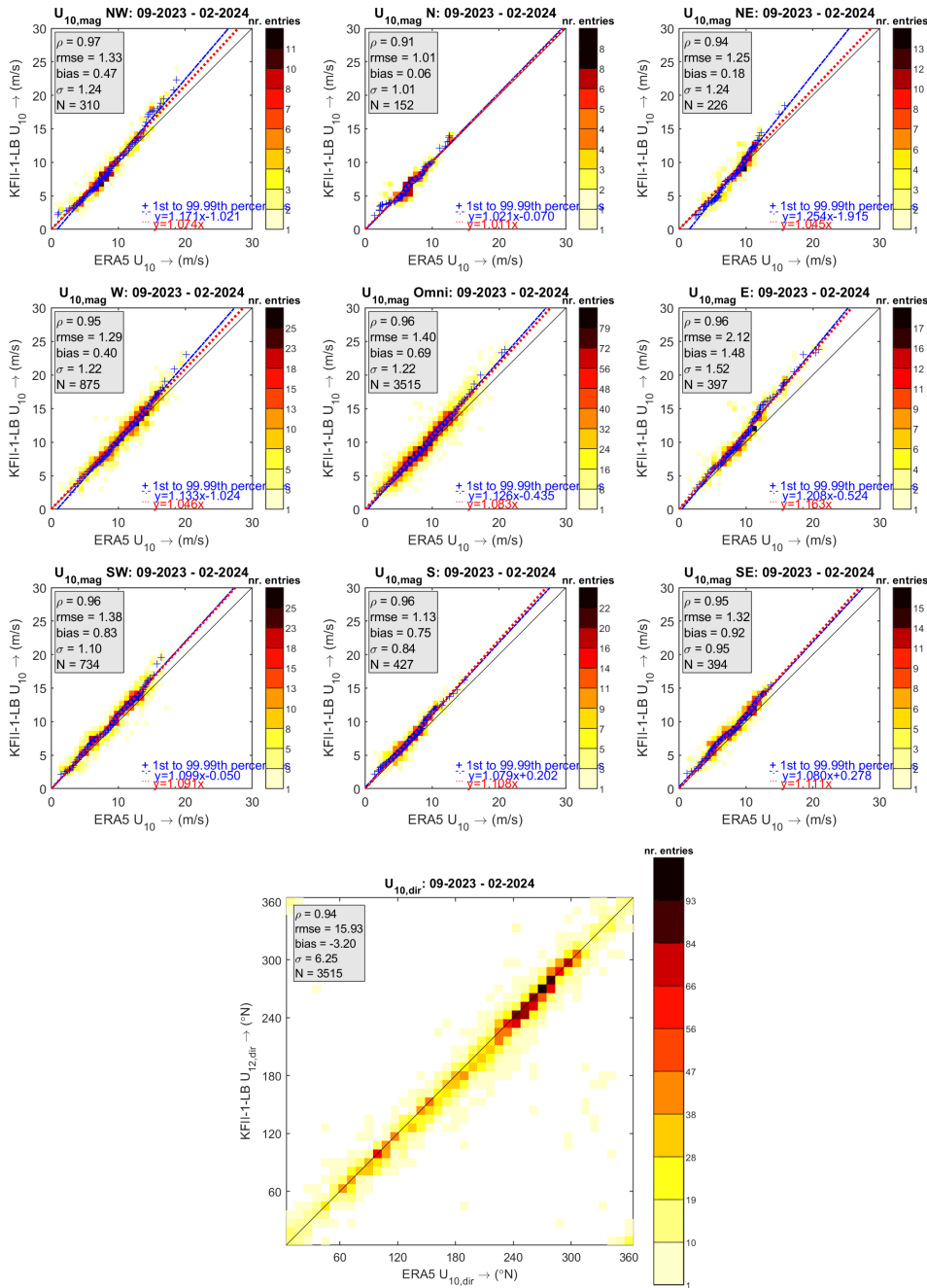


Figure 3-2 Wind speed (top 9 panels) and direction (lower panel) density scatter comparisons between the KFIIL-1-LB observations at 12 m (converted to 10 m) and the downscaled ERA5 data at 10 m. The middle panel of the top 9 shows the omni-directional comparisons and the panels surrounding it show the comparisons for the corresponding directional sectors (from top left, clockwise: NW, N, NE, E, SE, S, SW and W). The symmetric fit to the data is given by the red dotted line and the linear fits through the data percentiles (blue pluses) is given by the dashed blue line. The statistics of the comparisons are printed in the panels.

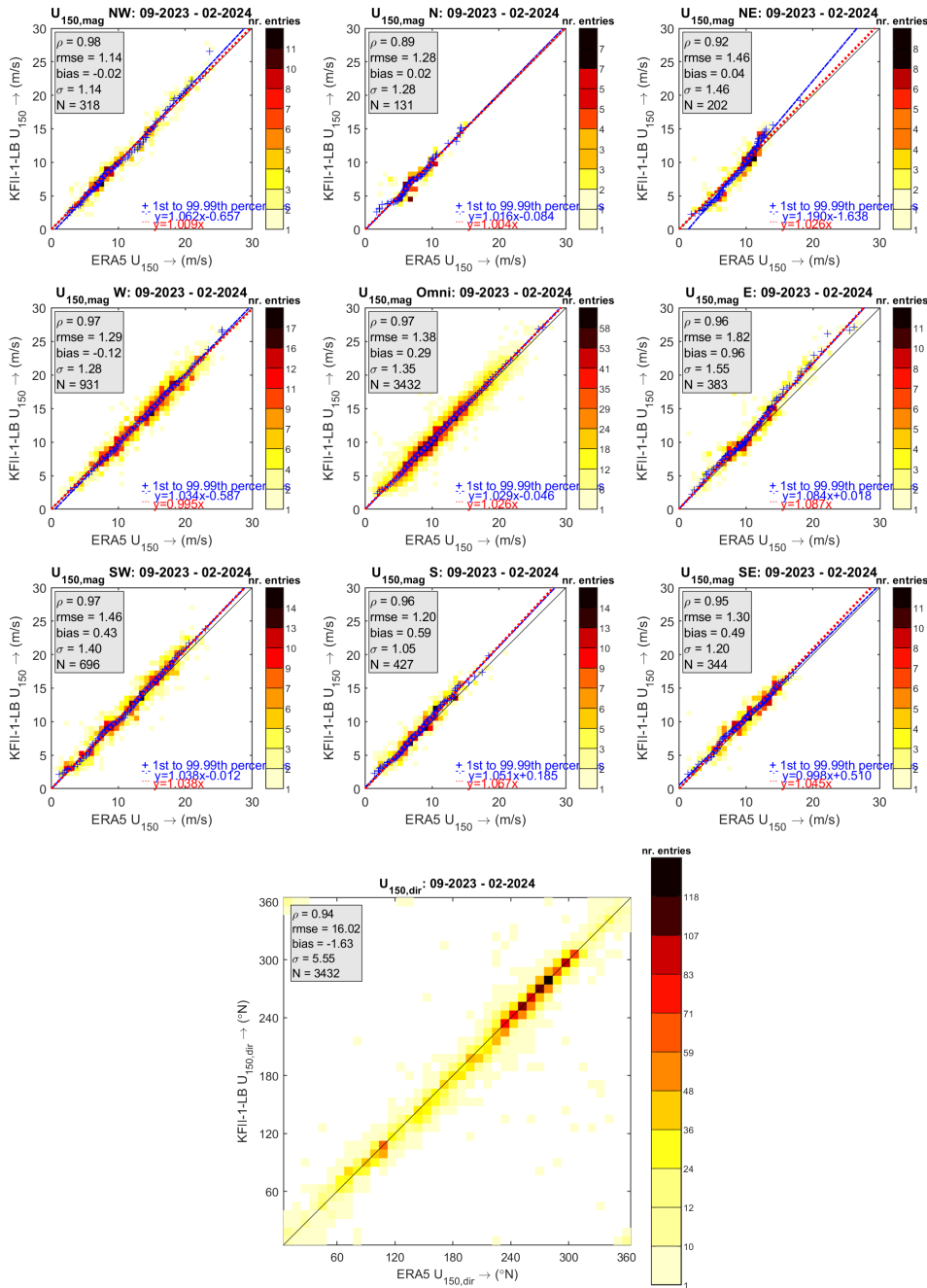


Figure 3-3 Wind speed (top 9 panels) and direction (lower panel) density scatter comparisons between the KFI1-1-LB observations at 150 m and the ERA5 data at 150 m. The middle panel of the top 9 shows the omni-directional comparisons and the panels surrounding it show the comparisons for the corresponding directional sectors (from top left, clockwise: NW, N, NE, E, SE, S, SW and W).

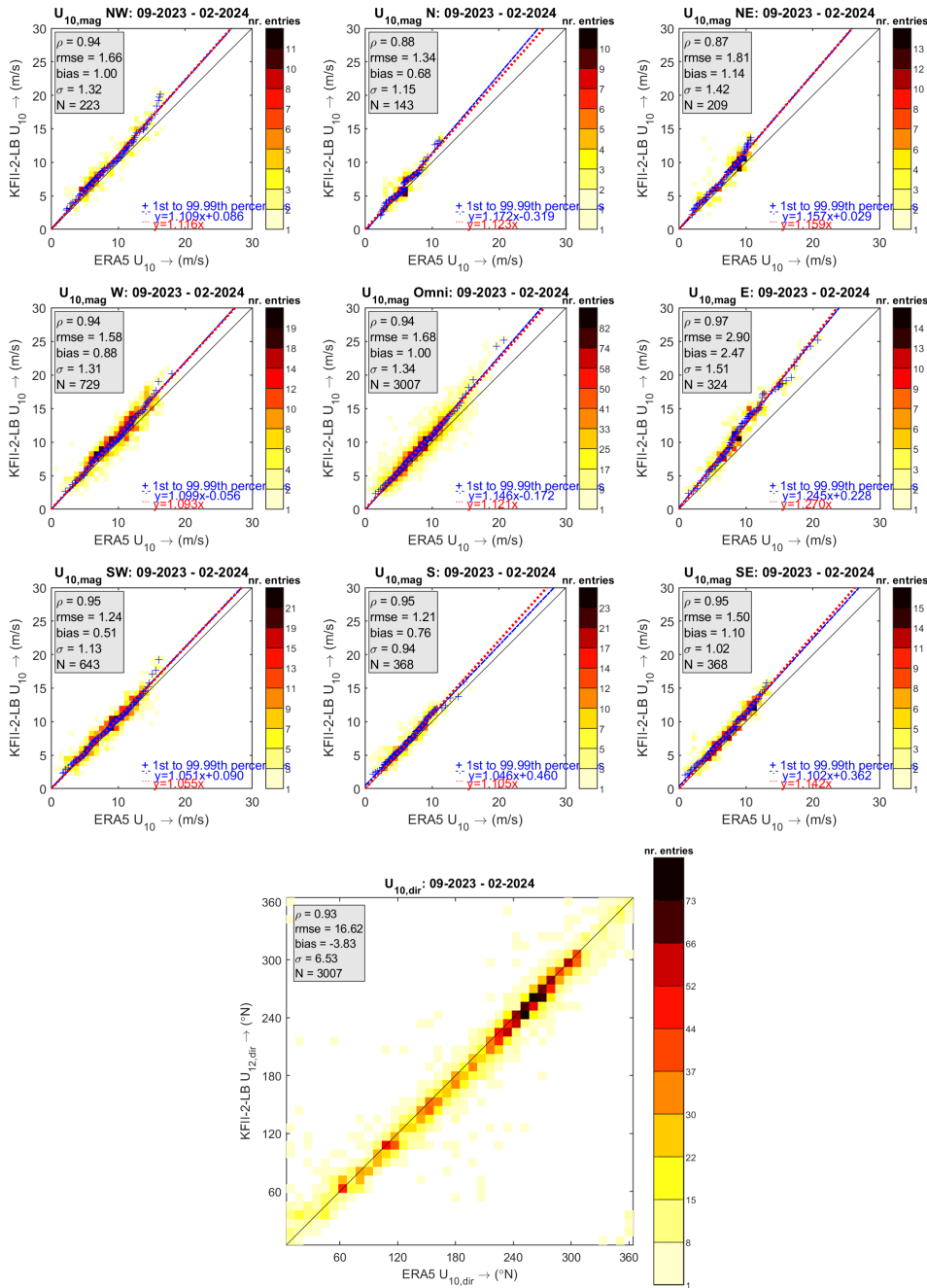


Figure 3-4 Wind speed (top 9 panels) and direction (lower panel) density scatter comparisons between the KFI|2-LB observations at 12 m (converted to 10 m) and the downscaled ERA5 data at 10 m. The middle panel of the top 9 shows the omni-directional comparisons and the panels surrounding it show the comparisons for the corresponding directional sectors (from top left, clockwise: NW, N, NE, E, SE, S, SW and W).

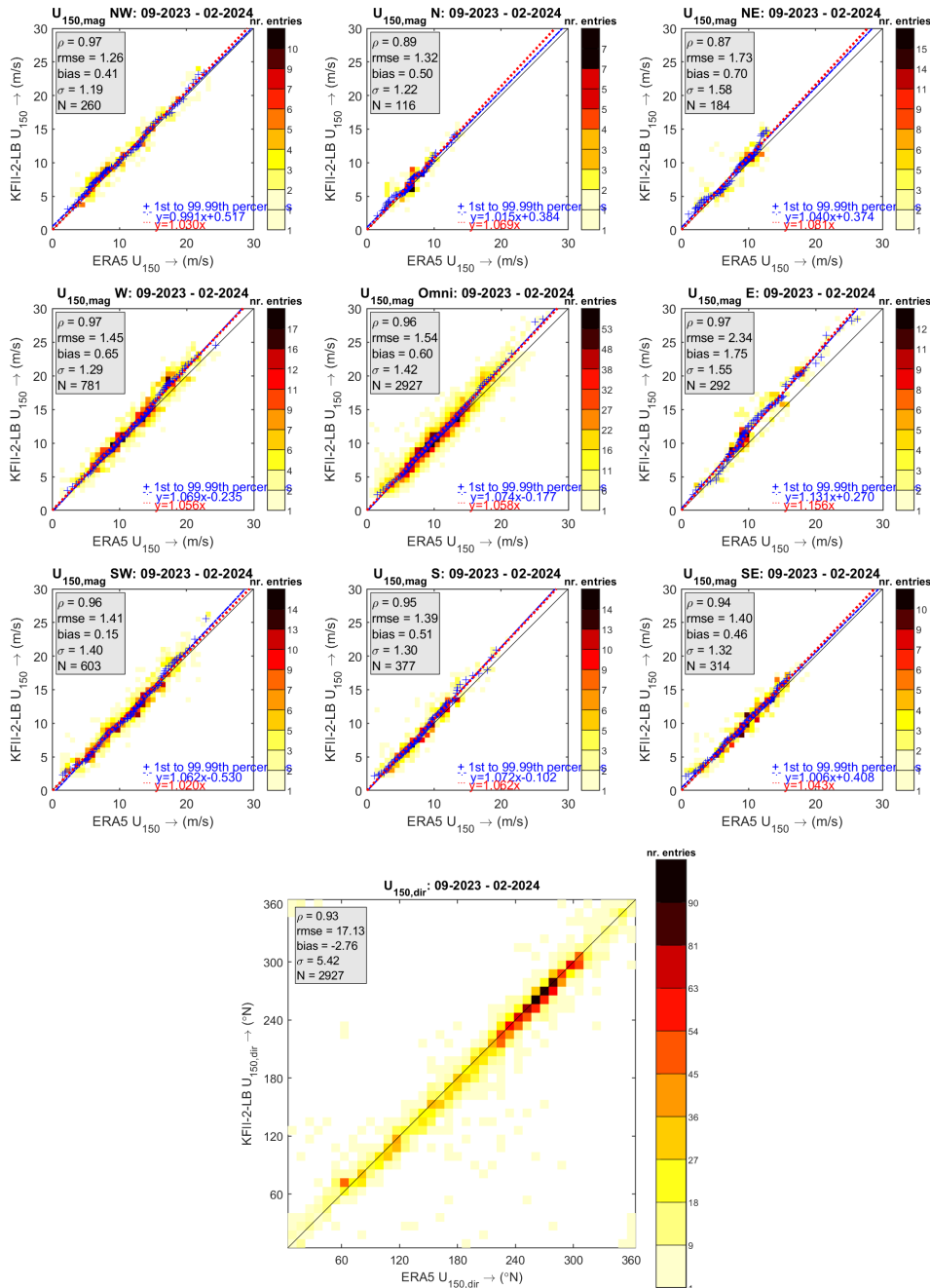


Figure 3-5 Wind speed (top 9 panels) and direction (lower panel) density scatter comparisons between the KFI-2-LB observations at 150 m and the ERA5 data at 150 m. The middle panel of the top 9 shows the omni-directional comparisons and the panels surrounding it show the comparisons for the corresponding directional sectors (from top left, clockwise: NW, N, NE, E, SE, S, SW and W).

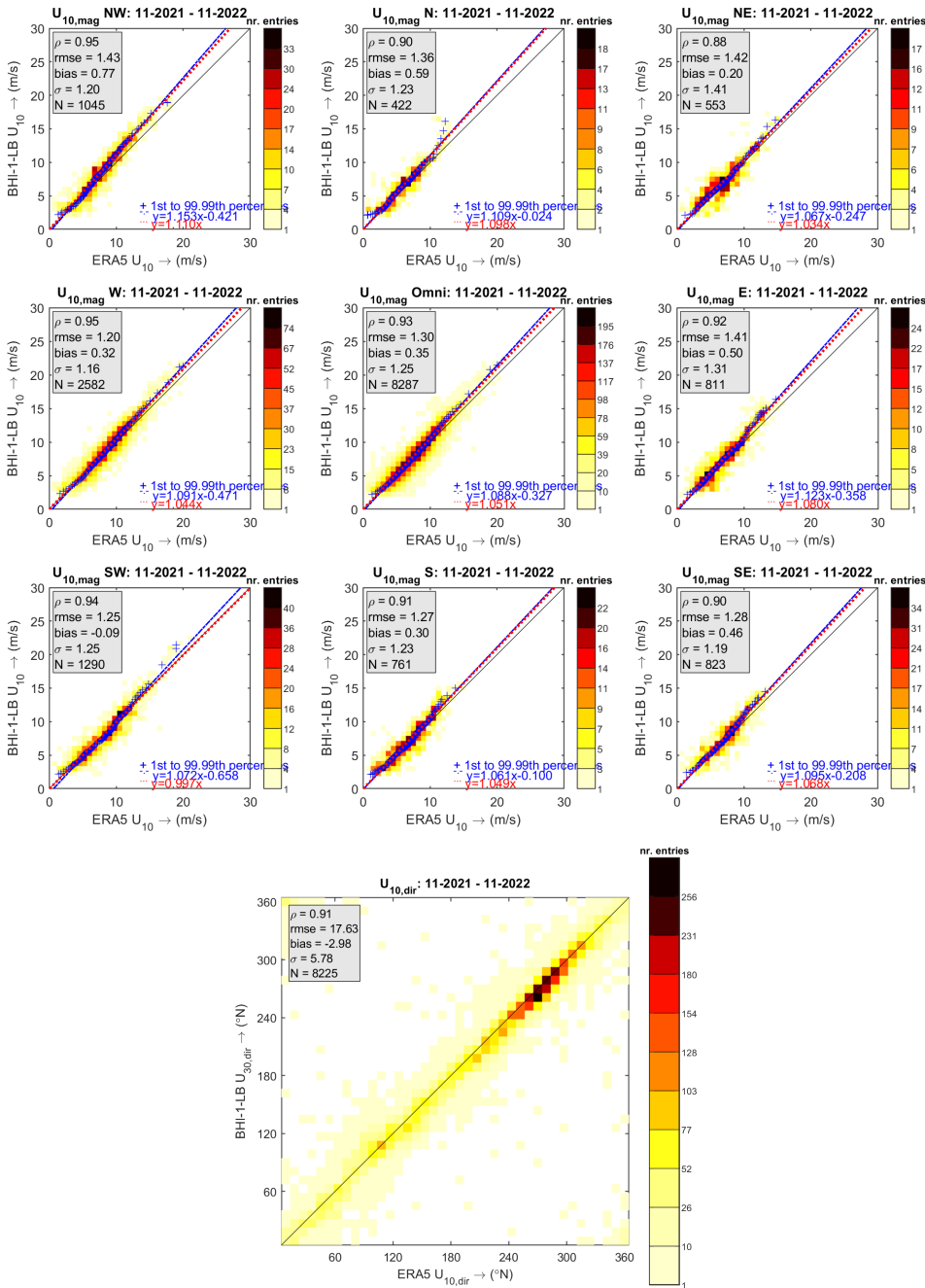


Figure 3-6 Wind speed (top 9 panels) and direction (lower panel) density scatter comparisons between the BHI-1-LB observations at 4 m (converted to 10 m) and the downscaled ERA5 data at 10 m. The middle panel of the top 9 shows the omni-directional comparisons and the panels surrounding it show the comparisons for the corresponding directional sectors (from top left, clockwise: NW, N, NE, E, SE, S, SW and W).

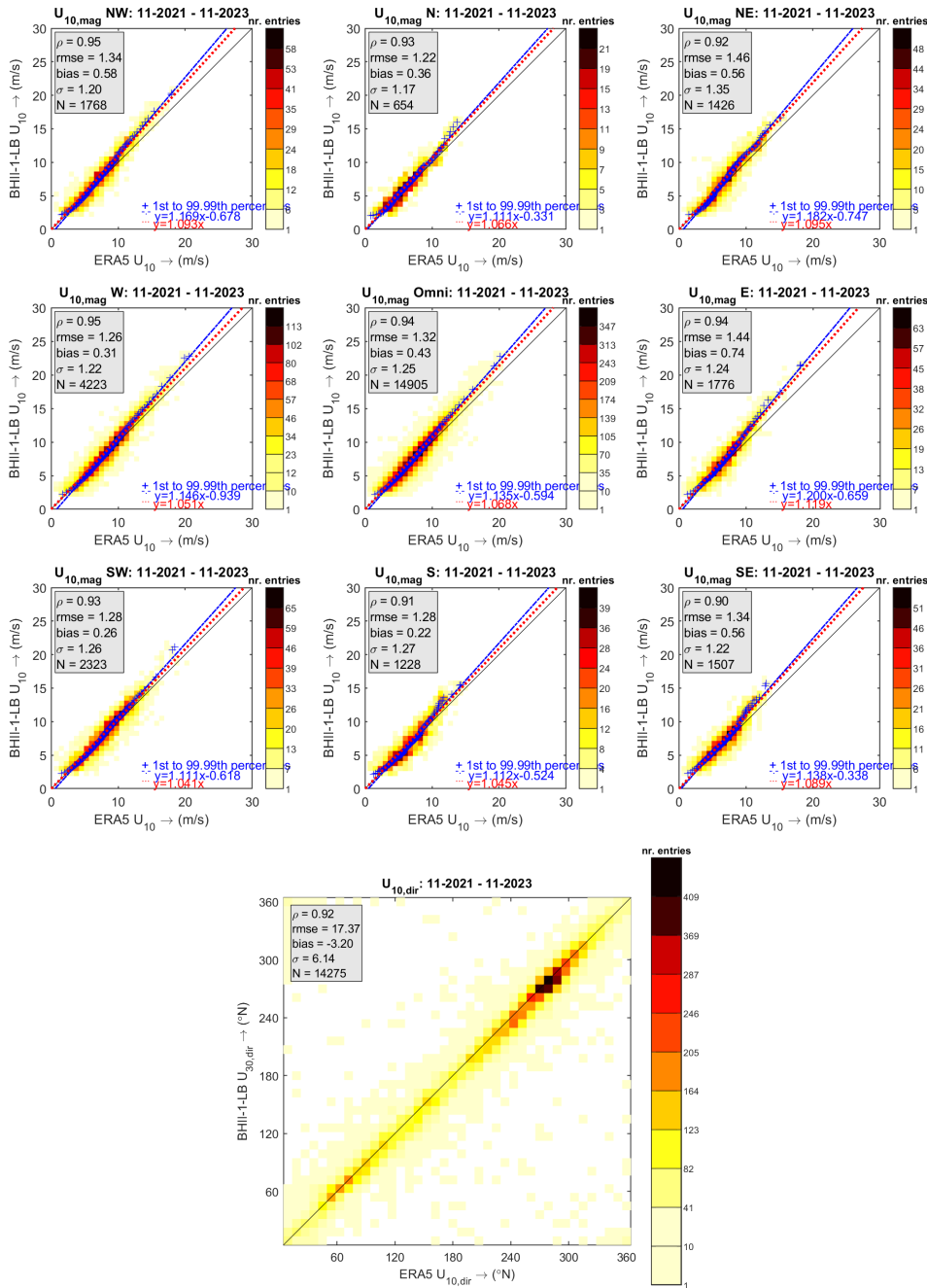


Figure 3-7 Wind speed (top 9 panels) and direction (lower panel) density scatter comparisons between the BHII-1-LB observations at 4 m (converted to 10 m) and the downscaled ERA5 data at 10 m. The middle panel of the top 9 shows the omni-directional comparisons and the panels surrounding it show the comparisons for the corresponding directional sectors (from top left, clockwise: NW, N, NE, E, SE, S, SW and W).

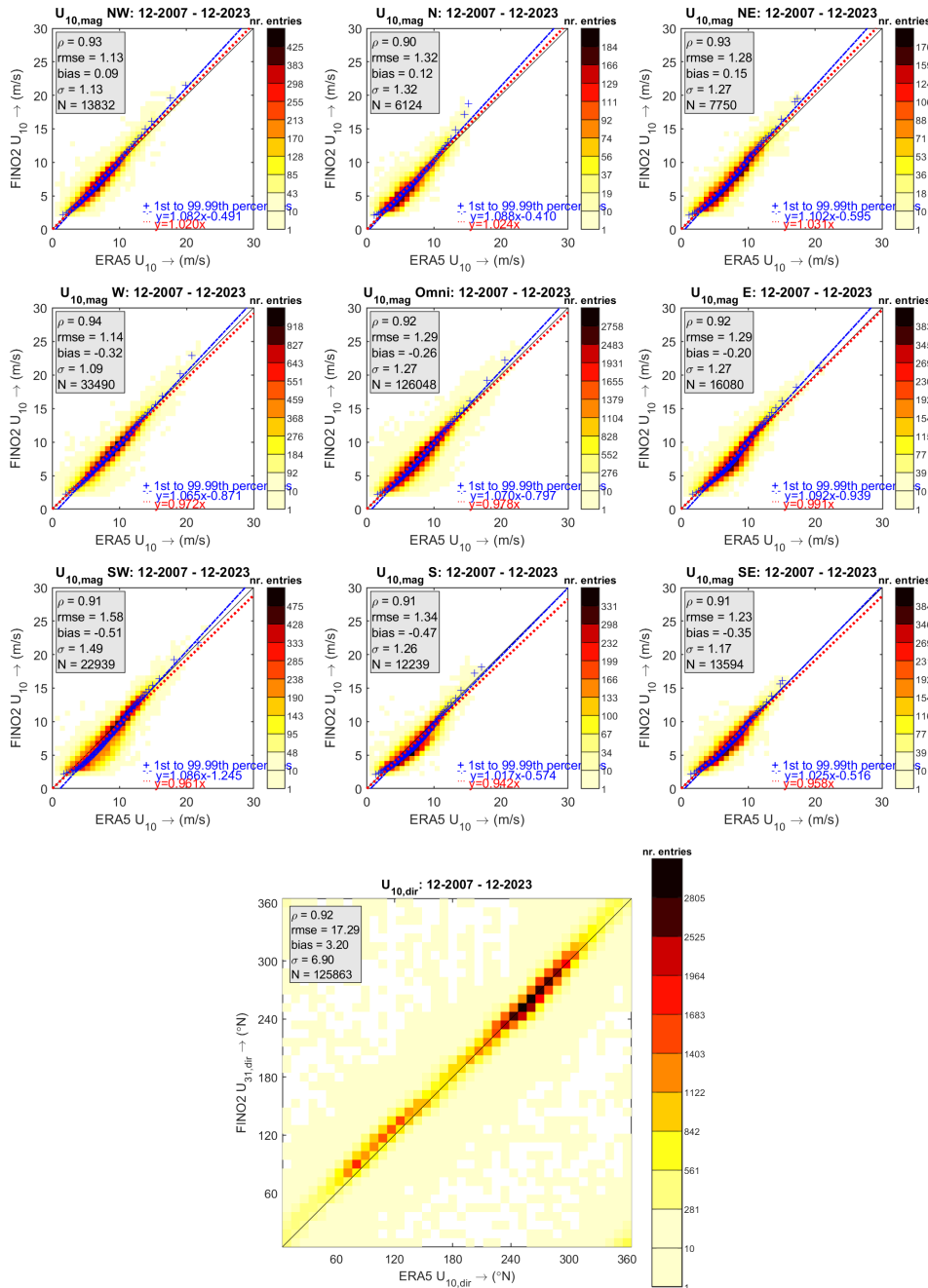


Figure 3-8 Wind speed (top 9 panels) and direction (lower panel) density scatter comparisons between the FINO2 observations at 32 m (converted to 10 m) and the downscaled ERA5 data at 10 m. The middle panel of the top 9 shows the omni-directional comparisons and the panels surrounding it show the comparisons for the corresponding directional sectors (from top left, clockwise: NW, N, NE, E, SE, S, SW and W).

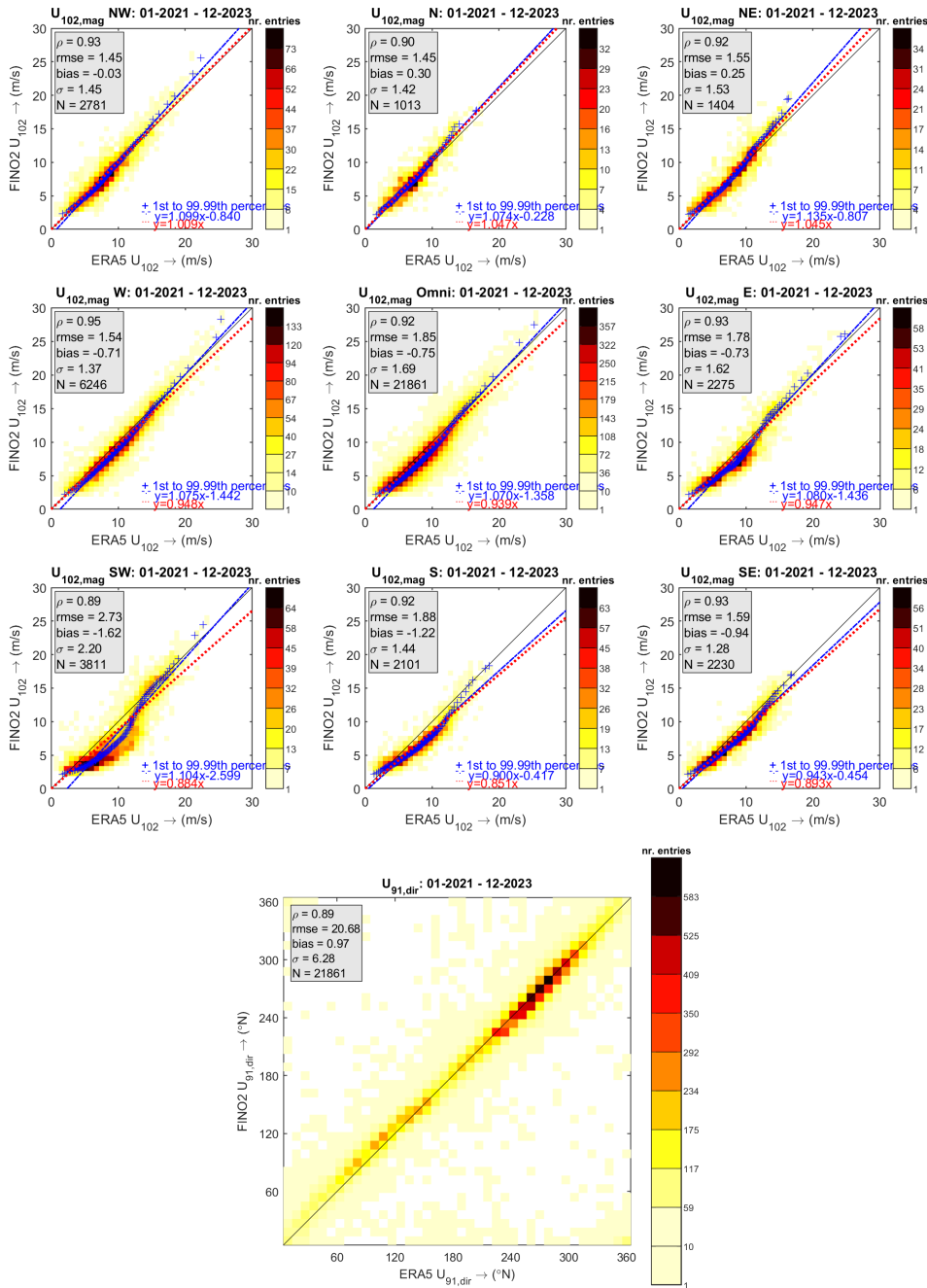


Figure 3-9 Wind speed (top 9 panels) and direction (lower panel) density scatter comparisons between the FINO2 observations at 102/91 m and the ERA5 data at 102/91 m. The middle panel of the top 9 shows the omni-directional comparisons and the panels surrounding it show the comparisons for the corresponding directional sectors (from top left, clockwise: NW, N, NE, E, SE, S, SW and W).

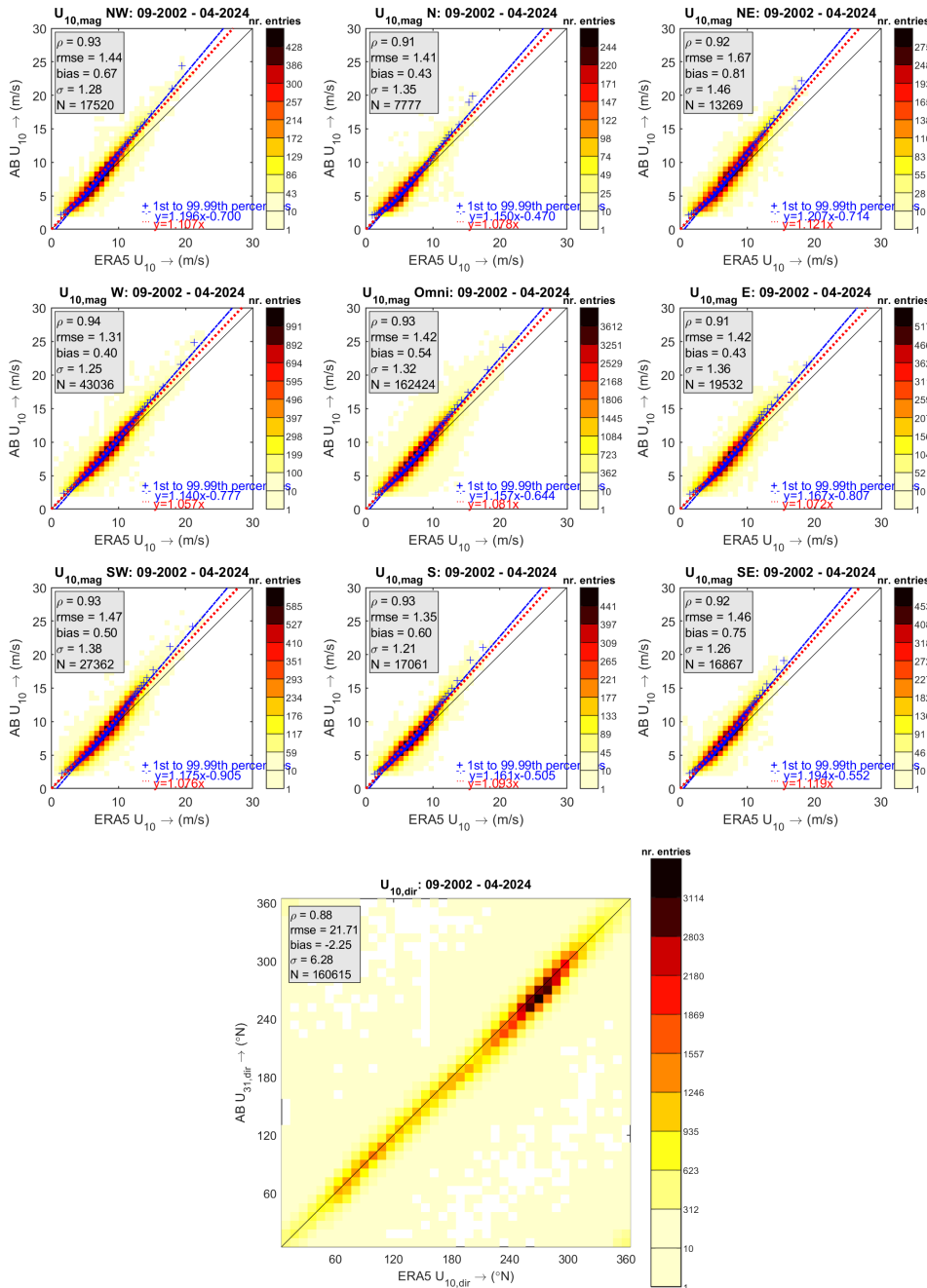


Figure 3-10 Wind speed (top 9 panels) and direction (lower panel) density scatter comparisons between the Arkona Basin (AB) observations at 10 m and the downscaled ERA5 data at 10 m. The middle panel of the top 9 shows the omni-directional comparisons and the panels surrounding it show the comparisons for the corresponding directional sectors (from top left, clockwise: NW, N, NE, E, SE, S, SW and W).

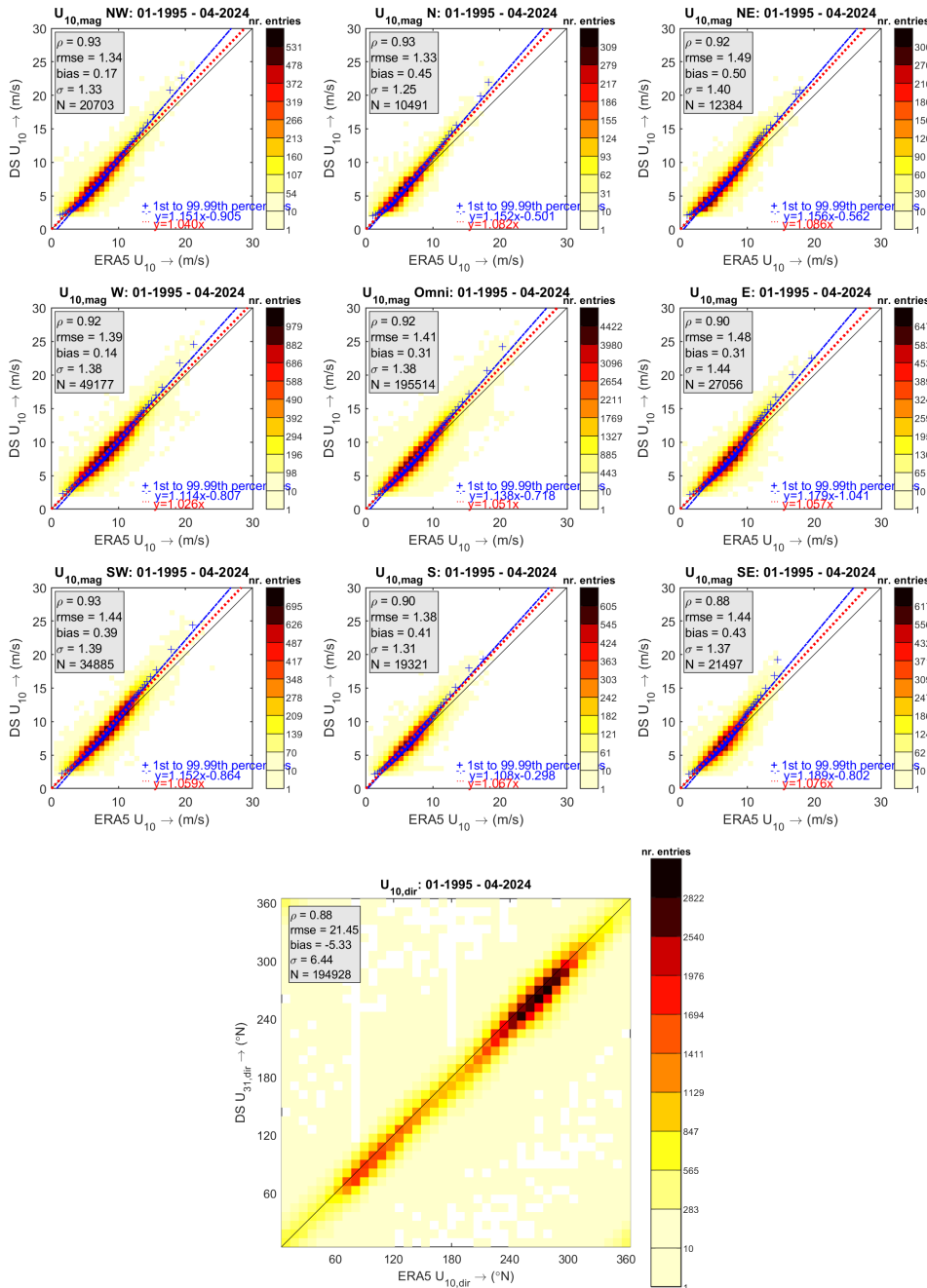


Figure 3-11 Wind speed (top 9 panels) and direction (lower panel) density scatter comparisons between the Darsser-Sill (DS) observations at 9 m (converted to 10 m) and the downscaled ERA5 data at 10 m. The middle panel of the top 9 shows the omni-directional comparisons and the panels surrounding it show the comparisons for the corresponding directional sectors (from top left, clockwise: NW, N, NE, E, SE, S, SW and W).

The figures show a very high correlation between the observed and ERA5 wind speeds (0.92-0.96, omni-directional at 10 m height and 0.96-0.97, omni-directional at hub-height) and directions (0.88-0.94). The ERA5 wind fields are, therefore and in line with our experience in other locations, considered to be

very reliable, due to the very high correlations with the observations and are considered to form a solid basis for the hydrodynamic and wave modelling.

Having considered the comparisons in detail (and some timeseries plots, not shown here) it has been concluded that in the considered area the ERA5 data show some underestimation of the high wind speed percentiles, which should be corrected for, using a multiplying factor of 1.12 at the surface (10 mMSL) and a factor of 1.075 at the hub height (150 mMSL). No correction is deemed necessary to be apply to the ERA5 wind directions. The calibrated ERA5 wind speeds and directions are considered to form a solid basis for the metocean analyses. The factors that have been applied are given in Table 3-3.

Table 3-3 ERA5 wind speed calibration factors.

Variable	Factor
10 mMSL wind speed	1.12
150 mMSL wind speed	1.075

3.2.4.2 Atmospheric data

The ERA5 air pressure, air temperature at 2 m and the relative humidity data were validated against available observations from the floating LiDAR buoys that are currently deployed in the Kriegers Flak II North and South areas during a one-year measurement campaign. Density scatter plots of these comparisons are presented for the KFII North (KFII-2-LB) and KFII South (KFII-1-LB) buoys in Figure 3-12 and Figure 3-13 respectively.

The comparisons show an excellent to perfect correlation between the sea level pressure and air temperature ERA5 data and the measurements (1.00 for KFII North and 0.94-1.00 for KFII South). On the other hand, the figures show that there is only at most fair comparison for the relative humidity data in terms of correlation; the correlation levels vary between 0.51 and 0.54 and the comparisons show quite a bit of scatter. Nevertheless, the mean and high percentile values appear to be trustworthy. The model values below 50-55% are most likely outliers and these values, in particular the minimum value of the dataset, should be interpreted with care.

Unfortunately, no measurement data of solar radiation for nearby locations were available for validation of the ERA5 data. The solar radiation data delivered with this report should therefore be considered as non-validated data. Based on our experience, the quality of the data should nevertheless be high.

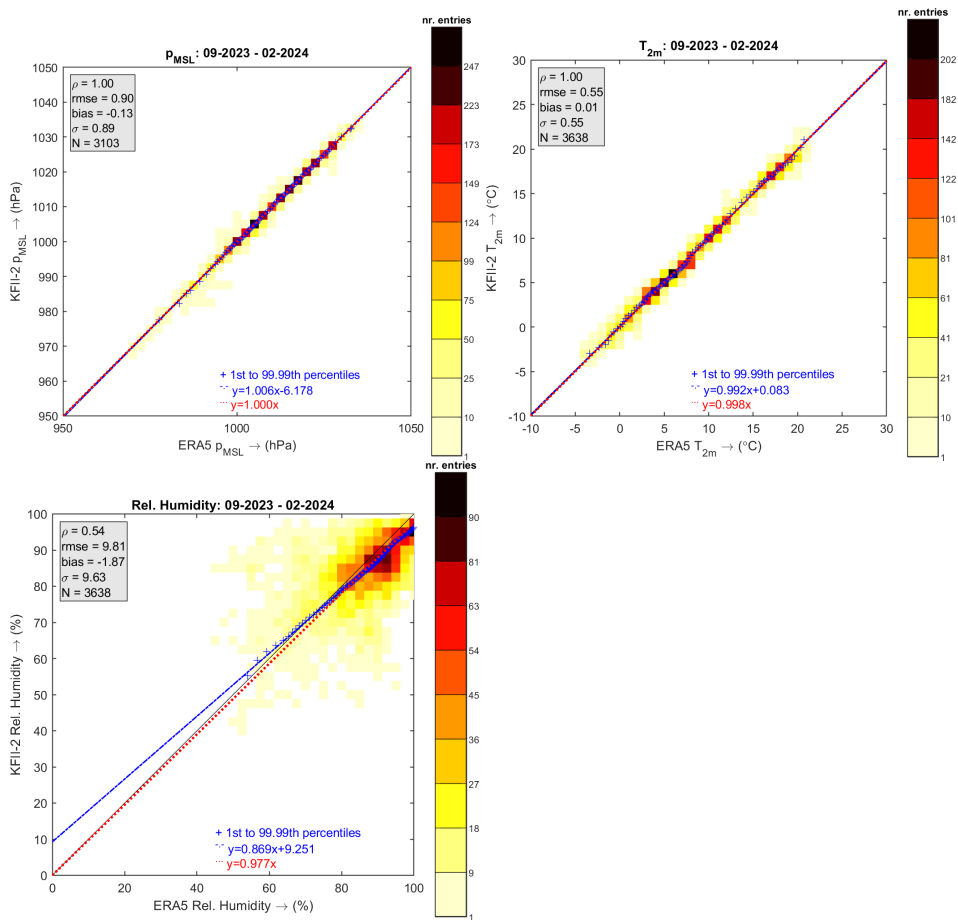


Figure 3-12 Density scatter plots of atmospheric pressure at mean sea level (top left), air temperature (top right) and relative humidity (lower left) for ERA5 vs measurements at the Kriegers Flak II N buoy (KFI-2-LB).

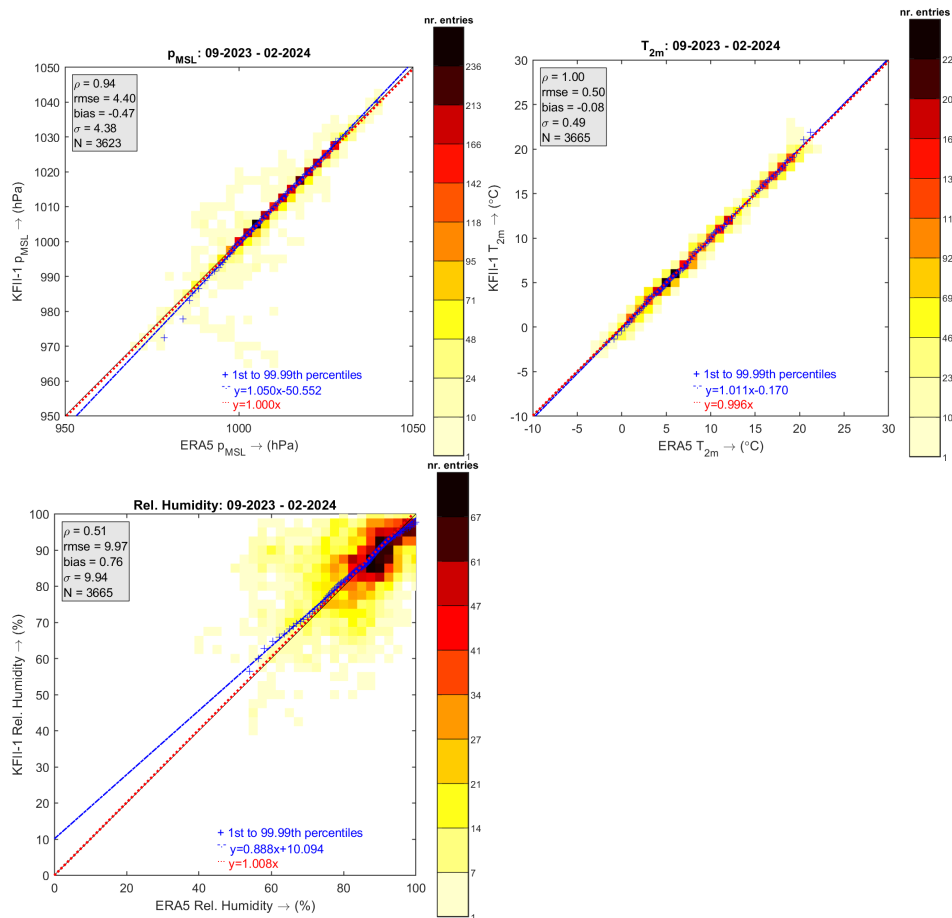


Figure 3-13 Density scatter plots of atmospheric pressure at mean sea level (top left), air temperature (top right) and relative humidity (lower left) for ERA5 vs measurements at the Kriegers Flak II South buoy (KFII-1-LB).

3.2.5 The Kriegers Flak II North and South (KFII) OWF datasets

3.2.5.1 Wind

Based on the validation and proposed calibration of the (downscaled) ERA5 data in the KFII OWF area presented in Section 3.2.4.1, the wind speed and direction timeseries were derived. The 10 m wind speeds are determined from the 10 mMSL ERA5 wind speeds calibrated using a factor of 1.12. The wind speeds at hub height (150 mMSL) are derived by linear interpolation of the ERA5 data at the fixed and (time-varying) pressure layer levels to the hub height and calibrated using a factor of 1.075. The ERA5 wind directions need no calibration and remain therefore unchanged.

The resulting timeseries of wind speed and directions are considered to accurately describe the 1-hour averaged winds in the area of the KFII OWFs at 10 mMSL height and at the hub height. These timeseries are provided together with this report as NetCDF files (together with the wave data) at both the reference locations (cf. Table 2-1, including hub-height wind data) and at the output locations within the data delivery area (excluding hub-height wind data) and cover the period from 1979 to 2023 (45 years, 01-01-1979 00:00 – 31-12-2023 23:00) at an hourly interval.

The naming of the two types of files follows the following structure:

- **Reference locations (6 in total):**
KriegersFlakIIArea_Point
name_latitudeN_longitudeE_WavesWind_1979_2023.nc
- **Data delivery area locations (9,318 in total):**
KriegersFlakIIArea_latitudeN_longitudeE_WavesWind_1979_2023.nc

The reference point timeseries are used in Part B (SWECO, 2024) of the study as input for the determination of the normal and extreme wind conditions.

3.2.5.2 Atmospheric data

Based on the validation of the ERA5 atmospheric data in the KFII OWF area presented in Section 3.2.4.2, the atmospheric data (air temperature at 2m T_{2m} , surface air pressure P, surface solar radiation SSR and relative humidity RH) timeseries were derived. As concluded in Section 3.2.4.2, the ERA5 atmospheric data need no calibration and remain therefore unchanged.

The resulting timeseries are provided together with this report as NetCDF files at both a single representative location per wind farm area and at various output locations covering the data delivery area (using the resolution at which the data was downloaded from ERA5) and cover the period from 1979 to 2023 (45 years, 01-01-1979 00:00 – 31-12-2023 23:00) at an hourly interval.

The naming of the two types of files follows the following structure:

- **Wind farm locations (2 in total):**
OWF name_latitudeN_longitudeE_AtmosData_1979_2023.nc
- **Data delivery area locations (1 in total):**
KriegersFlakIIArea_AtmosData_1979_2023.nc

The reference point timeseries are used in Part B (SWECO, 2024) of the study as input for the determination of the atmospheric data conditions.

3.3 Hydrodynamic data

3.3.1 Introduction

The hydrodynamic modelling performed in this study had as objective to derive accurate water properties (temperature, salinity and density), water levels and flow velocity timeseries to be used as input for the metocean assessments.

The water levels, vertical water properties (temperature, salinity and density) and flow velocity timeseries hydrodynamic conditions were derived from a simulation for the period of 2014–2023 (i.e. 10 years, 01-01-2014 00:00 – 31-12-2022 23:00) based on a three-dimensional (3D) modelling approach and water levels and depth-averaged flow velocities from a simulation for the period of 1979–2023 (i.e. 45 years, 01-01-1994 00:00 – 31-12-2022 23:00) based on a two-dimensional horizontal (2DH) modelling approach. These data were validated and calibrated against a large set of observations available in the area.

In order to enhance the robustness of the current and water level extreme estimates, the calibrated 10 years of computed 3D current velocities and water levels have been combined with the computed 2DH 45 years of depth-averaged current velocity and water levels to generate accurate 45 year long hourly

timeseries of current velocities and water levels at all data delivery area locations.

In the next section the modelling hydrodynamic modelling is described, followed by the validation and calibration of the model results. In Section 3.3.4 the determination of the vertical current profiles and extension of the 3D model results to the 45 year period is described. The resulting dataset is summarized in Section 3.3.5.

3.3.2 Hydrodynamic modelling

3.3.2.1 *Introduction*

For both the 3D and 2DH modelling we apply the Flow module of the Deltares Delft3D Flexible Mesh Modelling Suite, which is described in Appendix B. In the following the model setup, input and output are described.

3.3.2.2 *Model domain, horizontal mesh, vertical grid and bathymetry*

The basis for the hydrodynamic modelling is Deltares' extensively calibrated 3D Dutch Continental Shelf, Flexible Mesh Model (DCSM-FM). The 3D DCSM-FM model (Zijl et al., 2021) builds on the depth-averaged DCSM-FM 0.5 nm (nautical mile) model, which has been developed by Deltares (2019) for Rijkswaterstaat (RWS, the executive agency of the Ministry of Infrastructure and Water Management of the Dutch Government) and is used for e.g. operational forecasting. The model covered initially only the northwest European continental shelf between 15°W to 13°E and 43°N to 64°N and was subsequently extended with the entire Baltic Sea, see Figure 3-14. The overall model domain, bathymetry and resolution is shown in Figure 3-14.

The horizontal grid resolution ranges across the model domain from 4 to 0.5 nm depending on the bathymetry. In the offshore wind farm areas Kriegers Flak II North and South the model resolution has been increased to up to 100 m, see Figure 3-15.

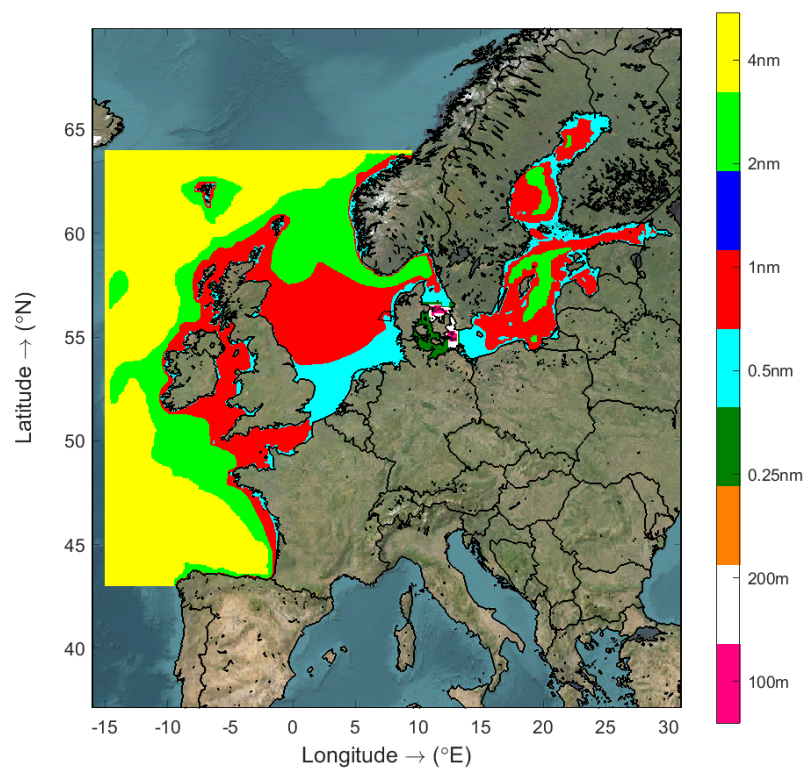
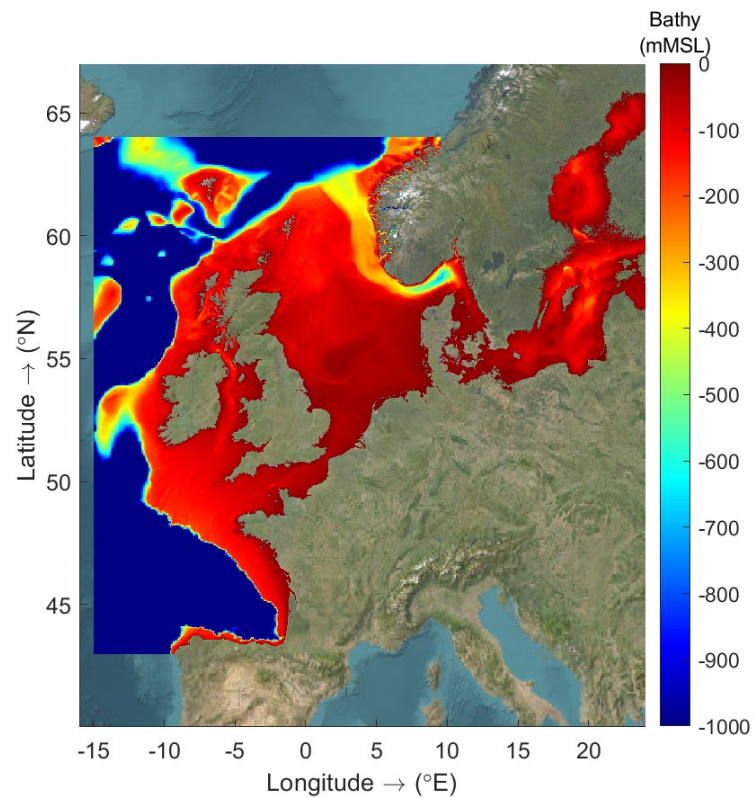


Figure 3-14 Domain and bathymetry (top) and resolution (bottom) of the DCSM-FM model with Baltic extension.

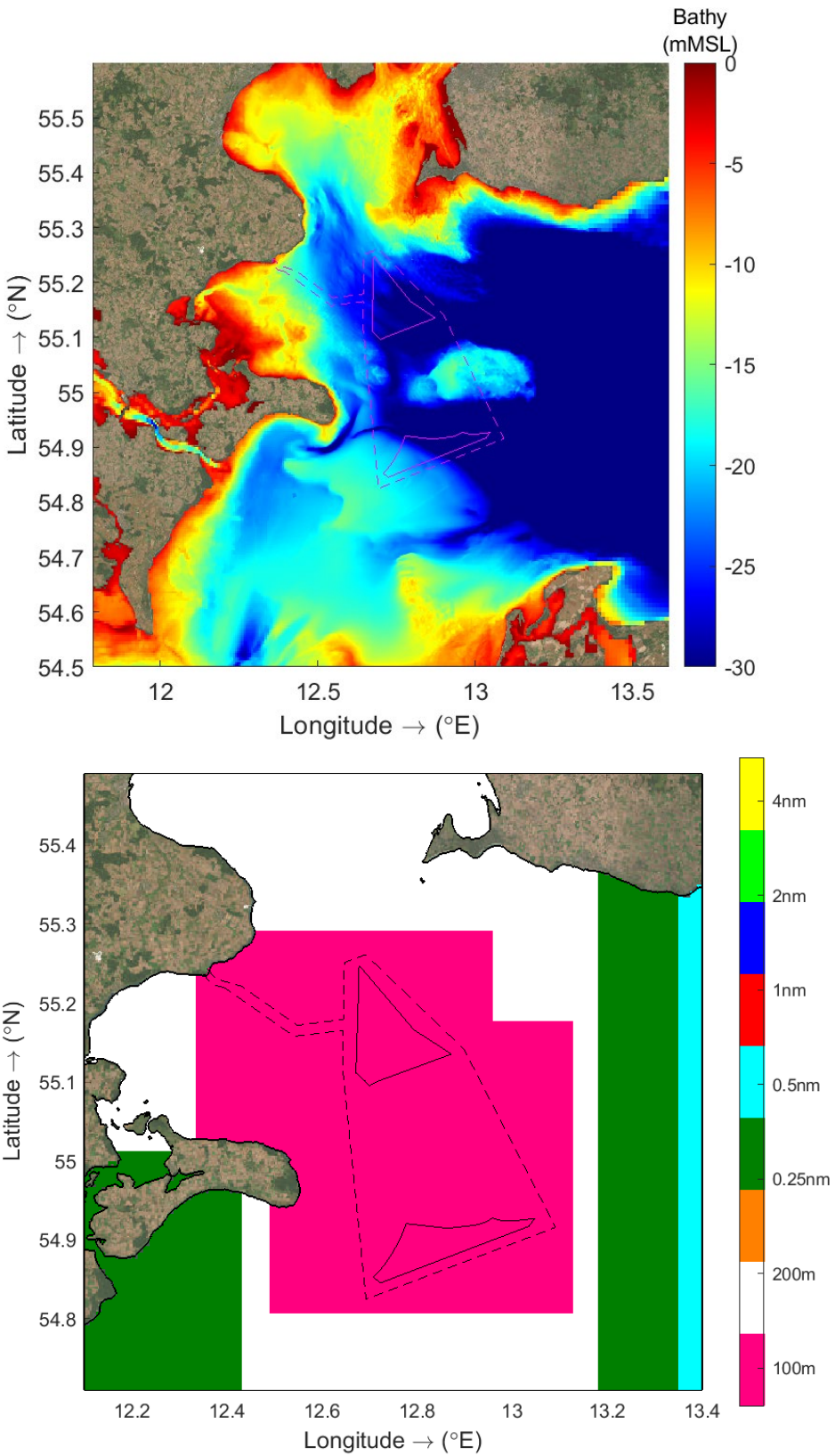


Figure 3-15 Zoom in of the bathymetry (top) and resolution (bottom) of the DCSM-FM model with Baltic extension in the Kriegers Flak II North and South area.

The model bathymetry has been derived from a gridded bathymetric dataset from the European Marine Observation and Data Network (EMODnet 2022 release, <http://portal.emodnet-bathymetry.eu>¹¹). The resolution of the gridded EMODnet dataset is 1/16' x 1/16' (circa 115 x 115 m). Locally, in the refined region, the bathymetry has been replaced by the high-resolution bathymetrical survey datasets provided by the Client (cf. Figure 2-3). The model's bathymetry in the area of interest is shown in Figure 3-15.

The 3D model uses the same horizontal grid and bathymetry as the 2DH model and has a total of 20 σ -layers up until a 100 m depth followed by 18 z-layers with thickness growing from 5 m with a growth factor of 1.19, allowing for the derivation of salinity, density, conductivity and temperature values over depth as well as currents and various depth levels and profiles. Given that most of the project region is shallower than 100 m, the 3D model has only 20 σ -layers in most of the region.

3.3.2.3 Model forcing

At the lateral open boundaries temperature and salinity are derived from CMEMS (product: [GLOBAL MULTIYEAR PHY 001_030](#) until the January 1st, 2021, and from then product [GLOBAL ANALYSISFORECAST PHY 001_024](#) was used). These daily values at 50 non-uniformly spaced vertical levels are interpolated by Delft3D FM to the right horizontal location and model layers. Furthermore, more than 300 climatological freshwater discharges are included.

The model is forced with (raw) hourly ERA5 data of the following meteorological parameters:

- air pressure (both the 3D and the 2DH model),
- neutral wind¹² (both the 3D and the 2DH model),
- dew point, air temperature and cloudiness (the 3D model only),
- solar (short-wave) radiation (the 3D model only),
- atmospheric (long-wave) radiation (the 3D model only), and
- rainfall rate (the 3D model only).

Momentum flux

The air-sea momentum flux is accounted for in the D-Flow model by using temporally and spatially varying neutral wind speeds at 10 m height and atmospheric pressure at mean sea level (cf. Zijl et al., 2021). In order to be consistent with the Atmospheric Boundary Layer (ABL) model that is used in the ERA5 meteorological model, a temporally and spatially varying Charnock coefficient (Charnock, 1955) is applied in the D-Flow model. The Charnock formulation assumes a fully developed turbulent boundary layer of the wind flow over the water surface. The associated wind speed profile follows a logarithmic shape. The wind shear stress, which represents the momentum exchange between air and water, is used in the D-Flow model to express the wind speed relative to the velocity of the water surface flow.

¹¹ Deltares is partner in the EMODnet High Resolution Seabed Mapping (HRSM) project.

¹² Calculated from the surface stress and the corresponding roughness length by assuming neutrally stratified air.

Heat flux

Horizontal and vertical spatial differences in water temperature affect the transport of water through its impact on the water density. For example, heating of surface water and shallow waters causes temperature gradients that can generate horizontal flow. It can also lead to temperature stratification with accompanying damping of turbulence and hence a reduction in vertical mixing. To include these effects, the transport of temperature is accounted for in the 3D version of the model. For its main driver, exchange of heat between the water surface and the atmosphere, a heat-flux model is used. This model considers the separate effects of solar (short-wave) and atmospheric (long-wave) radiation, as well as heat loss due to back radiation, evaporation and convection. The temporally and spatially varying turbulent exchange of heat through the air-water interface, due to evaporation and convection, is computed based on the local temperature (at 2 m height), dew point temperature and wind speed from the ERA5 data. To account for the radiative heat fluxes the surface net solar (short-wave) radiation and the surface downwelling long wave radiation have been imposed, while the surface upwelling long-wave radiation is computed based on the modelled sea surface temperature. The incoming solar radiation is distributed over the water column, depending on the water transparency prescribed with a Secchi depth (for more methodological details see Zijl et al., 2021).

Mass-flux

In order to account for the mass-flux through the air-sea interface, temporally and spatially varying fields of evaporation and precipitation are applied in the 3D version of the model.

3.3.2.4 *Miscellaneous model parameter settings*

Besides the model parameters described so far, the model uses further specific numerical and physical parameter settings which are summarised in the table below.

Table 3-4 Settings of the DCSM with Baltic extension model parameters.

Parameter	Keyword	Value/setting
Bottom roughness (Manning's n)	UnifFrictCoef	0.028 s m ^{-1/3} (uniform)
Horizontal eddy viscosity	Vicouv	0.1 m ² /s (uniform)
Horizontal eddy diffusivity	Dicouv	0.1 m ² /s (uniform)
Uniform vertical eddy viscosity	Vicoww	0.0001 [3D]
Uniform vertical eddy diffusivity	Dicoww	0.000014 [3D]
Wind drag coefficient type	lcdtyp	4 [-] (Charnock 1955)
Maximum Courant number	CFLMax	0.7 [-]

3.3.2.5 *Initial conditions, spin-up and simulation times*

All 3D and 2DH D-Flow FM model simulations start with a uniform initial water level of 0 mMSL and a uniform initial flow velocity of 0 m/s in the entire model domain. Salinity and temperature are initialised in the 3D D-Flow model by

interpolating the spatially varying data by CMEMS at the corresponding start time of each simulation to the (horizontal) computational mesh and to the vertical grid. To guarantee that a dynamic equilibrium is reached before the start of the actual hindcast period of each simulation run, a spin-up period of 1 year (3D model) and of 31 days (2DH model) respectively is applied.

The exact simulation times are from 01-Jan-1993 00:00 UTC to 31-March-2024 23:00 UTC in the case of the 3D model and from 01-Jan-1979 00:00 UTC to 31-Dec-2023 23:00 UTC in the case of the 2DH model. In order to reduce the computational times, both the 3D and the 2DH simulation runs are split into 1-year simulations, with corresponding spin-up periods before the actual start of each simulation. For the post-processing, all model data have been merged into continuous timeseries without the spin-up periods. I.e. the model results until 31 December 23:00 of a given year are merged with the model results from 1 January 0:00 of the next year. The hindcast periods covered by the data are January 1979 to December 2023 by the 2DH model and January 2014 to March 2024 by the 3D model. The data of 2024 have only been computed for the validation.

3.3.2.6 *Output definitions*

Timeseries of the hydrodynamic parameters were output by the models at a time step of 1 hour within the data delivery area at a large set of locations, including the reference locations, the observation locations and the delivery area locations.

The hydrodynamic parameters output by the 2DH model are the total water level and the depth-averaged current velocity. The hydrodynamic parameters output by the 3D model are the total water level and at all model levels the current velocity, water temperature and salinity.

3.3.3 Data validation and calibration

3.3.3.1 *Introduction*

The validation of the model is done considering observations in the area of the offshore wind farm areas Kriegers Flak II North and South, for the calibration more weight is given to the comparisons with data from the stations with longer records.

Figure 3-1 shows the locations of the considered water level and current velocity observations. The origins and periods covered by the data are given in Table 3-1 and Table 3-2.

In the validation of the 3D model results, given that these are only available from 2014 to 2024, only observations from 2014 onwards are considered.

3.3.3.2 *Validation of the 2DH model results*

3.3.3.2.1 *Water level comparisons*

Figure 3-16 to Figure 3-25 show the comparisons between the 2DH model water level results and the observations in the Kriegers Flak region. Comparisons are made by means of timeseries covering the full period with a zoom in into the higher event, and density scatter comparisons. The error statistics are given in the scatter plots and summarised in Table 3-5. Before being applied, all water level observation data were first quality controlled. This

means that data gaps were filled with dummy values and outliers to the data were removed from the data based on deviations from the (running) mean and standard deviations over a period of about a month. Furthermore, given that water level observations are by nature inhomogeneous, with variations in the location of the sensor generally leading to jumps in the observed levels, in the comparisons shown the monthly bias between the model and the observations has been removed.

As can be seen in the figures, the correlations between the model results and observations are high, in particular in the stations with a longer record. In the stations Skanör, Køge, Rødvig, Hesnaes and FINO2, those with more than 50,000 records, the correlations range between 96 and 97% and the symmetric slopes (r) of the data are close to 1 (1.019-1.092) but indicate an underestimation by the model data of up to 10% (at Køge). Based on these we recommend a calibration factor of 1.1 to be applied to the raw 2D water level model results. Overall, we conclude that the 2D model results in the Kriegers Flak region, calibrated using a factor of 1.1, already form a solid basis for further assessments. However, given the availability of (higher quality) 3D model data at the same locations as the 2DH model data, the 2DH model results can be locally calibrated against the (validated and calibrated) 3D model water level, leading to an even higher quality water level dataset.

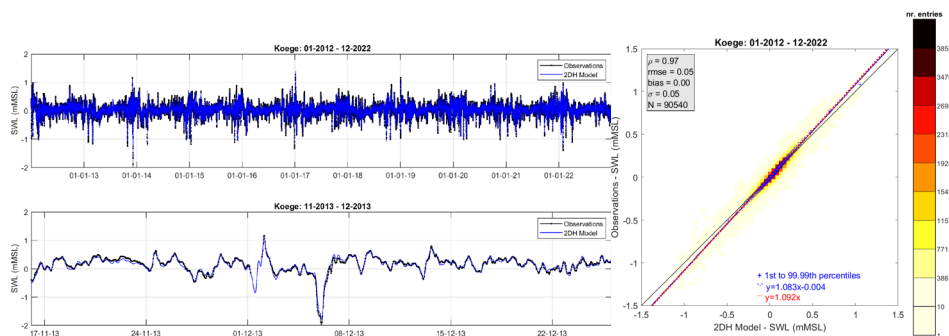


Figure 3-16 Comparisons between the Køge and the 2DH model water levels.

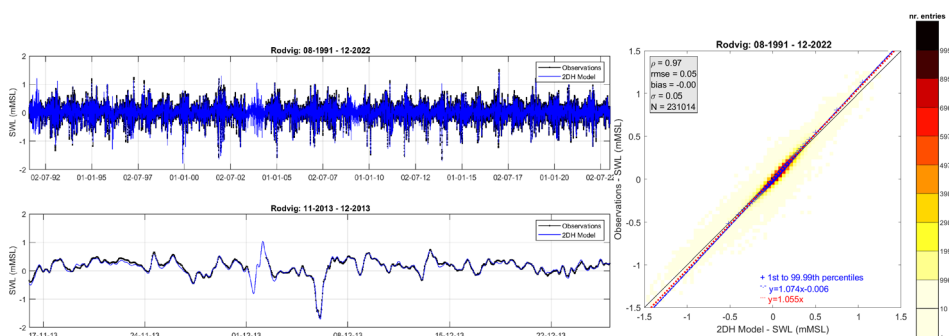


Figure 3-17 Comparisons between the Rødvig and the 2DH model water levels.

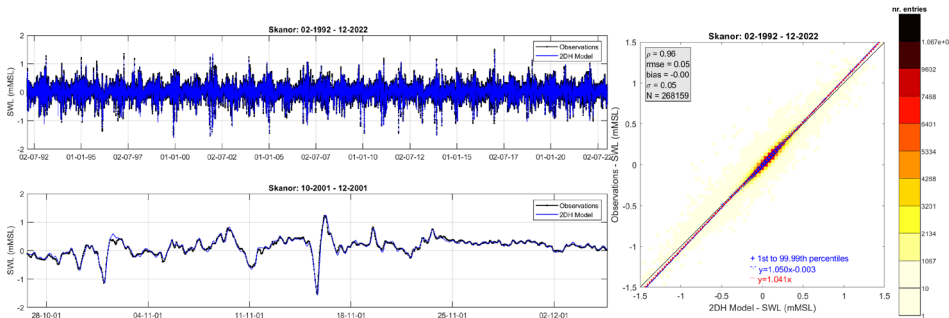


Figure 3-18 Comparisons between the Skanör and the 2DH model water levels.

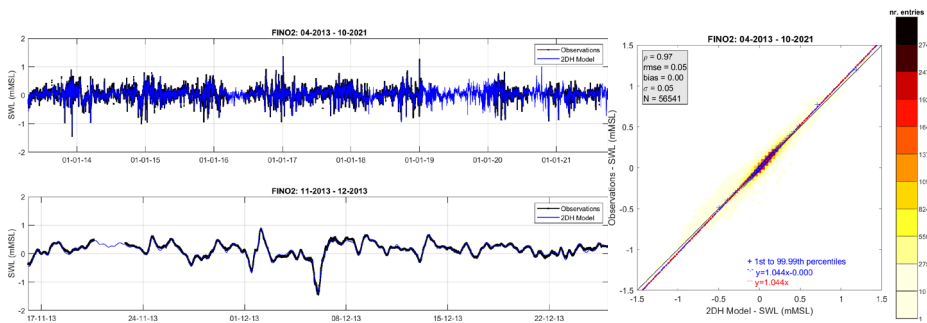


Figure 3-19 Comparisons between the FINO2 and the 2DH model water levels.

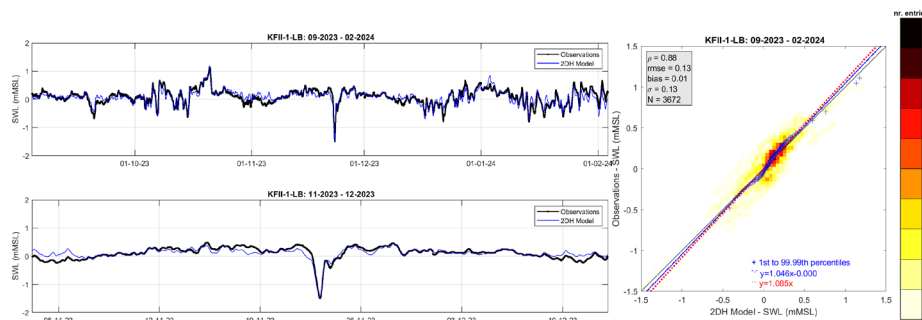


Figure 3-20 Comparisons between the KFII-1-LB and the 2DH model water levels.

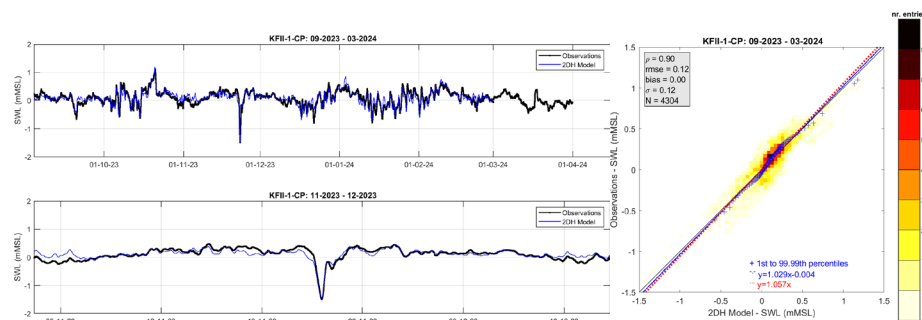


Figure 3-21 Comparisons between the KFII-1-CP and the 2DH model water levels.

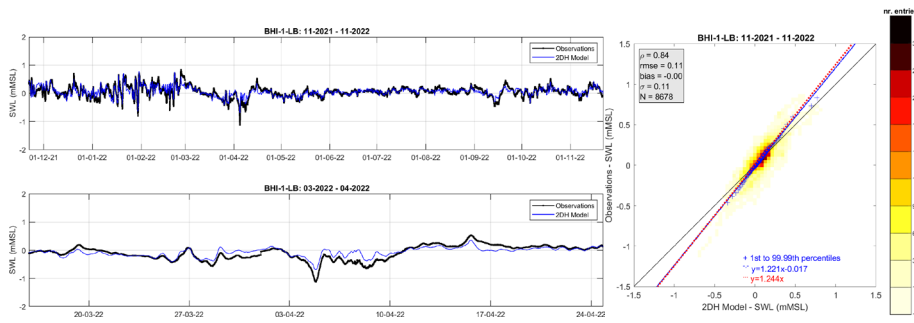


Figure 3-22 Comparisons between the BHI-1-LB and the 2DH model water levels.

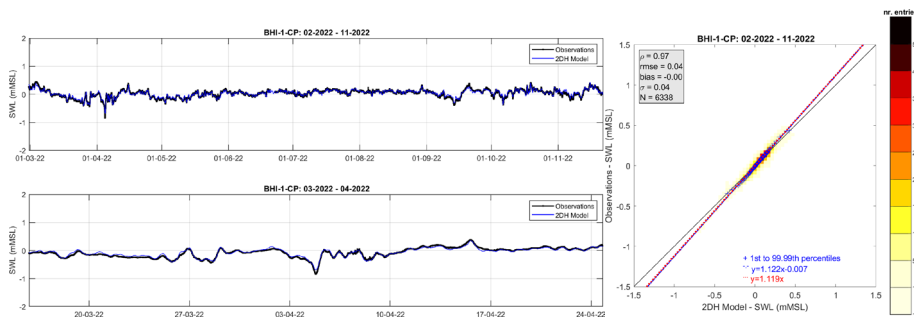


Figure 3-23 Comparisons between the BHI-1-CP and the 2DH model water levels.

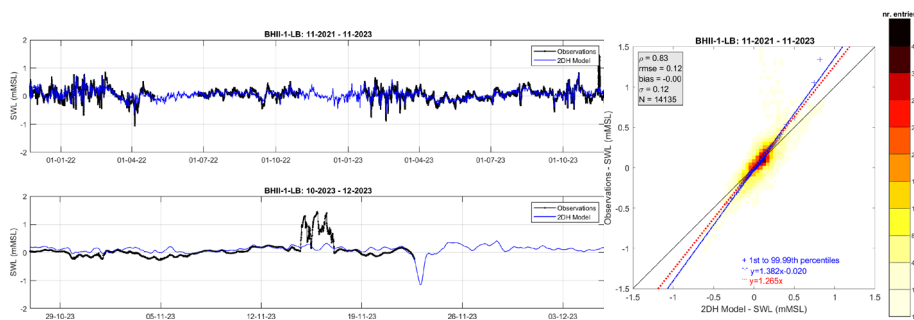


Figure 3-24 Comparisons between the BHII-1-LB and the 2DH model water levels.

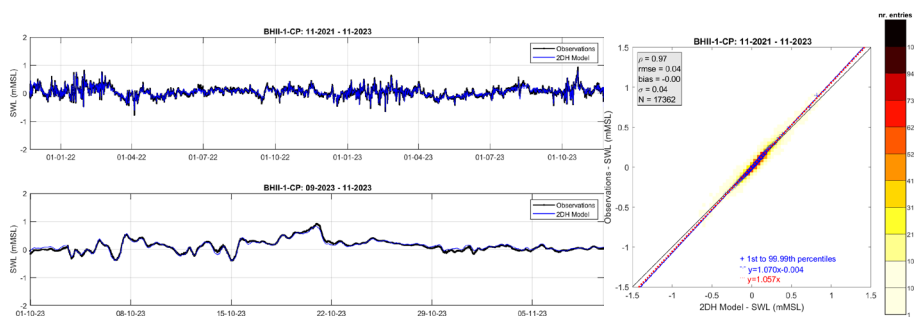


Figure 3-25 Comparisons between the BHII-1-CP and the 2DH model water levels.

Table 3-5 Water level statistics based on 2DH model results.

Water level	ρ	RMSE	σ	n	r
Skånör	0.96	0.05	0.05	268159	1.041
Køge	0.97	0.05	0.05	90540	1.092
Rødvig	0.97	0.05	0.05	231014	1.055
Hesnaes	0.97	0.05	0.05	158089	1.019
FINO2	0.97	0.05	0.05	56541	1.044
(KFII-1-CP)	0.90	0.12	0.12	4304	1.057
(KFII-1-LB)	0.88	0.13	0.13	3672	1.085
(KFII-2-CP)	0.92	0.11	0.11	2867	1.109
(KFII-2-LB)	0.91	0.11	0.11	2865	1.117
(BHI-1-CP)	0.97	0.04	0.04	6338	1.119
(BHI-1-LB)	0.84	0.11	0.11	8678	1.244
(BHII-1-CP)	0.97	0.04	0.04	17362	1.057
(BHII-1-LB)	0.83	0.12	0.12	14135	1.265

3.3.3.2.2 Current velocity comparisons

In the following we present the validation of the 2D model depth-averaged current results. Before being applied, all current observation data were first quality controlled. This means that data gaps were filled with dummy values and outliers to the data were removed from the data based on deviations from the (running) mean and standard deviations over a period of about a month. Nevertheless, there are still some observations that look spurious, but which have not been identified by the algorithms and have therefore been kept.

Figure 3-26 to Figure 3-31 show the comparisons between the 2DH model depth-averaged currents and the observations in the Kriegers Flak region. Comparisons are made between the model depth-averaged currents and the depth-averaged currents computed from the observations. For certain levels it has been found that the model depth-averaged results show higher correlations with the data from that level than the depth averaged mean of the observations (not shown). However, given that we are interested in the validation of the depth-average value in here we only present these plots. Each figure shows the timeseries of the depth-averaged current speeds and the respective density scatter comparisons (top) and the depth-averaged current speeds and the respective density scatter (bottom). The error statistics are given in the scatter plots and summarised in Table 3-6.

The figures show some correspondence between the model and observed speeds, but generally low correlations, a large spread between the current directions but no indications of systematic offsets. This is as expected given that the currents are generally very low (lower than 10 cm/s which is about the expected model accuracy), and the model does not account for relevant density driven effects. Nevertheless, at location Darsser-Sill, the location with the most observations, the correlation between the speeds is 64% and the symmetric slope close to 1.5. Based on these we conclude that it would be beneficial to

calibrate the raw 2DH depth-averaged current speeds with a factor of 1.5. However, given the availability of (higher quality) 3D model data at the same locations as the 2DH model data, at all locations considered in this study the 2D model results can be calibrated against the (validated and calibrated) 3D model results per location, see Section 3.3.4.

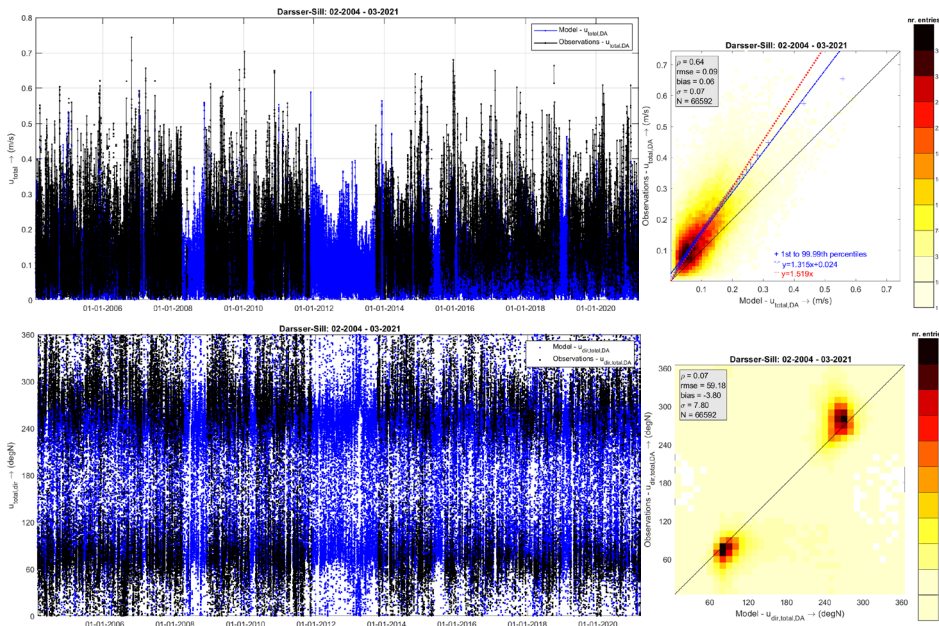


Figure 3-26 Comparisons between the Darsser-Sill and the 2DH model current speeds and directions.

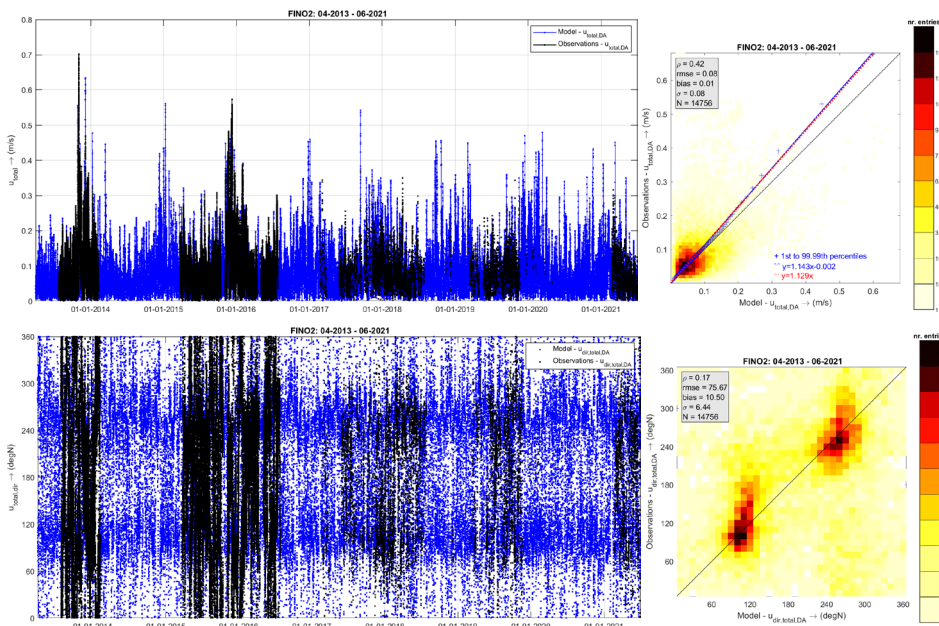


Figure 3-27 Comparisons between the FINO2 and the 2DH model current speeds and directions.

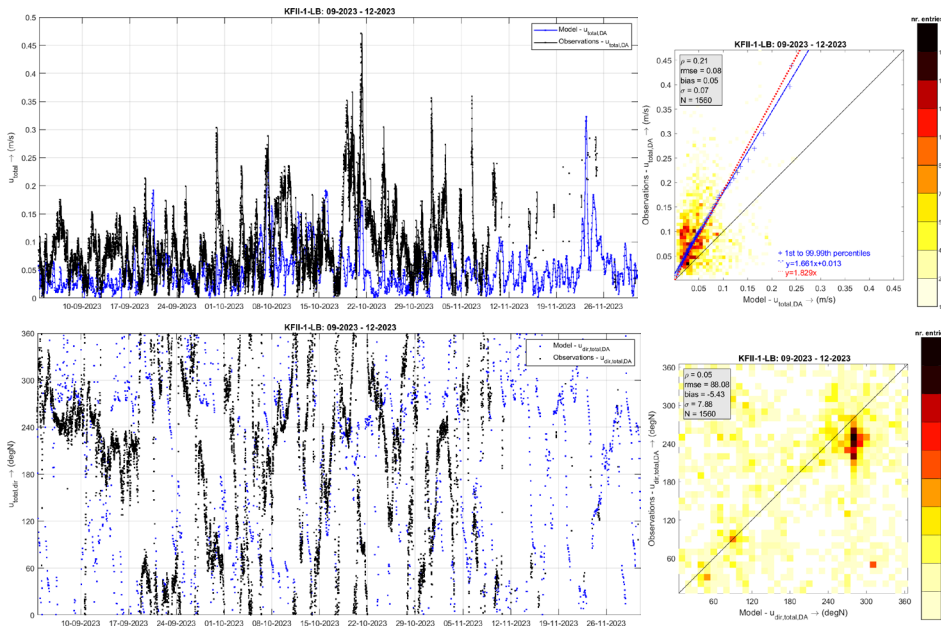


Figure 3-28 Comparisons between the KFII-1-LB and the 2DH model current speeds and directions.

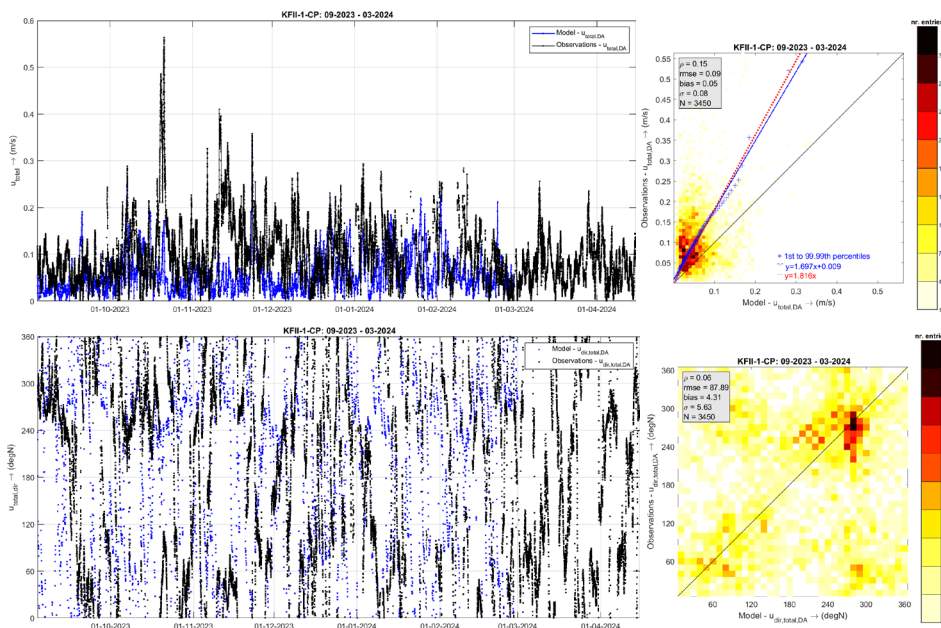


Figure 3-29 Comparisons between the KFII-1-CP and the 2DH model current speeds and directions.

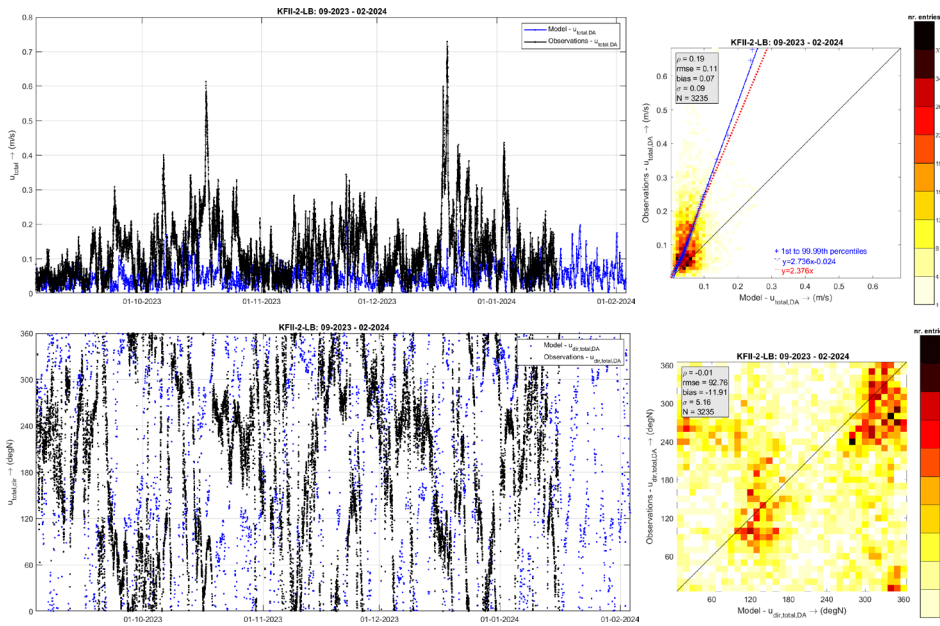


Figure 3-30 Comparisons between the KFII-2-LB and the 2DH model current speeds and directions.

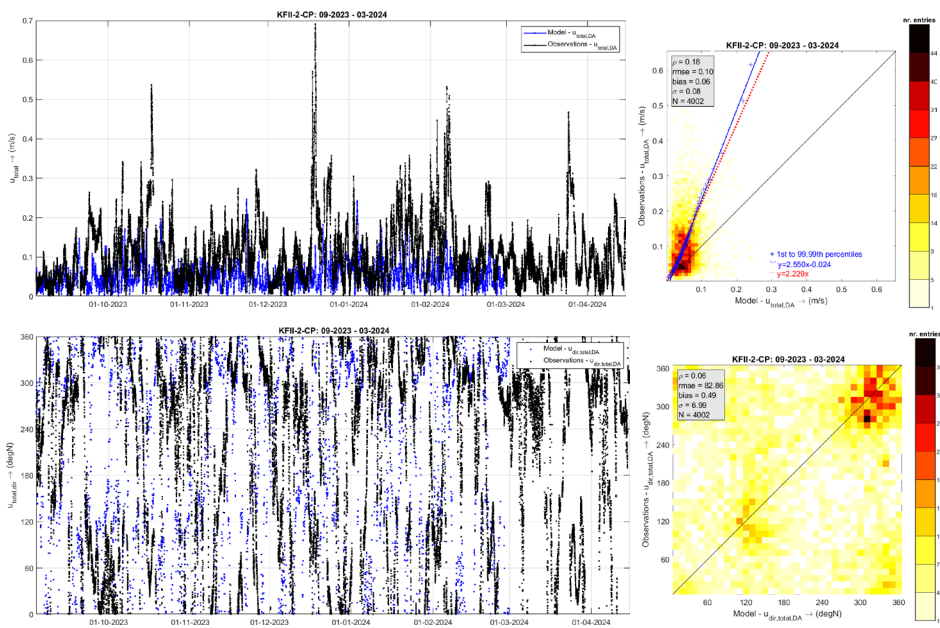


Figure 3-31 Comparisons between the KFII-2-CP and the 2DH model current speeds and directions.

Table 3-6 Current magnitude statistics based on 2DH model results.

Currents	ρ	RMSE	bias	σ	n	r
Darsser-Sill	0.64	0.09	0.06	0.07	66592	1.519
FINO2	0.42	0.08	0.01	0.08	14756	1.129
KFII-1-LB	0.21	0.08	0.05	0.07	1560	1.829
KFII-1-CP	0.13	0.10	0.05	0.08	2590	1.938
KFII-2-CP	0.13	0.10	0.05	0.08	2629	2.303
KFII-2-LB	0.21	0.11	0.07	0.09	2866	2.523

3.3.3.3 Validation of the 3D model results

3.3.3.3.1 Water level comparisons

The validation of the 3D water levels model results has been done in the same way and considering the same observations as for the validation of the 2D model water level results, but only considering data from 2014 onwards, the start of the 3D model computations.

Figure 3-32 to Figure 3-43 show the comparisons between the 3D model water level results and the observations in the Kriegers Flak region. The error statistics are given in the scatter plots and summarised in Table 3-7.

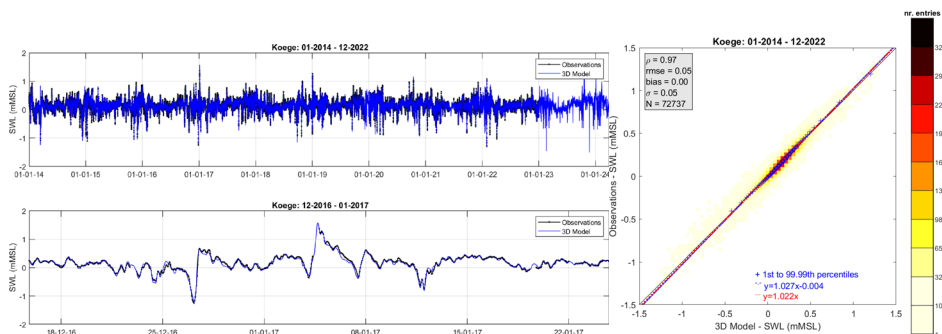


Figure 3-32 Comparisons between the Køge and the 3D model water levels.

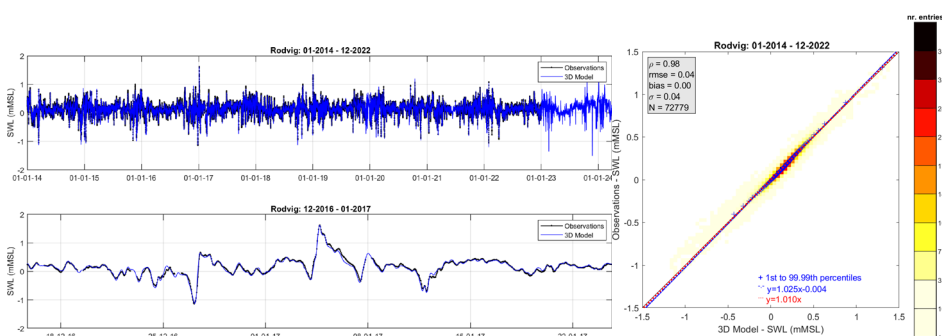


Figure 3-33 Comparisons between the Rødvig and the 3D model water levels.

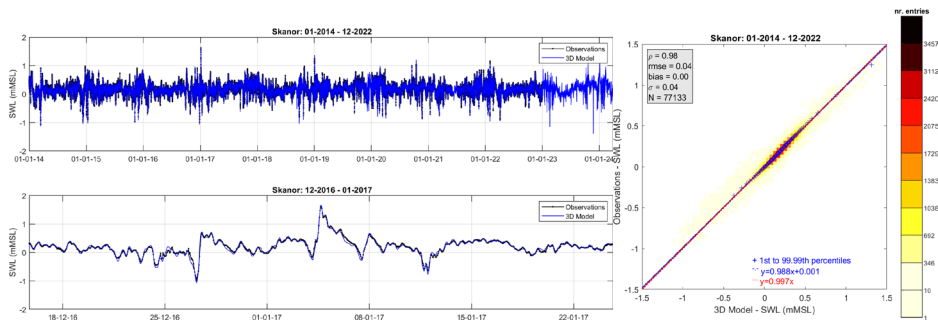


Figure 3-34 Comparisons between the Skanör and the 3D model water levels.

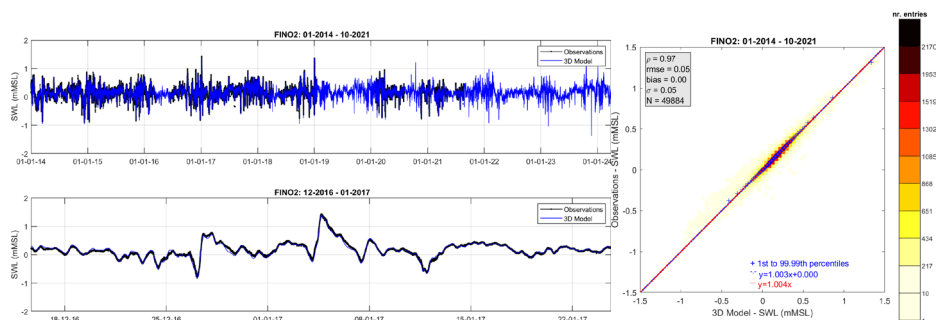


Figure 3-35 Comparisons between the FINO2 and the 3D model water levels.

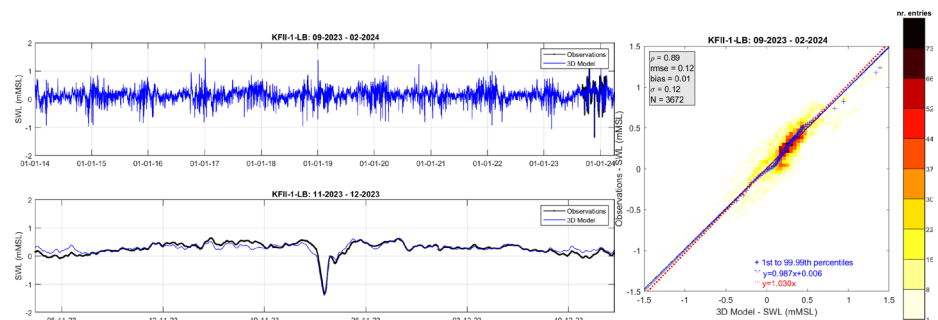


Figure 3-36 Comparisons between the KFII-1-LB and the 3D model water levels.

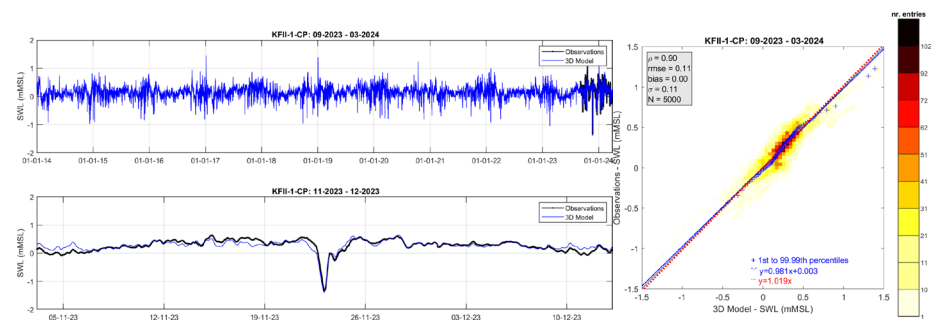


Figure 3-37 Comparisons between the KFII-1-CP and the 3D model water levels.

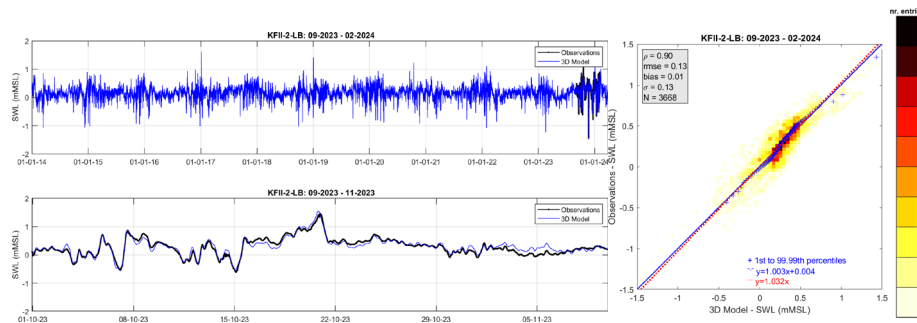


Figure 3-38 Comparisons between the KFII-2-LB and the 3D model water levels.

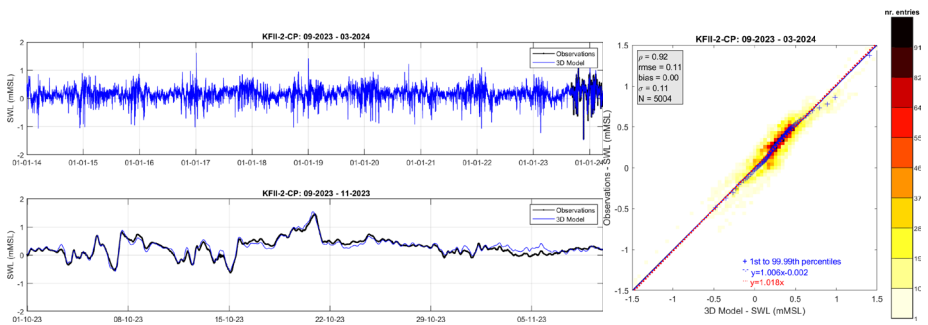


Figure 3-39 Comparisons between the KFII-2-CP and the 3D model water levels.

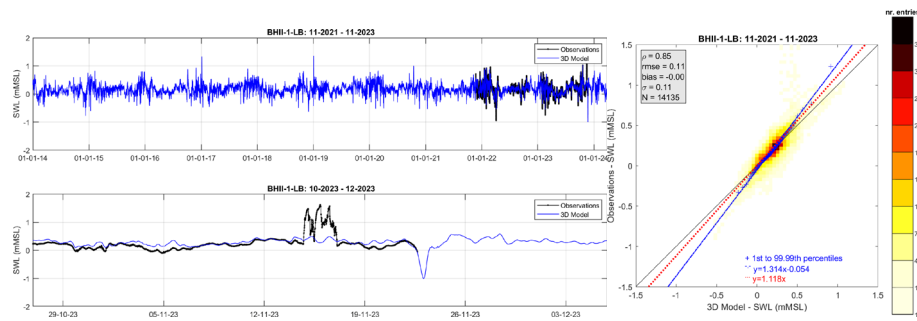


Figure 3-40 Comparisons between the BHI-1-LB and the 3D model water levels.

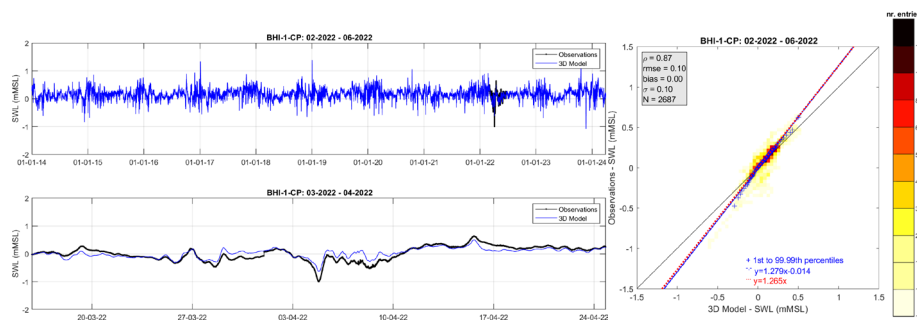


Figure 3-41 Comparisons between the BHI-1-CP and the 3D model water levels.

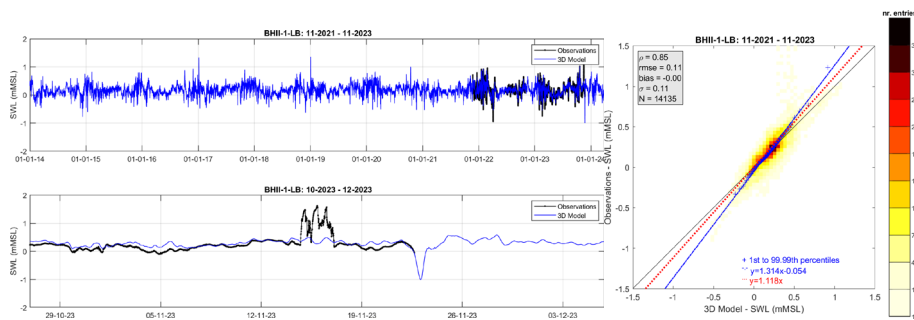


Figure 3-42 Comparisons between the BHII-1-LB and the 3D model water levels.

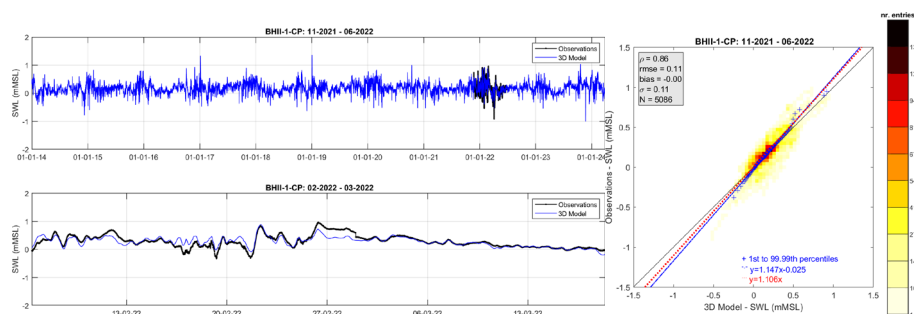


Figure 3-43 Comparisons between the BHII-1-CP and the 3D model water levels.

Table 3-7 Water level statistics based on 3D model results.

Water level	ρ	RMSE	σ	n	r
Skånör	0.98	0.04	0.04	77133	0.997
Køge	0.97	0.05	0.05	72737	1.022
Rødvig	0.98	0.04	0.04	72779	1.010
Hesnaes	0.97	0.05	0.05	67120	0.960
FINO2	0.97	0.05	0.05	49884	0.997
(KFII-1-CP)	0.90	0.11	0.11	5024	1.019
(KFII-1-LB)	0.89	0.12	0.12	3672	1.030
(KFII-2-CP)	0.92	0.11	0.11	5028	1.018
(KFII-2-LB)	0.90	0.13	0.13	3668	1.032
(BHI-1-CP)	0.87	0.10	0.10	2687	1.265
(BHI-1-LB)	0.87	0.10	0.10	7712	1.111
(BHII-1-CP)	0.88	0.11	0.11	4143	1.137
(BHII-1-LB)	0.86	0.11	0.11	13194	1.128

As can be seen in the figures and as expected the performance of the 3D model is even better than that of the 2DH model. The correlations between the model results and observations are high, in particular in the stations with a longer record. In the stations Skånör, Køge, Rødvig, Hesnaes and FINO2, those with

more than 50,000 records, the correlations range between 97 and 98% and the symmetric slopes (r) of the data are close to 1 (0.960-1.022). Given that the symmetric slopes are so close to 1, in principle there is no calibration of the model water level data needed, but as the model shows some underestimation in some of the stations with less data, we also recommend a calibration factor of 1.1 to be applied to the 3D water level model results. Furthermore, these can be used to calibrate the 2D model data and extend the timeseries of the water level data to the period not covered by the 3D model results. Overall, we conclude that the 3D model water levels in the Kriegers Flak region, calibrated using a factor of 1.1 as given in Table 3-8, form a solid basis for further assessments.

Table 3-8 Raw 3D model water level calibration factor.

Variable	Factor
Total water level	1.10

3.3.3.3.2 Current velocity comparisons

We start the validation of the 3D model currents in the same way as for the model currents of the 2D model, by comparing the depth-averaged current speeds and directions from the model and the observations. We then focus on locations Darsser-Sill and KFII-1-CP presenting first the comparisons between the near-surface, mid-depth and near-bottom model and observations and then compare the observed and calibrated model current profiles.

Figure 3-44 to Figure 3-49 show the comparisons between the 3D model depth-averaged currents and the observations in the Kriegers Flak region. The error statistics are given in the scatter plots and summarised in Table 3-9.

As can be seen in the figures the quality of the 3D model results is much higher than of the 2DH model results, but it remains that very low current velocities (lower than 10 cm/s, which is about the expected model accuracy) are not well-captured by the model and also that rare, density driven extreme events (such as Major Baltic Inflow, MBI, cf. Deltares, 2022) are not captured by the model.

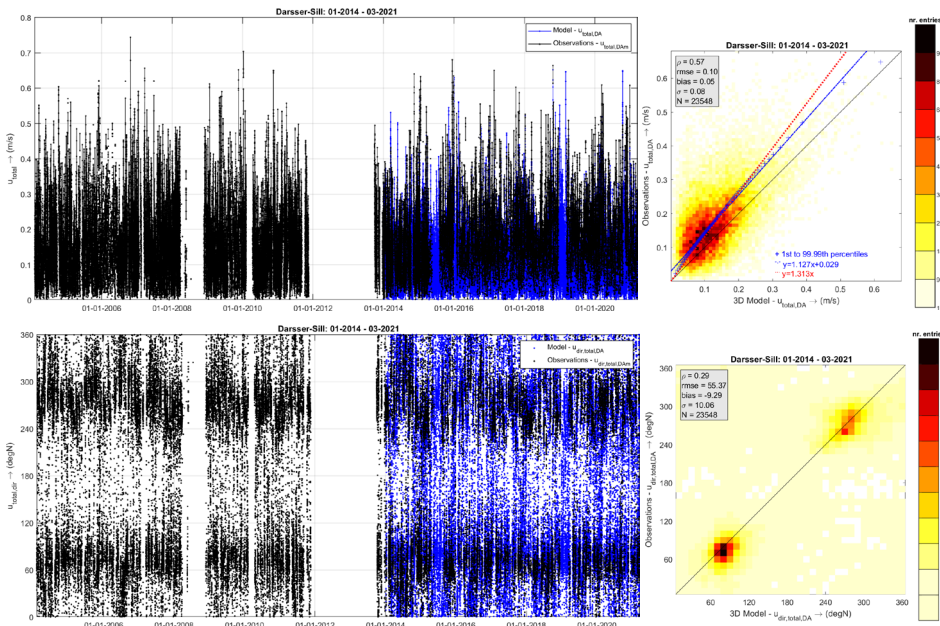


Figure 3-44 Comparisons between the Darsser-Sill and the 3D model current speeds and directions (depth-averaged).

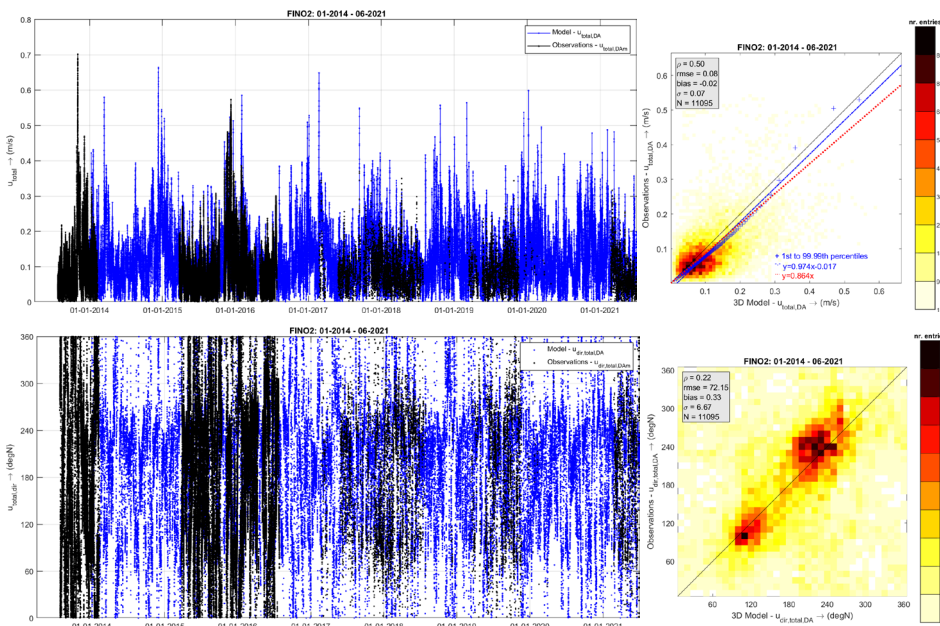


Figure 3-45 Comparisons between the FINO2 and the 3D model current speeds and directions (depth-averaged).

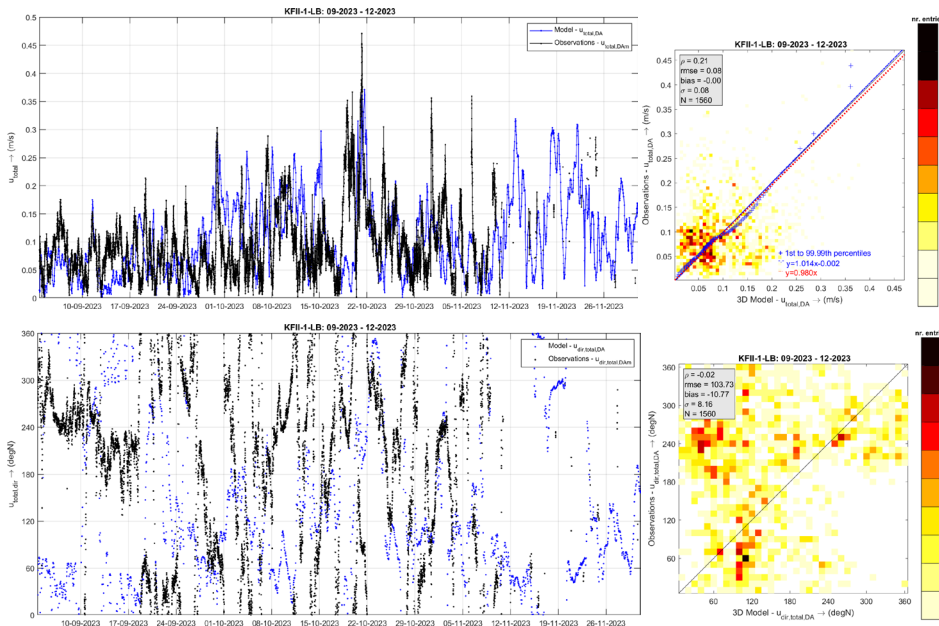


Figure 3-46 Comparisons between the KFII-1-LB and the 3D model current speeds and directions (depth-averaged).

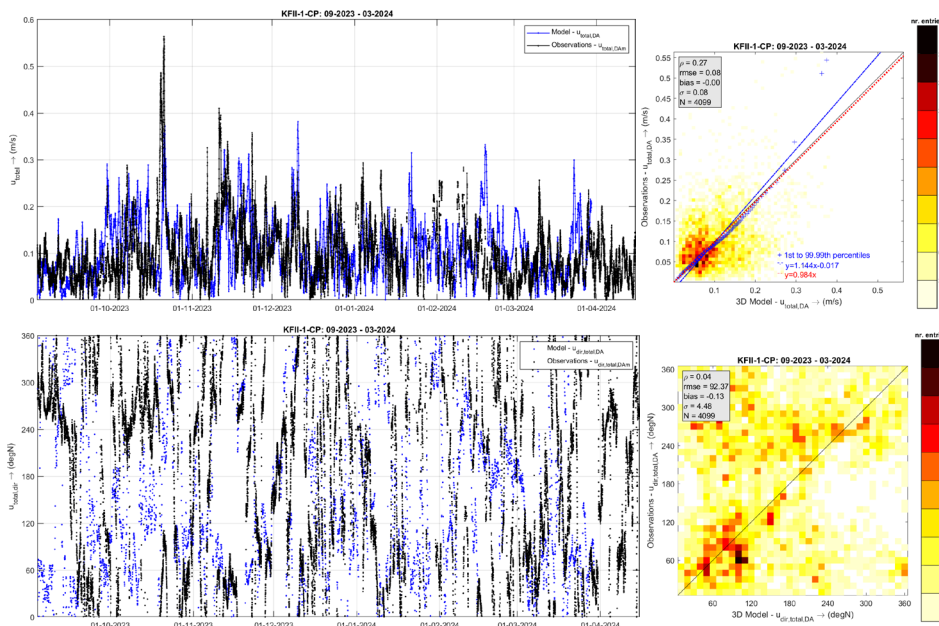


Figure 3-47 Comparisons between the KFII-1-CP and the 3D model current speeds and directions (depth-averaged).

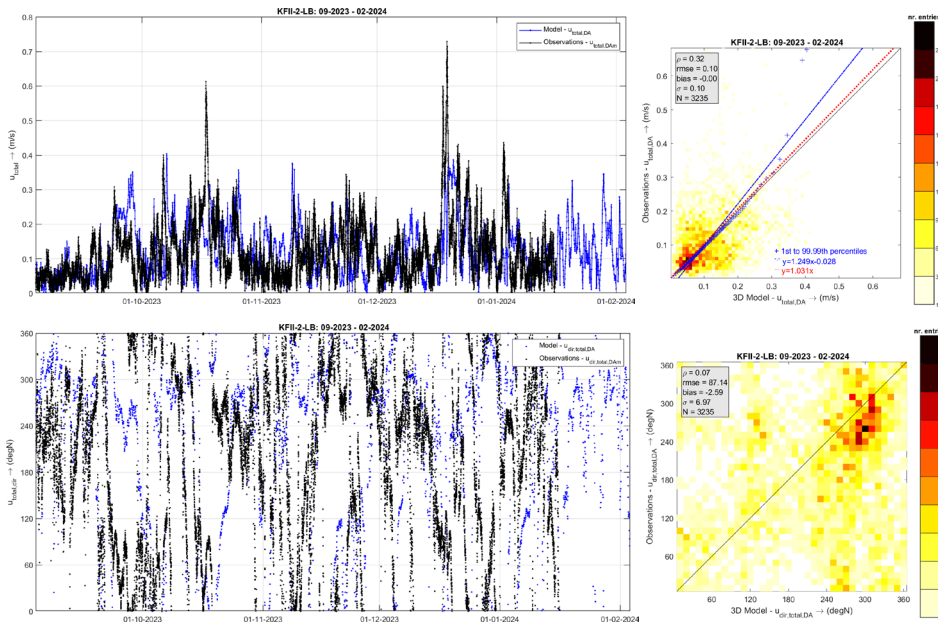


Figure 3-48 Comparisons between the KFII-2-LB and the 3D model current speeds and directions (depth-averaged).

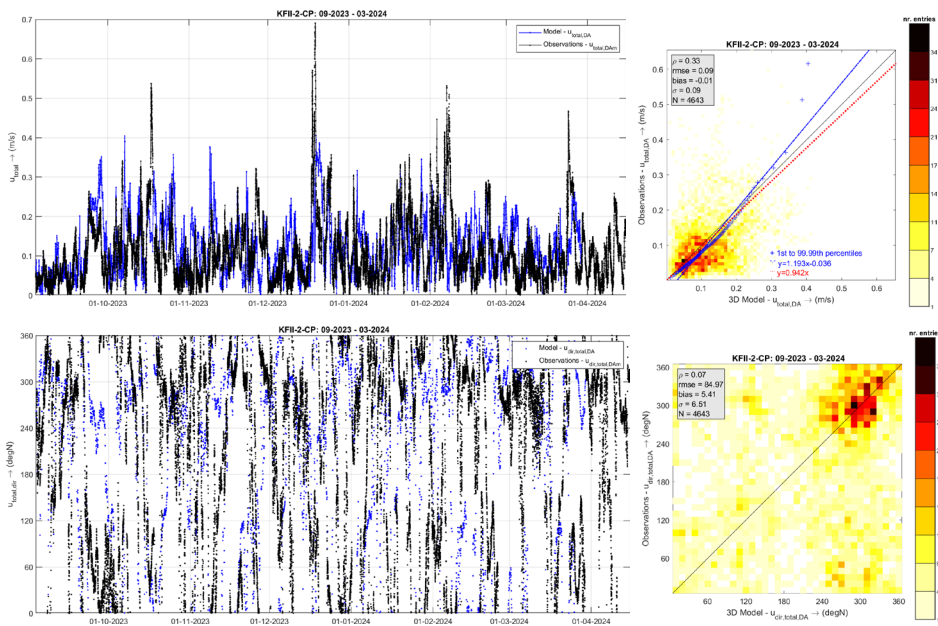


Figure 3-49 Comparisons between the KFII-2-CP and the 3D model current speeds and directions (depth-averaged).

Table 3-9 Depth averaged current magnitude statistics based on 3D model results.

	ρ	RMSE	bias	σ	n	r
Darsser-Sill	0.57	0.10	0.05	0.08	23548	1.313
FINO2	0.50	0.08	-0.02	0.07	11095	0.864
KFII-1-LB	0.21	0.08	0.00	0.08	1560	0.980
KFII-1-CP	0.27	0.08	0.00	0.08	4099	0.984
KFII-2-CP	0.33	0.09	-0.01	0.09	4643	0.942
KFII-2-LB	0.32	0.10	0.00	0.10	3235	1.031

Figure 3-50, Figure 3-51 and Figure 3-52 show the comparisons between the observed and calibrated model near-surface, middle-depth and near-bottom speeds and directions at Darsser-Sill, KF-1-CP and KF-2-CP, respectively. The figures show agreement between the data as also shown in the depth-averaged and profile comparisons and that the underestimation by the model is closely to uniform over depth, with the model showing slightly less underestimation of the near-surface data, which is probably due to instrumental biases in the observations.

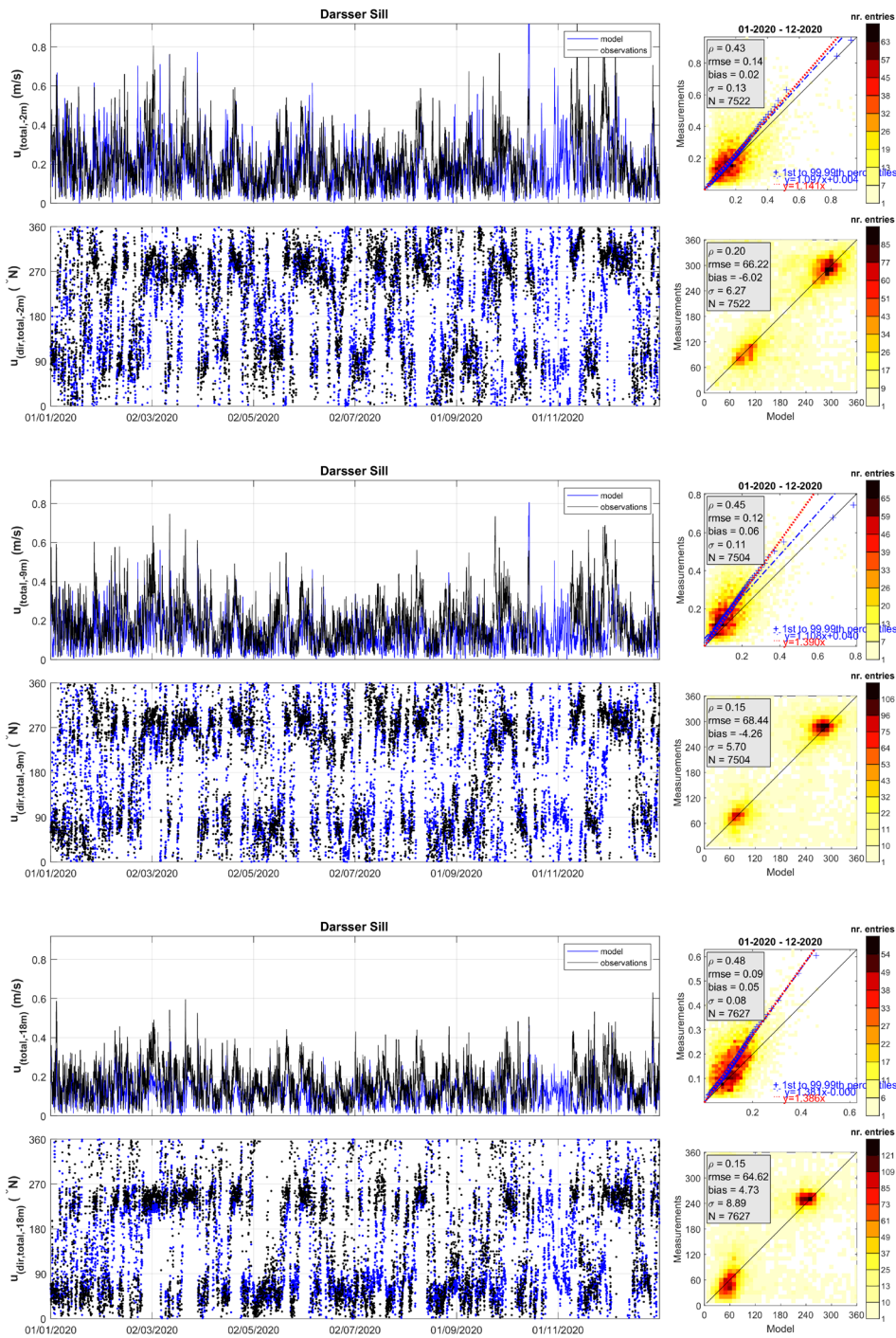


Figure 3-50 Comparisons between the Darsser-Sill and the 3D model current speeds and directions at 2 meters from surface (top) at 9 meters from surface (middle) and at 18 meters from surface (bottom).

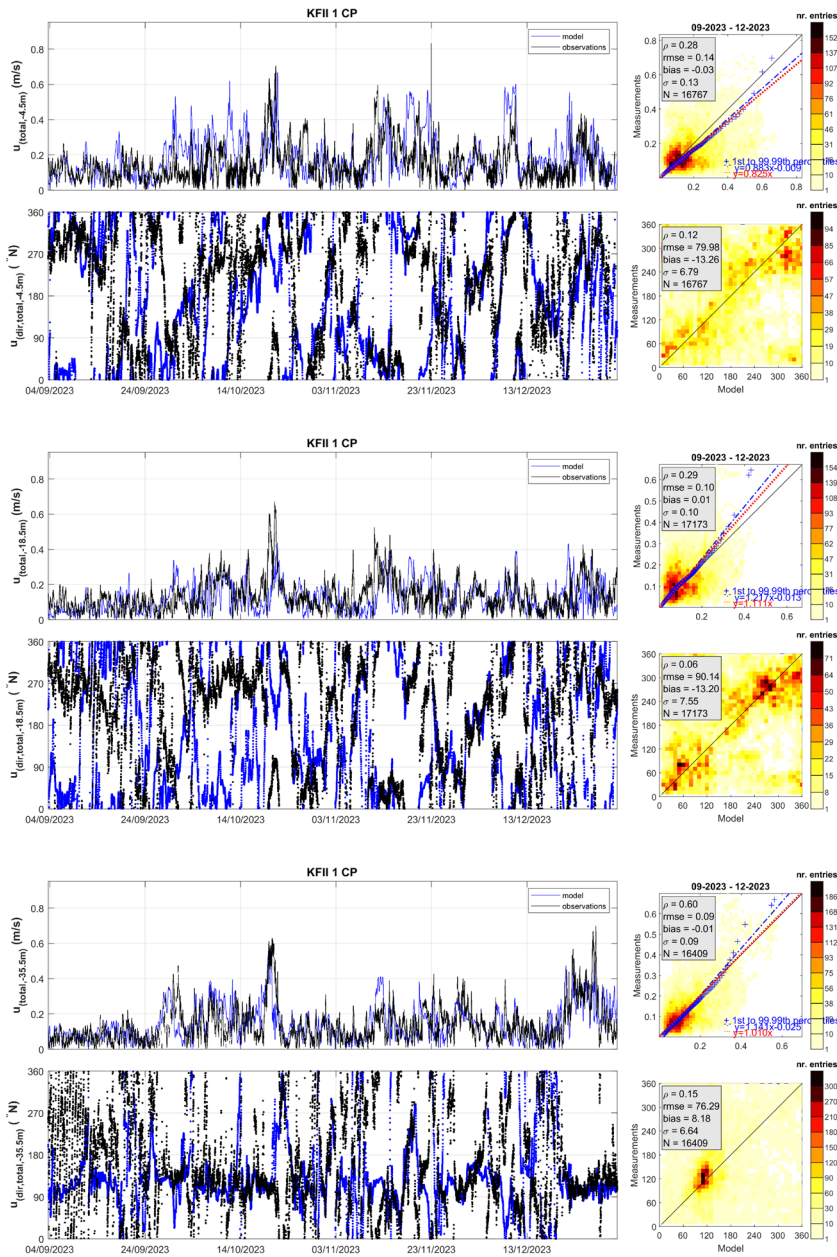


Figure 3-51 Comparisons between the KFII-1-CP and the 3D model current speeds and directions at 4.5 meters from surface (top), at 18.5 meters from surface (middle) and at 35.5 meters from surface (bottom).

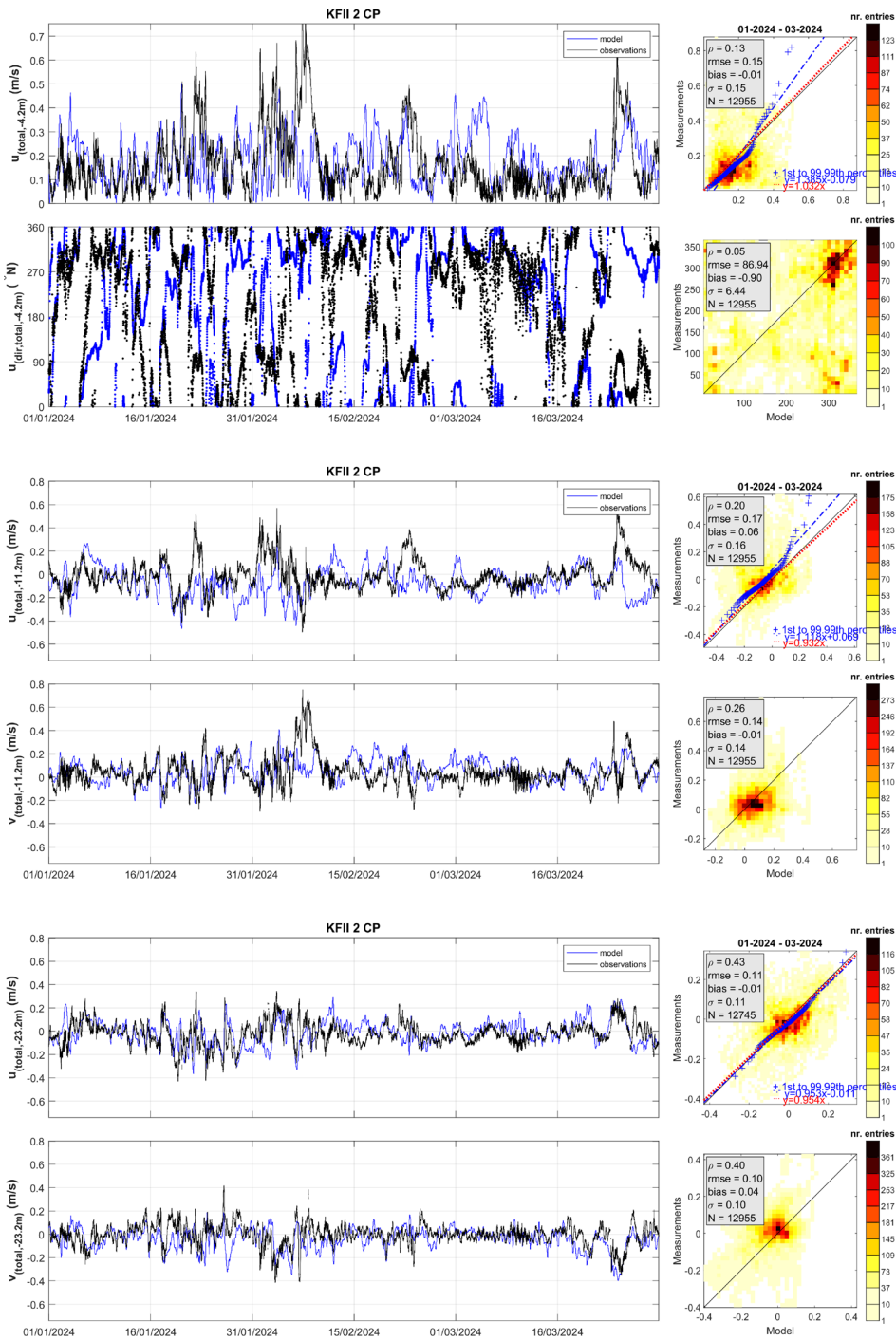


Figure 3-52 Comparisons between the KFII-2-CP and the 3D model current speeds and directions at 4.2 meters from surface (top), at 11.2 meters from surface (middle) and at 23.2 meters from surface (bottom).

Given that the model results at most underestimates the observations by 30% (cf. Table 3-9) and the underestimation appears to occur consistently along the depth profile (except for the surface due to issues in the observations), we

recommend a calibration coefficient of 1.3 to be applied to the current speeds at all levels. Although with large scatter, no systematic deviations are found between the modelled and observed current directions, therefore, we recommend no correction to be applied to the current directions.

Figure 3-53 and Figure 3-54 show the comparisons between the observed and calibrated model current profiles at locations Darsser-Sill and KFII-1-CP and KFII-2-CP, respectively. The figures shows a good correspondence between the profiles, with the calibrated model results on average overestimating the observations at KFII and with at all three locations the calibrated model results at the surface being higher than the observations as expected as the observations are biased due to the effects of the instruments.

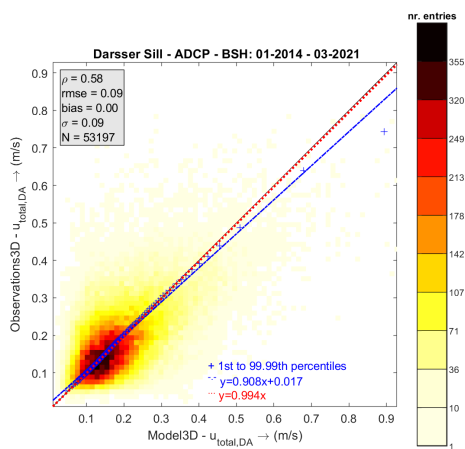
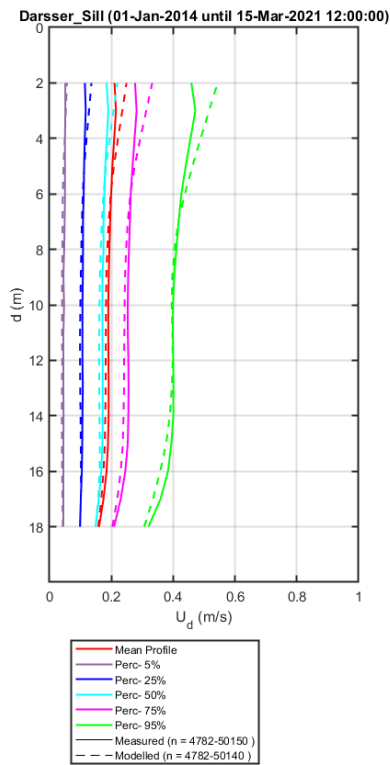


Figure 3-53 Top panel: Current magnitude 3D profile plots comparisons between measurements (full lines) and calibrated 3D model results (dashed lines) at Darsser-Sill. Bottom panel: Comparisons between the corresponding depth-averaged current speeds.

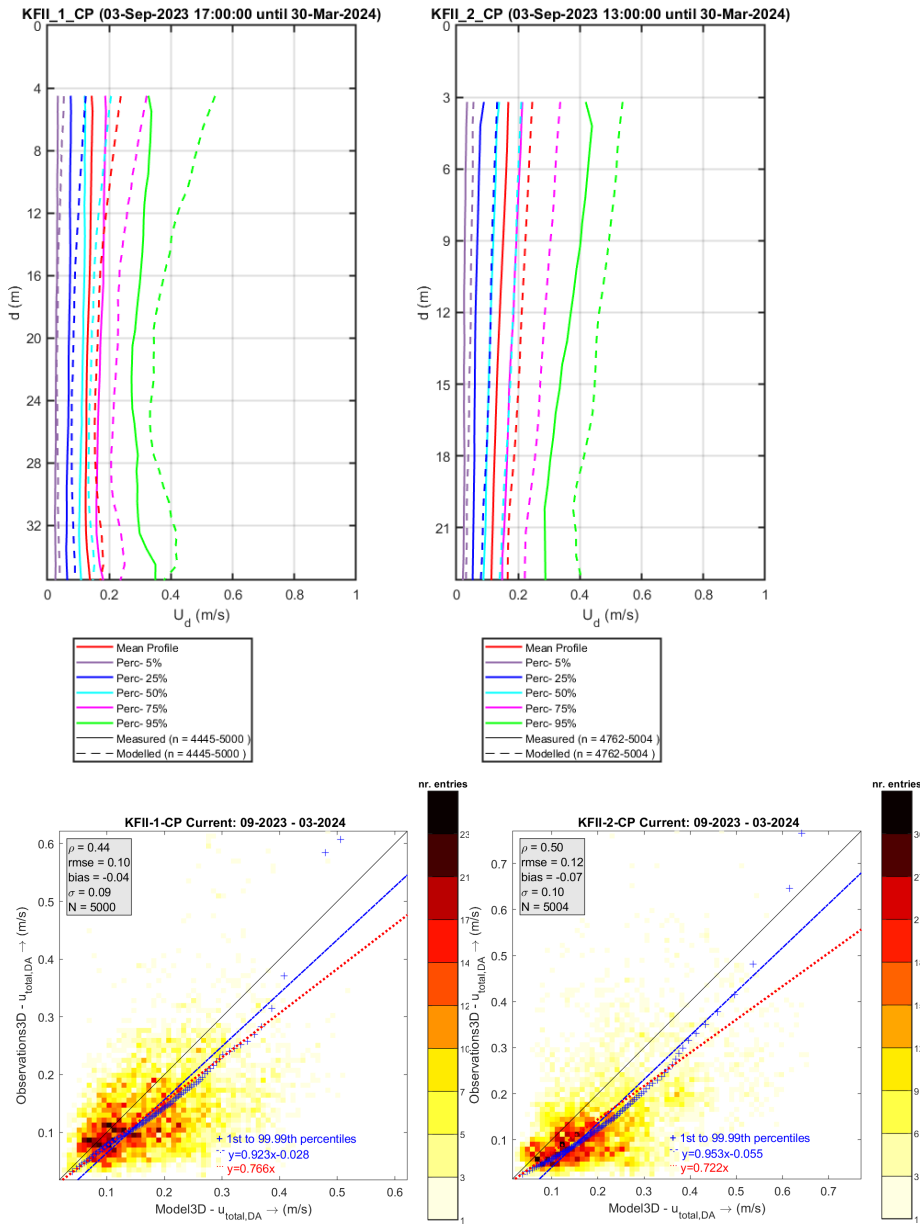


Figure 3-54 Top panels: Current magnitude 3D profile plots comparisons between measurements (full lines) and calibrated 3D model results (dashed lines) at KFII-1-CP (left) and KFII-2-CP (right). Bottom panels: Comparisons between the corresponding depth-averaged current speeds.

For completeness, Figure 3-55, Figure 3-56 and Figure 3-57 show respectively the profile of the KFII-1CP, KFII-2-CP and Darsser-Sill observations when considering all speeds above 0.05 m/s.

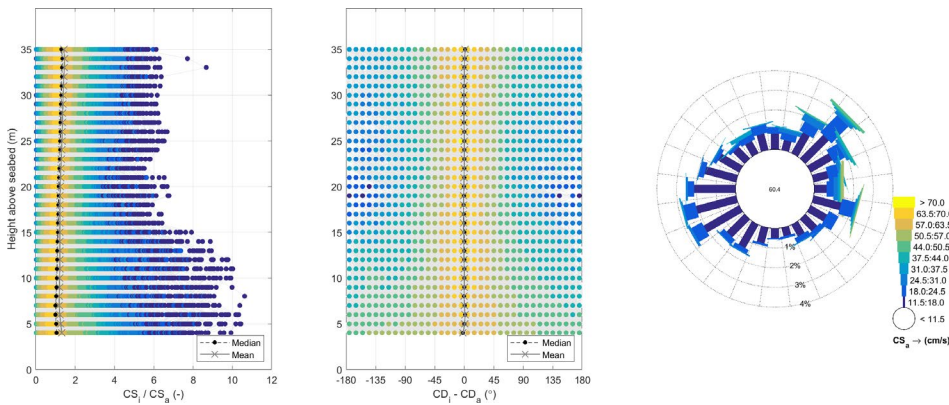


Figure 3-55 KFII-1-CP vertical current speed (left, ratio between the current speed of the layer and the depth-averaged current speed) and direction (middle, rotation between the current direction of the layer and the depth-averaged current direction) profiles and rose of the depth-averaged velocities (right). Only speeds above 0.05 are considered.

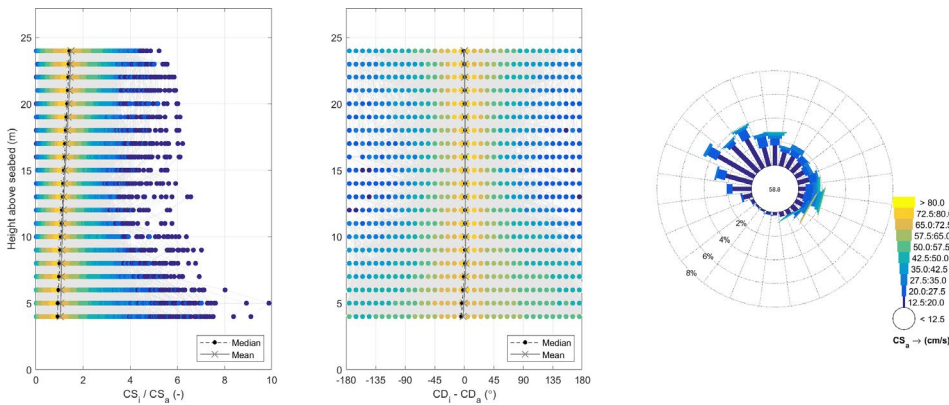


Figure 3-56 KFII-2-CP vertical current speed (left, ratio between the current speed of the layer and the depth-averaged current speed) and direction (middle, rotation between the current direction of the layer and the depth-averaged current direction) profiles and rose of the depth-averaged velocities (right). Only speeds above 0.05 are considered.

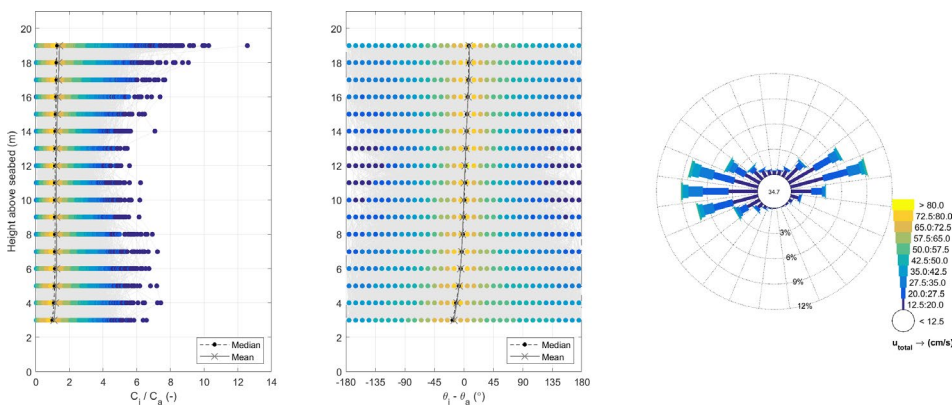


Figure 3-57 Darsser-Sill vertical current speed (left, ratio between the current speed of the layer and the depth-averaged current speed) and direction (middle, rotation between the current direction of the layer and the depth-averaged current direction) profiles and rose of the depth-averaged velocities (right). Only speeds above 0.05 are considered.

Based on the comparisons between the model results and the observations, we conclude that the 3D current velocity model results in the Kriegers Flak region, calibrated using a factor of 1.3, form a solid basis for further assessments. The factors that have been applied are given in Table 3-10.

Table 3-10 Raw 3D model current speed calibration factors.

Variable	Factor
Depth-averaged current speed	1.30
Current speed at each level	1.30

As can be seen in the show figures the prevailing currents are low. In general, on average the depth-averaged current speeds vary between 0.1 m/s to 0.3 m/s. In periods with high winds or density flow the currents can get extremer, but generally with depth averaged values below 0.8 m/s. The most predominant depth-averaged total currents are towards West-Northwest followed by East-northeast.

3.3.4 Determination of vertical current profiles and extension of the 3D data

Although the computational times of the 3D DCSM+Baltic model do not allow for a full long-term detailed modelling of the 3D currents, these have still been derived for the full 45 years period (1979-2023) by means of post-processing the available model results. The determination of current velocities at all layers in the period not covered by the 3D simulations (1979-2013) involved per location:

1. Using the simultaneous 10 years (2014-2023) of calibrated 3D depth-averaged current velocities (with a factor of 1.3 for the speed and the raw directions) to calibrate the 2DH depth-averaged current speeds. The calibration factor applied to the 2DH depth-averaged data is the symmetric slope between the hourly calibrated 3D and raw 2DH depth-averaged current speeds from 2014 until 2023.
2. Using the 10 years (2014-2023) of calibrated 3D current data to determine at each location non-parametric vertical current speed and direction profiles. For each model layer, the coefficient and rotation angle are computed to translate the depth-averaged current speed and direction to the current speed and direction of the layer.
3. Using the hourly 2DH depth-averaged current speed, calibrated using the calibration factor from 1., and depth-averaged current direction from 1979 to 2013 and the profiles from 2. to determine the current speed and direction of each layer.

The profiles of 2. have been determined considering two directional bins of 180 degrees, with one of the bins centred at the mode of the depth-averaged current direction and three bins of current speed: $0.05 \text{ m/s} < CS_{dav} \leq 0.1 \text{ m/s}$, $0.1 \text{ m/s} < CS_{dav} \leq 0.2 \text{ m/s}$ and $CS_{dav} > 0.2 \text{ m/s}$. The factors and rotation angles are determined as the mean on the data falling in the respective bin. Currents from instants in which CS_{dav} is lower than 0.05 m/s in the 2014-2023 period have not been considered in the determination of the profiles. Instants in which CS_{dav} is

lower than 0.05 m/s in the period 1979-2013 are transformed to the model layers using the factors and rotations determined for the respective directional sector and the $0.05 \text{ m/s} < CS_{\text{dav}} \leq 0.1 \text{ m/s}$ bin. Figure 3-58 and Figure 3-59 show the determined profiles for reference location KFIN-2 in Kriegers Flak II North and for reference location KFIS-2 in Kriegers Flak II South.

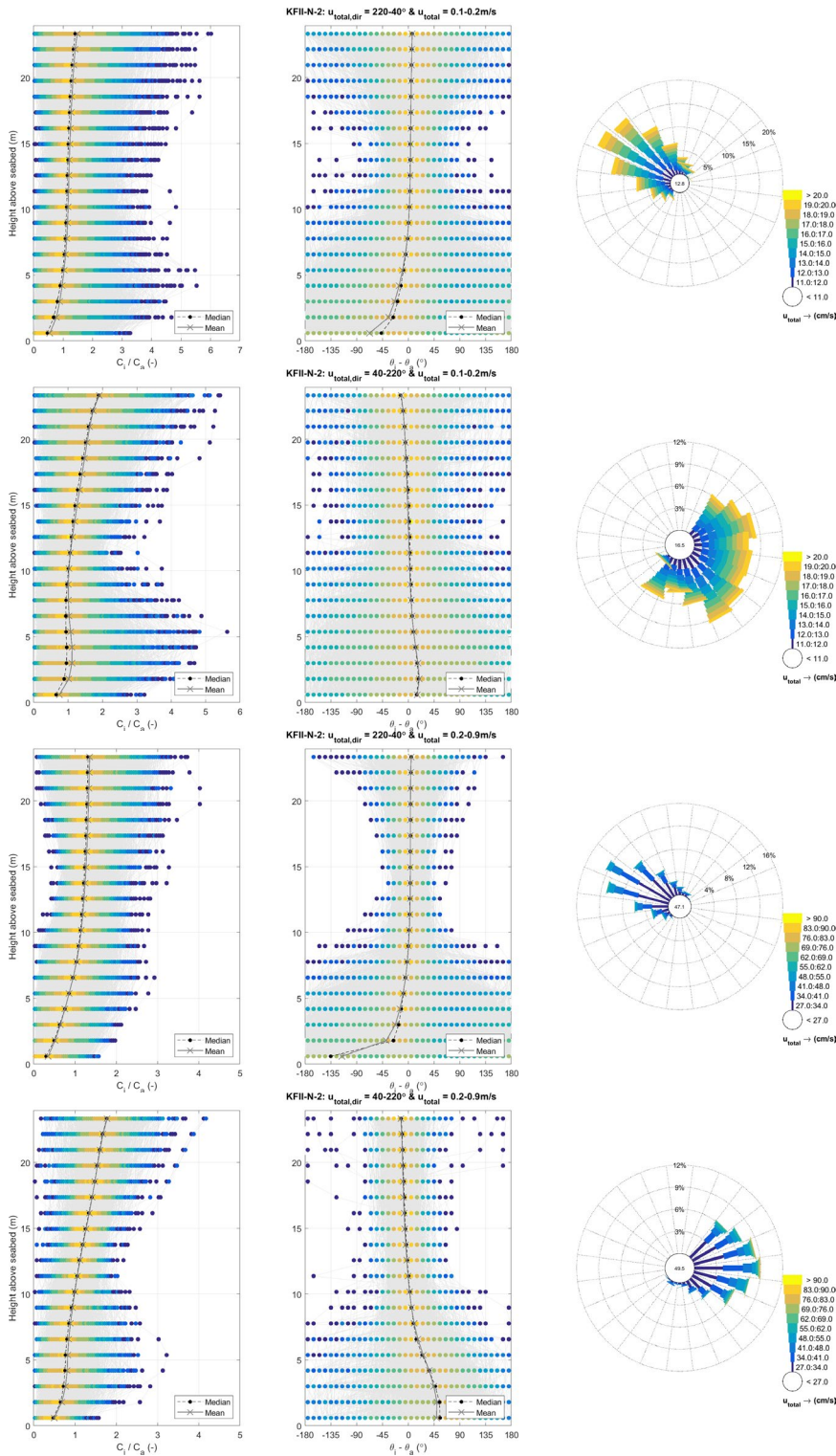


Figure 3-58 KFIIN-2 vertical current speed (left, ratio between the current speed of the layer and the depth-averaged current speed) and direction (middle, rotation between the current direction of the layer and the depth-averaged current direction) profiles and rose of the depth-averaged velocities (right). The top two panels show the results for the 2 directional sectors and depth-averaged current speed class 0.1-0.2 m/s and the bottom two panels show the results for the 2 directional sectors and depth-averaged current speed above 0.2 m/s.

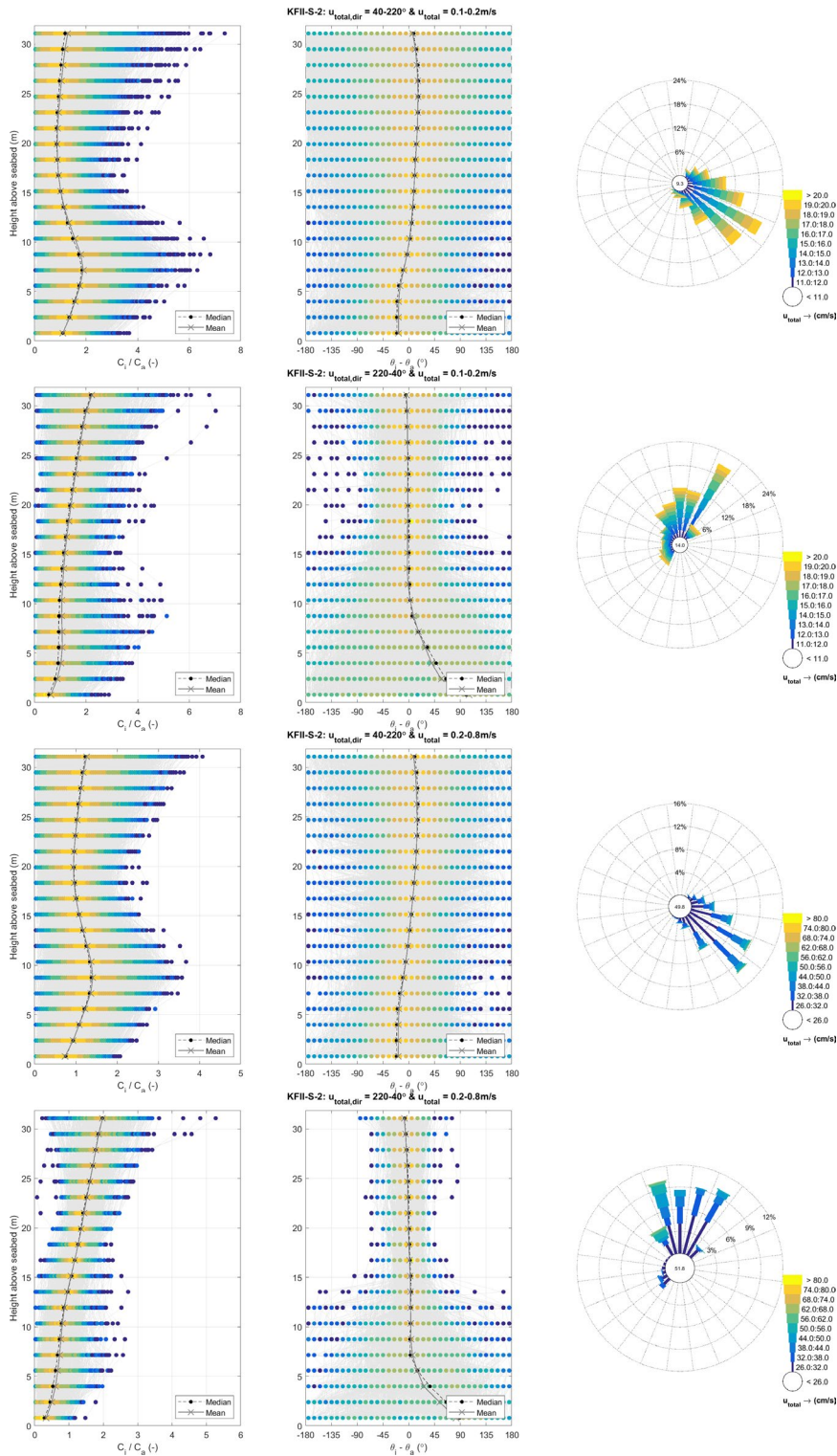


Figure 3-59 KFIS-2 vertical current speed (left, ratio between the current speed of the layer and the depth-averaged current speed) and direction (middle, rotation between the current direction of the layer and the depth-averaged current direction) profiles and rose of the depth-averaged velocities (right). The top two panels show the results for the 2 directional sectors and depth-averaged current speed class 0.1-0.2 m/s and the bottom two panels show the results for the 2 directional sectors and depth-averaged current speed above 0.2 m/s.

3.3.5 Validation of temperature and salinity

The validation of thermodynamic parameters is performed based on the KFII-1-CP and KFII-2-CP near-bottom temperature observations, the KFII-1-LB and KFII-2-LB near-surface temperature observations, and on the available CMEMS temperature and salinity measurement data at a few instances during the year.

Figure 3-60 and Figure 3-61 show the comparisons at KFII-1 and KFII-2, respectively. The figures show a general agreement between the model results and the observations.

Figure 3-62 and Figure 3-63 show comparisons between the model results and observations of temperature and salinity at Arkona during 2014 and 2020, respectively and Figure 3-64 shows comparisons between the model results and observations of temperature and salinity Darsser-Sill during 2022. The figures show a again general agreement between the model results and the observations.

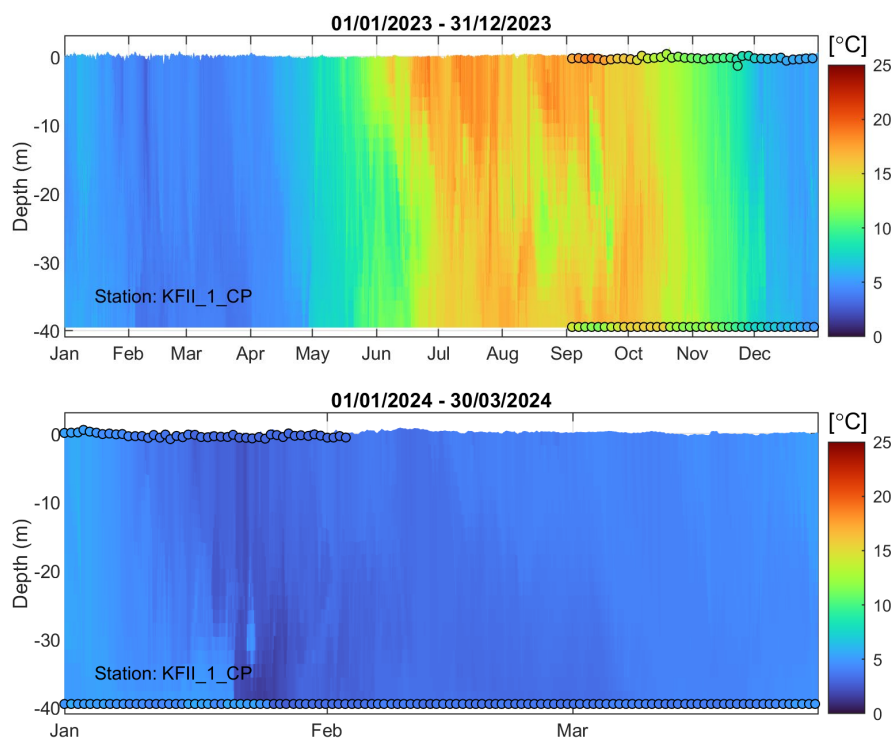


Figure 3-60 Hovmöller diagrams of the 3D temperature model results (background colour map) and near-bottom and near-surface temperature observations (coloured circles) from KFII-1-CP and KFII-1-LB, respectively, from 2023 (top panel) and 2024 (bottom panel).

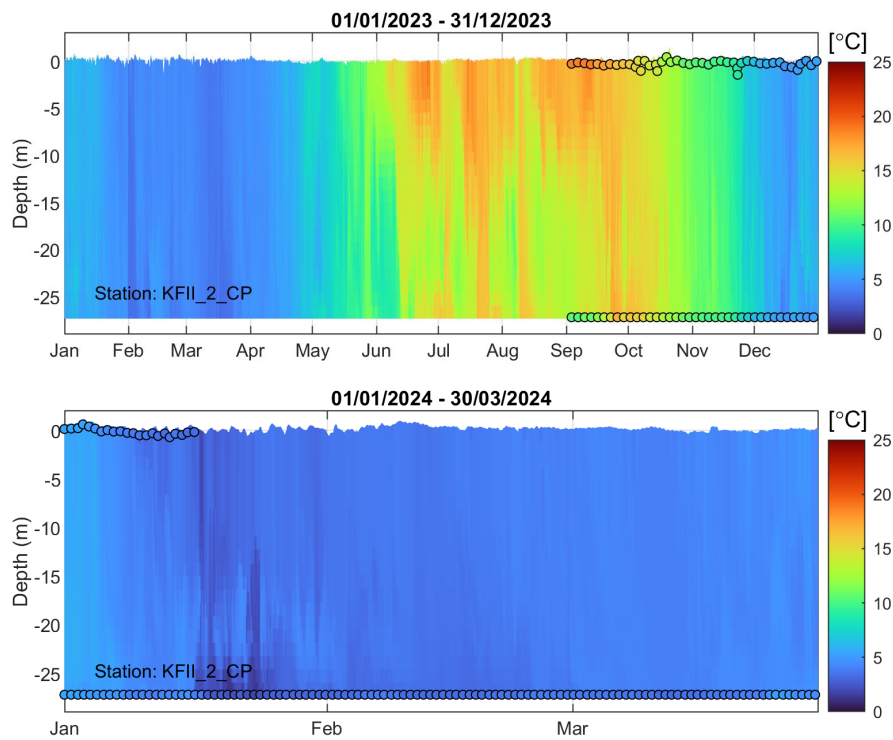


Figure 3-61 Hovmöller diagrams of the 3D temperature model results (background colour map) and near-bottom and near-surface temperature observations (coloured circles) from KFII-2-CP and KFII-2-LB, respectively, from 2023 (top panel) and 2024 (bottom panel).

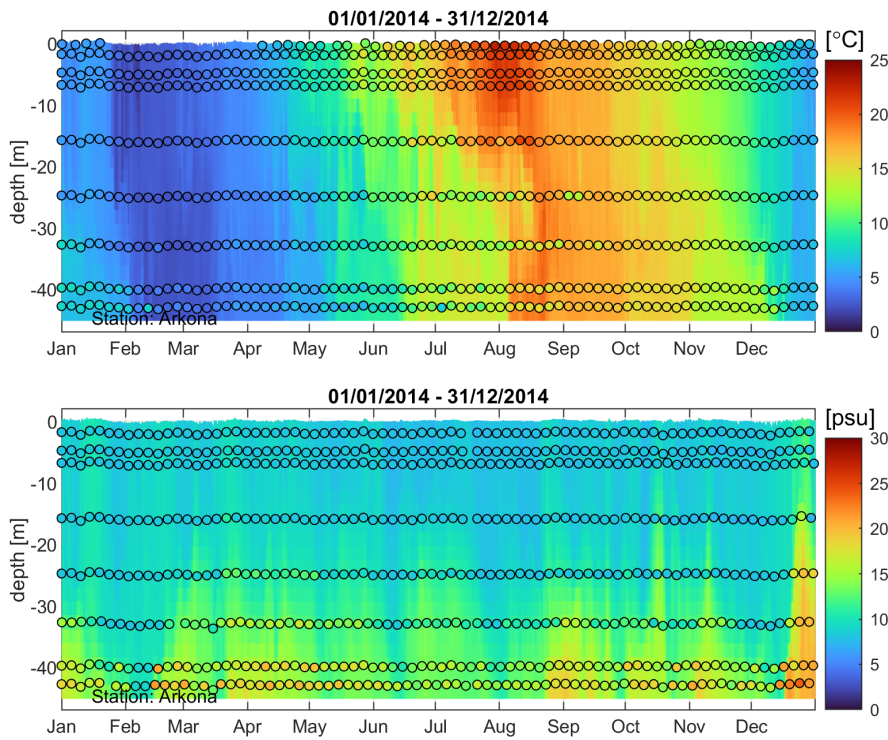


Figure 3-62 Hovmöller diagrams of the 3D model results (background colour map) and observations (coloured circles) of temperature (top) and salinity (bottom) at Arkona during 2014.

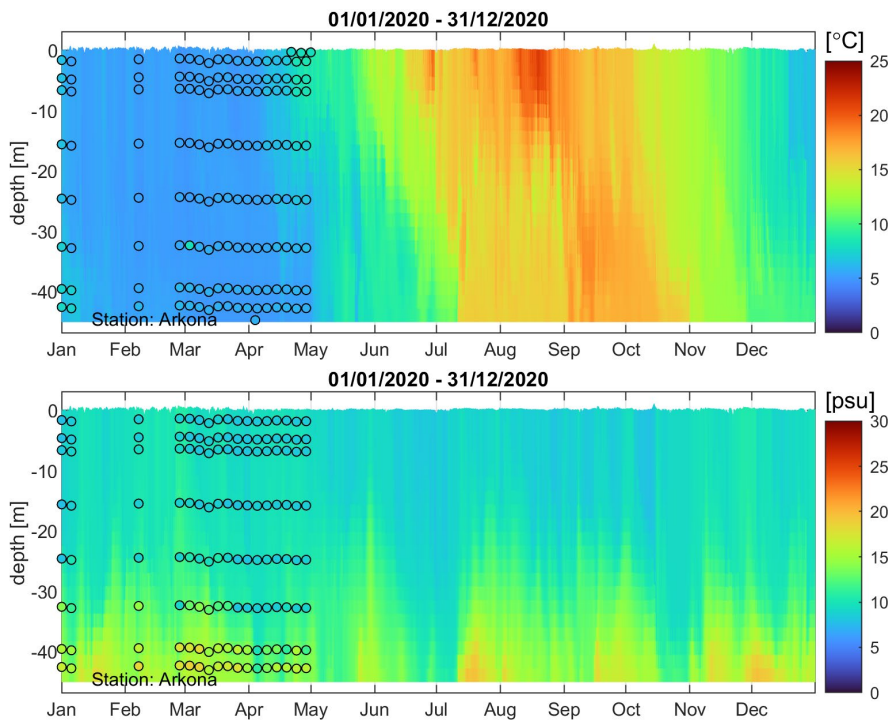


Figure 3-63 Hovmöller diagrams of the 3D model results (background colour map) and observations (coloured circles) of temperature (top) and salinity (bottom) at Arkona during 2020.

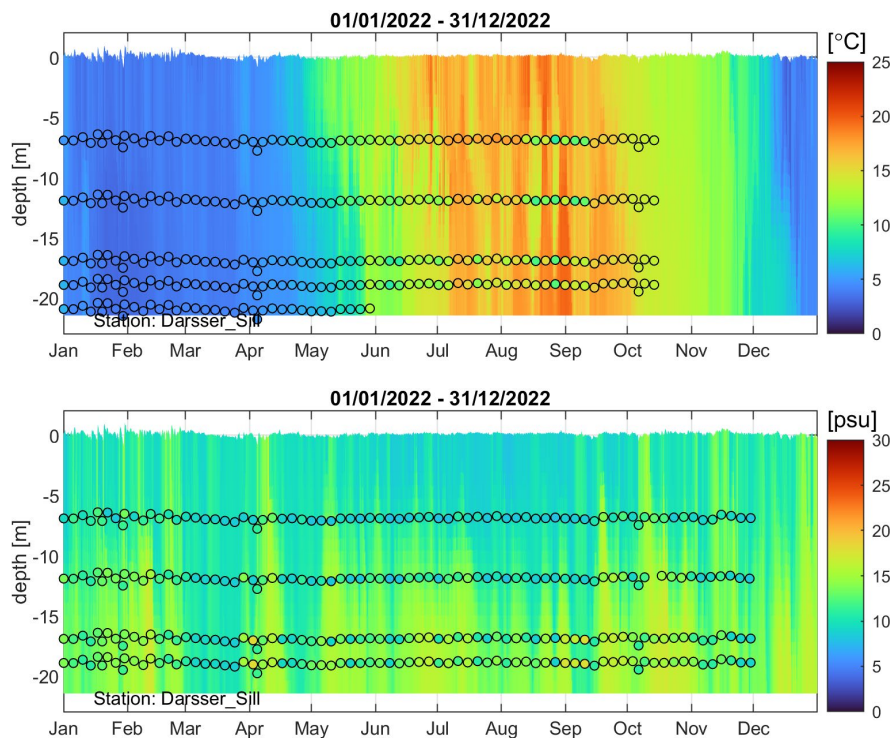


Figure 3-64 Hovmöller diagrams of the 3D model results (background colour map) and observations (coloured circles) of temperature (top) and salinity (bottom) at Darsser-Still during 2022.

Given the shown correspondence, limited availability of observation data and the relatively low, no clear spatial and temporal uniform biases, it has been decided to apply no correction to the model output salinity and temperature values.

3.3.6 The Kriegers Flak II North and South (KFII) OWF water level and current dataset

Based on the validation of the hydrodynamic model results presented in Section 3.3.3 and the extension of the 3D current and water level data timeseries (Section 3.3.4) the hydrodynamic data timeseries were derived. The resulting timeseries are considered to accurately describe the various water level, current and water properties parameters within the area of the KFII OWFs. These timeseries are provided together with this report as NetCDF files at both the reference locations (including tidal and residual components) and at the output locations within the data delivery area and cover the period from 1979 to 2023 (45 years, 01-01-1979 00:00 – 31-12-2023 23:00) at an hourly interval.

The tidal and residual components timeseries given in the reference locations have been obtained from the total timeseries by means of a post-processing step conducted using the T-Tide Harmonic Analysis Toolbox (Pawlowicz et al., 2002). T-Tide is used to determine the tidal signal based on several tide constituents (e.g. M2, S2, O1, K1, etc.) and correcting for the 18.6-year nodal cycle based on the start time of the timeseries and the latitude of the measurement site. The water level analysis was carried out using the hourly total water level timeseries and subtracting the resulting tidal signal from the total water level, to obtain the non-tidal residual. The harmonic analysis of the

currents was carried out on the x- and y-components separately, with the residual per component being computed by subtracting the tidal from the total signal per component.

The contents and naming of the delivered files are as follows:

- **Reference locations:**

Depth-averaged and three-dimensional hydrodynamic data 1979-2023 (6 files each containing data for 1 reference location):

- Water level (total, tidal and residual)
- Total, tidal and residual depth-averaged current (magnitude and direction, going towards)
- Tidal and residual current near-surface, mid-depth and near-bottom (magnitude and direction, going towards)
- Total current per model layer (magnitude and direction, going towards)
- Seawater temperature per layer
- Seawater salinity per layer
- Mid-layer levels

Name: *KriegersFlakIIArea_Point*
name_latitudeN_longitudeE_3D_1979_2023.nc

- **Data delivery area locations:**

Depth-averaged and three-dimensional hydrodynamic data 1979-2023 (9,324 files):

- Water level (total)
- Total depth-averaged current (magnitude and direction, going towards)
- Total current per model layer (magnitude and direction, going towards)
- Seawater temperature per layer
- Seawater salinity per layer
- Mid-layer levels

Name: *KriegersFlakIIArea_latitudeN_longitudeE_3D_1979_2023.nc*

Along with these files a python script is provided that allows the reading and visualization of the data.

The reference point timeseries are used in Part B (SWECO, 2024) of the study as input for the determination of the normal and extreme hydrodynamic conditions.

Please note that within the data delivery area data points along the coastline with depths less than 5 m have been excluded.

3.4 Wave data

The wave modelling performed in this study had as objective to derive accurate wave conditions to be used as input for the metocean assessments. The wave

modelling is described in the next section, the validation and calibration of the model results in Section 3.4.2 and the resulting dataset is summarized in Section 3.4.3.

3.4.1 Wave modelling

Detailed numerical wave modelling was performed using the shallow-water phase-averaging wave model SWAN (Zijlema), to produce long-term timeseries of accurate wave conditions in the KFII OWF area. The high-resolution local numerical wave model was run with ERA5 wind forcing, ERA5 wave boundary conditions and water level and current data from the depth-averaged hydrodynamic model described in Section 3.3.2.

SWAN is widely used for nearshore wave modelling in the international coastal and offshore engineering communities and has been successfully validated under a large variety of field cases and conditions. The software is continually undergoing further development; see www.swan.tudelft.nl for more information. For this study we have used the latest operational version that includes the most recent insights and model developments (SWAN Version 41.45). The model has been run in the unstructured mode, which allows the generation of a boundary fitted grid. Please refer to Appendix B for more general information on the SWAN model.

3.4.1.1 Model domain

SWAN requires the specification of three types of grids:

1. computational grid, which defines the 2D geographical locations of the nodes in the calculation grid;
2. directional grid, which defines the wave directional range (usually 360°) and resolution;
3. spectral grid, which defines the range and resolution of the computations in the wave frequency space.

A single unstructured computational grid (spatial domain) was developed for this study, with a spatial resolution varying between 100 m in the area of interest and about 1.2 kilometres further away. The model domain is shown in Figure 3-65. For reasons of computational efficiency, not all enclosed waters in the area were considered in the model, as the conditions in those areas do not influence the wave conditions reaching the KFII region. Furthermore, the models western boundary is placed on the eastern part of Bornholm. Both the eastern and northern model boundaries, where incoming wave conditions are given (see Section 3.4.1.3), are considered far enough from the area of interest to have no boundary effects in the model results.

The defined directional grid covers the full circle (360°). The number of directional bins was set to 45, resulting in a directional resolution of 8°. This is a typical and often used directional resolution in such wave studies.

The spectral grid of the numerical model covers a frequency range from 0.03 Hz to 1.0 Hz, allowing for representation of wave periods ranging from 1.00 s to 33.33 s. The distribution of the frequencies, f , is logarithmic with a constant relative resolution, $\Delta f/f$, close to 0.1. This results in a total number of frequency bins of 37. This way of distributing the modelled frequencies over the extent of the considered frequency range ensures that the resolution at lower frequencies

is not as coarse as it would have been if an equidistant distribution of frequencies had been applied.

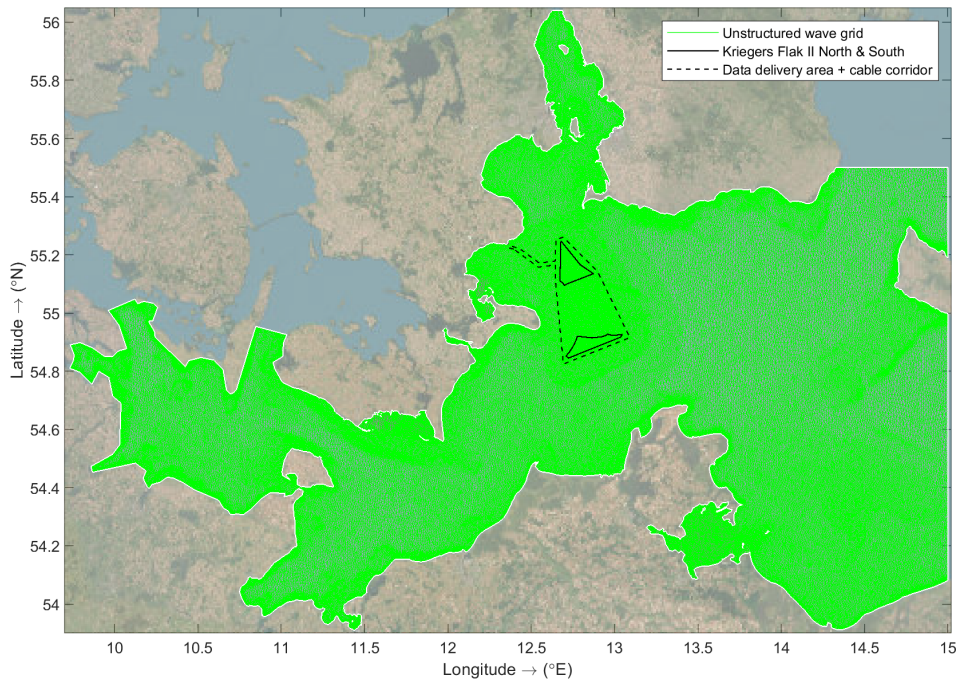


Figure 3-65 Computational SWAN wave model domain and grid.

3.4.1.2 Bathymetry

As for the hydrodynamic model, the bathymetry information for the wave model was based on locally surveyed data provided by the Client (cf. Section 2.3) supplemented by publicly available bathymetry data from the EMODnet dataset from 2022. The bathymetry of the wave model is shown in Figure 3-66 for the full domain and in more detail in the KFII area in Figure 3-67.

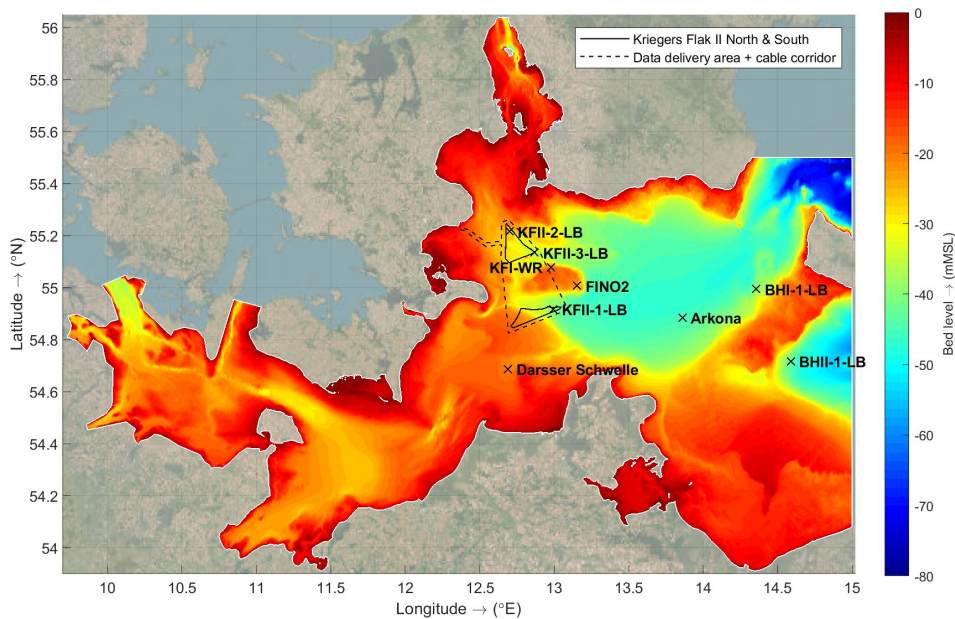


Figure 3-66 Bed levels relative to MSL as used in the computational grid of the wave model including wave observation locations.

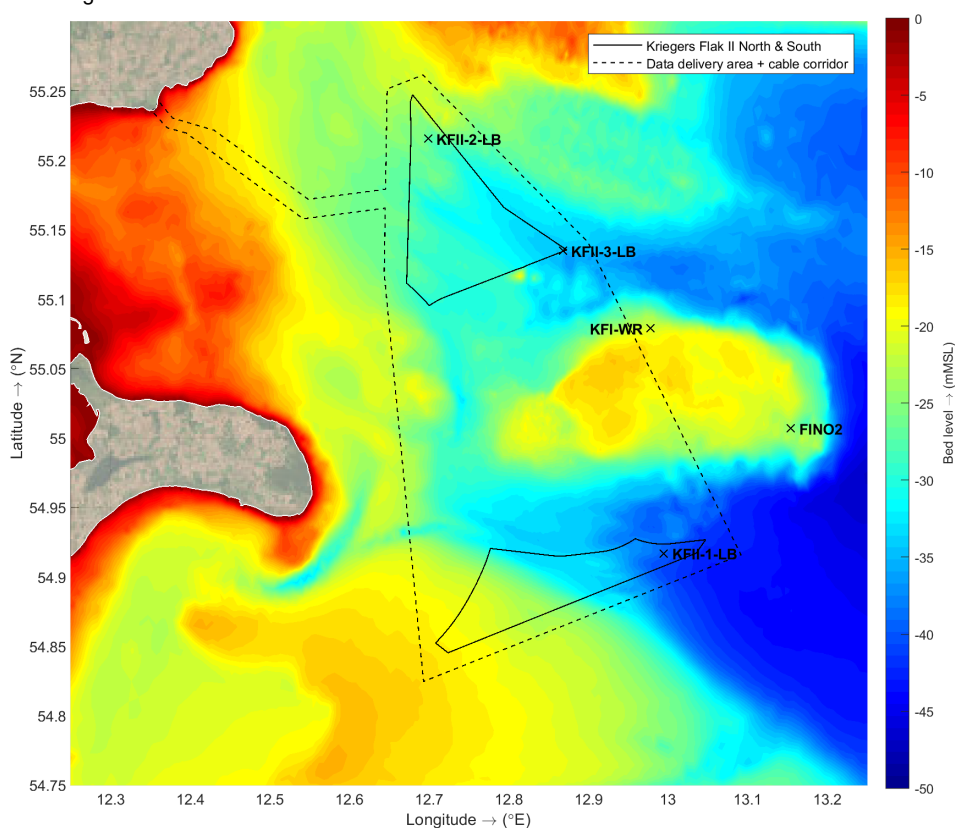


Figure 3-67 Bed levels relative to MSL as used in the surroundings of KFII. Zoom of Figure 3-66

3.4.1.3 Boundary and input conditions

The wave model was run in non-stationary mode (i.e. taking evolution of the wave conditions in time into account) for the period from 1979 to 2023 (45

years, 01-01-1979 00:00 – 31-12-2023 23:00). The model uses a timestep of one hour, which is equal to the time step of the (ERA5) input wind fields. The runs were divided in periods of 6 months with the first 48 hours simulated time being considered as the spin-up period of the model¹³.

Incoming boundary conditions

The SWAN model was forced at the outer boundaries of the overall domain with parameterized wave spectra described by ERA5 timeseries of five wave parameters (described in more detail below this list):

- Significant wave height, H_s
- Peak wave period, T_p
- Mean wave direction (coming from), MWD
- Directional spreading, DSpr
- Spectral shape, γ (an enhancement factor of the peak in the wave spectrum)

The spectral shape, γ , was at the boundary assumed constant and equal to the value of a standard JONSWAP (Hasselmann et al., 1973), $\gamma = 3.3$. The exact value of γ prescribed along the boundary is not critical, since the model will automatically properly redistribute the wave energy in the frequency domain and in balance with the wind forcing. The amount of directional spreading present at the incoming boundaries was derived from the ERA5 timeseries for “wave spectral directional width”. For numerical reasons, this value was capped at a maximum of $\sigma = 37.5^\circ$ (one-sided directional spreading level from the mean direction), which corresponds to a cosine-m power of $m = 1$ in SWAN¹⁴.

Reflecting/transmitting boundaries

No reflecting or transmitting boundaries were defined in the model domain. All wave energy reaching an outer boundary or land boundary is assumed in the model to be fully absorbed at that location. For sloping shorelines and beaches that is a fitting and often applied approach. At the sections bordering enclosed waters waves propagate out of the computational domain uninfluenced (as if they move into these areas).

Wind input

The wave model was forced spatially using the downscaled and calibrated ERA5 wind fields as described in Section 3.2.2.

Hydrodynamics input

The uncalibrated and spatially varying hourly water level and current fields, from the 2DH hydrodynamic model described in Section 3.3.2, have been used as input to the wave model. This means that the wave model accounts for the influence of the spatially distributed water levels and currents (speeds and directions) in the wave propagation and evolution. The reason why the uncalibrated data have been applied is because the wave modelling has been carried out before the calibration of the hydrodynamic data. Any eventual effects of applying the calibrated instead of the uncalibrated data (which are expected to be low) are corrected for in the calibration of the wave model results.

¹³ The spin-up period is the modelling interval which is required for the model to start up and initialise. This includes allowing the wave energy from the boundary to distribute over the total modelling domain. A spin-up period of 48 hours (2 days) is typically used. Results for the spin-up period may not be reliable and are discarded.

¹⁴ This power is used to describe directional distribution shape description according to $\cos^m(\theta)$, with θ representing the wave directions.

3.4.1.4 Numerical and physics parameter settings

This section lists detailed settings for physics parameters and numerical aspects within the SWAN model. It is primarily included here for recording purposes, e.g. for possible future interpretation or reproduction of results. General readers may opt to skip this section.

The modelling was carried out using SWAN, version 41.45, in unstructured and non-stationary mode. The most relevant applied wave physics settings in the computations are:

- Dissipation of wave energy by bottom friction and wave breaking (wave steepness-induced and depth-induced) have both been applied in the SWAN computations.
 - For dissipation by bottom friction the JONSWAP formulation (Hasselmann et al., 1973) with a friction coefficient of $0.038 \text{ m}^2\text{s}^{-3}$ (Zijlema et al., 2012) has been applied.
 - For dissipation by depth-induced wave breaking the Battjes-Janssen formulation (Battjes and Janssen, 1978) with a proportionality coefficient of 0.73 has been applied.
- For representing the effects of white-capping, the formulations by Rogers et al. (2003) have been applied, which is default setting since SWAN version 40.91 (see Appendix B for more details on the formulation).
- For the wind drag the default Wu (1982) approximation of the Charnock relation has been applied (see Appendix B for more details on the formulation).

The criteria for numerical accuracy thresholds were set as follows:

- the computation is finished in case of changes in the second derivative of the iteration curve of the significant wave height are less than 0.6% and the absolute (relative) change in significant wave height from one iteration to the next is less than 1.1 cm (1.1%) at 98% of the grid points, and
- a maximal number of 30 iterations is computed.

These settings mean that the computation will continue until a stable outcome has been reached for the modelled moment in time, with a maximum of 30 iterations to reach the result for that time step. Typically, 30 iteration steps will be sufficient, if not then often a setting in the model is incorrect or the computational grid is not optimal. In the computations performed for the present study, all timesteps after the two days spin-up period have been verified to have converged within 30 iterations (on average even within a much lower number), i.e. the computation has reached the proper numerical outcomes.

3.4.1.5 Output definitions

Timeseries of multiple wave parameters were output by the model at a time step of 1 hour (i.e. the computational time step) within the data delivery area at a large set of locations. In addition, hourly timeseries of wave parameters were also output at observation locations to allow for a detailed validation of the model outcomes. Comparing measured and computed values at those locations gives an indirect verification of the accuracy of the model results in the full model domain.

Further, hourly timeseries of wave parameters and two-dimensional wave variance spectra (describing the wave-energy distribution over frequencies and directions) have been output at the six assessment locations (three per OWF area, cf. Table 2-1).

Last, the maximum wave heights (H_{\max}) and corresponding crest wave heights (C_{\max}) were determined for each of the output locations in a post-processing step. Given that the local maximum waves may be depth-limited, the local model depths in combination with the concurrent water levels were accounted for in this step (the local depths were based on survey data, cf. Section 3.4.1.2).

The maximum wave height (H_{\max}) is defined as the largest wave height in 1,000 waves ($H_{0.1\%}$) during a given sea state. In deep waters the Rayleigh distribution is often assumed for the distribution of wave heights in a sea state. In regions where the highest waves in a sea state may be depth-limited, the Karpadakis et al. (2022) can be applied, which accounts for eventual depth-induced wave breaking. In this study we apply the Rayleigh distribution to determine $H_{0.1\%}$ when the significant wave height is not depth-limited (i.e. $H_s < 0.15 \cdot (d + WL)$) and the Karpadakis et al. (2022) distribution otherwise. For the crest wave height, the second-order Stokes theory is used for when the significant wave height is not depth-limited and the Rienecker and Fenton (1981) theory when it is depth-limited.

For both Karpadakis et al. (2022) and Rienecker and Fenton (1981) the wave period associated with H_{\max} (i.e. $T_{H_{\max}}$) is required as input. Based on an analysis of a large number of measurements, Goda (1978) has shown that the most likely wave period associated with the highest waves in a sea state is closely related to the peak wave period T_p . According to Goda this wave period is 0.9 to 1.0 times T_p . Our standard practice is to take the wave period associated with the maximum wave height ($T_{H_{\max}}$) equal to the peak wave period (T_p), which is also what is done in this study.

3.4.2 Data validation and calibration

The wave timeseries computed by SWAN were validated against available wave observations in the model domain and close to the KFII OWF area. The locations of the considered observation stations are visualized in Figure 3-66. Table 3-1 and Table 3-2 present the time periods covered by the data, the available variables and its provenience. Given the sampling variability of the observations¹⁵, which are available every 1, 10 or 30 minutes, and the spatial scales of the model winds, that correspond to one-hour averages, in order to bring the spatial and time scales of the data together the observations have been averaged from 1 hour before the hour.

For location Darsser-Schwelle and FINO2 (ADCP) the significant wave height observations are available for a longer period than the other wave parameters. Furthermore, although the metadata mention that the peak wave directions were stored at locations Darsser-Schwelle, Arkona and FINO2 (ADCP and buoy), the observations correlate better with the modelled mean wave directions than with the modelled peak wave directions. The model mean wave directions have therefore been validated against the observed peak wave directions.

¹⁵The sea surface elevation is generally observed for periods of about 20 minutes and from these observations the wave spectrum is computed and the integral wave parameters, such as the significant wave height are computed.

Figure 3-68 to Figure 3-77 show the density scatter and percentile comparisons and the main statistics of the data comparisons such as the correlation coefficient, root-mean-square errors, bias and standard deviation. For each station there is a figure with the omni-directional significant wave height comparisons and when available with the peak wave period, the zero-crossing wave period ($T_{m0,2}$) and the mean wave direction comparisons (cf. Table 3-1 and Table 3-2).

The figures show good to excellent correlations between the wave model results and the observations and some overestimation of the significant wave height peaks. The scatter in the T_p and MWD comparisons is higher than for the other variables due to the discrete nature of the data. However, when only considering higher wave height conditions (i.e. $H_s \geq 1$ m), this scatter largely disappears, and the correlations increase. Furthermore, in terms of MWD, the figures show a bias over the full range of directions between the MWD model results and observations from all three wave buoys of the KFII campaign (e.g. Figure 3-69). As such biases are lower in the comparisons with observations from other campaigns (e.g. Figure 3-71), these are most likely due to an offset in the observation data that has not been accounted/corrected for by the surveyor (e.g. due to a declination error, which for this area is $\approx +5^\circ$ in October 2023). If these mismatches would have been caused by inaccuracies in the model bathymetry, one would not see a constant offset over the full range of directions, but rather a local offset for a limited range of directions. These offsets will therefore not be corrected for.

Moreover, it should be noted that the apparent mismatches found for the zero-crossing wave period data are only due to the difference in frequency ranges considered by the buoys (0.04-0.5 Hz) and the wave model (0.03-1.0 Hz). When only considering wave model data falling within the same frequency range as the observations, the matches become much better. This is shown for KFII-1-LB and KFII-2-LB in the lower panels of Figure 3-68 and Figure 3-69 respectively.

The comparisons also show the appropriateness of the models eastern and northern boundaries (see Section 3.4.1.1). As can be seen in the comparisons between the model results and the measurements at the locations that are relatively close to the boundary, the Bornholm and Arkona buoy locations, the correlations are high and the required corrections for the wave height are in the same order of magnitude as for the Kriegers Flak buoys. Making the model larger (and the computations longer), would thus not enhance the results further.

Having considered all comparisons in detail it has been concluded that the model significant wave height data show some overestimation of the high significant wave height percentiles, which should be corrected for. At the KFII OWF buoy this comes down to a general correction factor of 0.9 for the significant wave height. To maintain the deep-water wave steepness, the concurrent peak and mean wave periods are also corrected with a factor equal to $\sqrt{0.9}$. The calibrated SWAN results are considered to properly reflect the wave conditions in the considered calibration area. Figure 3-78 to Figure 3-80 show the density scatter plots for the corrected model data of respectively locations KFII-1-LB, KFII-2-LB and KFII-3-LB.

Also, from the consideration of all other comparisons in detail, we have concluded that the SWAN mean wave directions already properly reflect the

corresponding values in the considered calibration area: i.e. there is no need for a correction of these SWAN wave directions.

The factors that have been applied to the wave model results are given in Table 3-11.

Table 3-11 Raw wave model calibration factors.

Variable	Factor
Significant wave height	0.9
Wave period	$\sqrt{0.9}$

In addition to all density scatter plots for the various locations, also timeseries comparison plots of storm Babet (20-21 October 2023) are shown for LiDAR buoys KFII-1-LB and KFII-2-LB in Figure 3-81 and Figure 3-82 respectively. The figures show both the raw and calibrated model timeseries and the good match between the calibrated model data and the observations.

Last, Figure 3-83 and Figure 3-84 show 1D wave spectra comparison plots of the wave conditions during the peak of storm Babet. Note that only the raw model data are shown here. The plots show that SWAN is well capable to correctly capture the spectral shape of the sea state during the peak of the storm (with some overestimation, as expected given that only raw data are plotted).

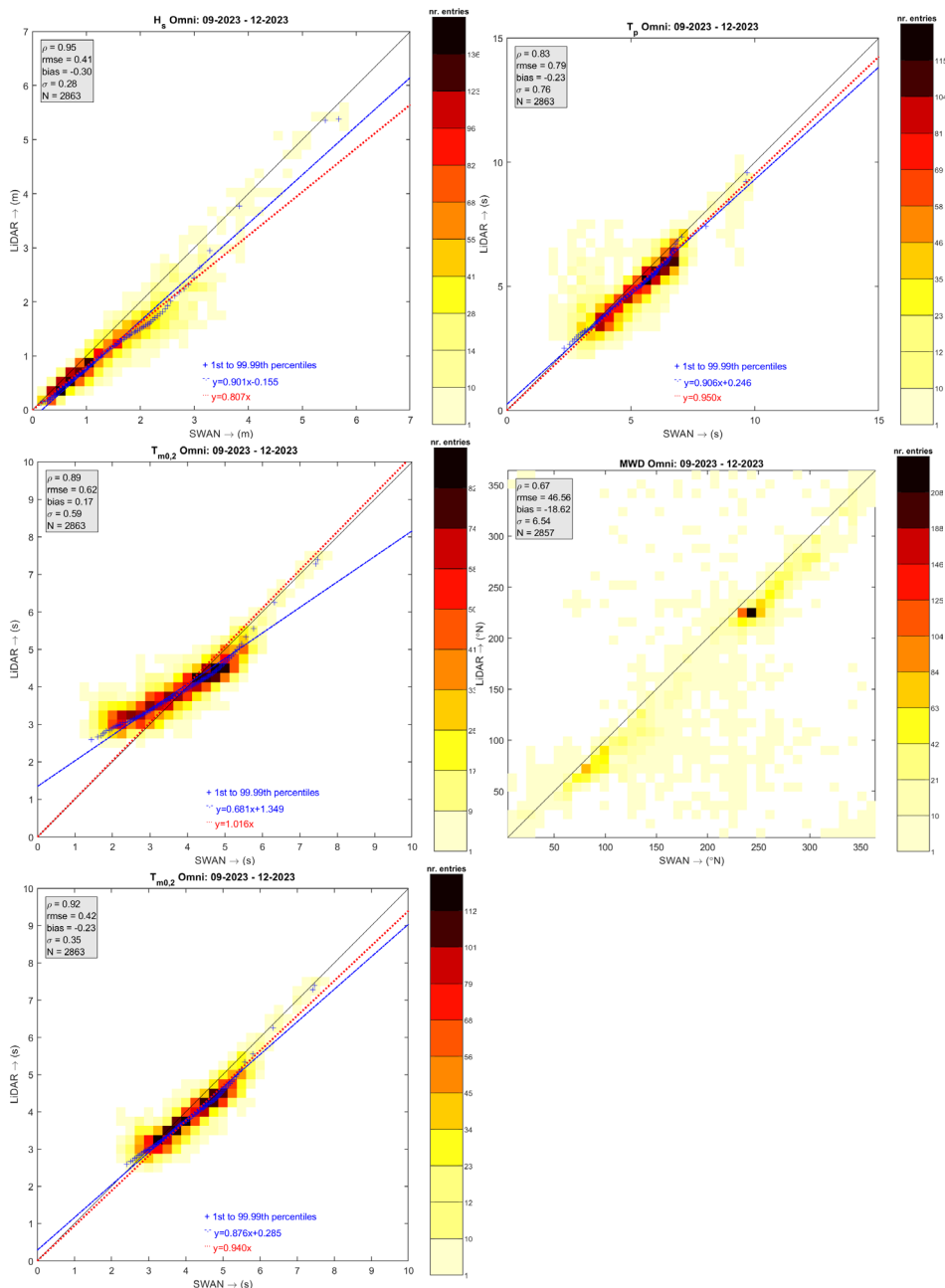


Figure 3-68 Density scatter comparisons (all data) between the buoy observations and the (raw) SWAN results at KFII-1-LB (Kriegers Flak II South OWF). Top left: significant wave height, top right: peak wave period, middle left: zero-crossing wave period (full frequency range, 0.03-1.0 Hz), middle right: mean wave direction, bottom left: zero-crossing wave period (limited frequency range, 0.04-0.5 Hz). The symmetric fit to the data is given by the red dotted line and the linear fit through the data percentiles (blue pluses) is given by the dashed blue line. The statistics of the comparisons are printed in the panels.

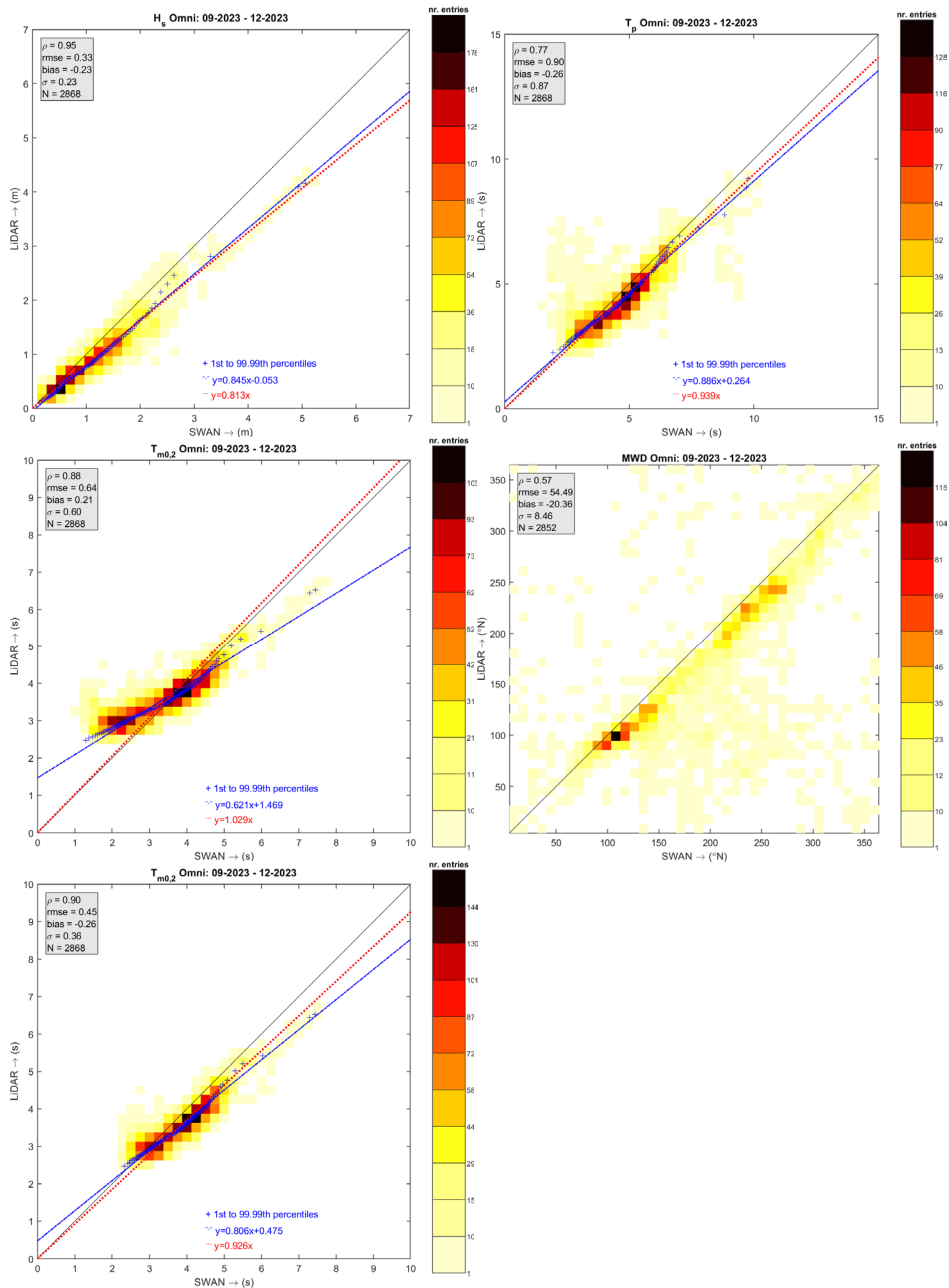


Figure 3-69 Density scatter comparisons (all data) between the buoy observations and the (raw) SWAN results at KFII-2-LB (Kriegers Flak II North OWF). Top left: significant wave height, top right: peak wave period, middle left: zero-crossing wave period (full frequency range, 0.03-1.0 Hz), middle right: mean wave direction, bottom left: zero-crossing wave period (limited frequency range, 0.04-0.5 Hz).

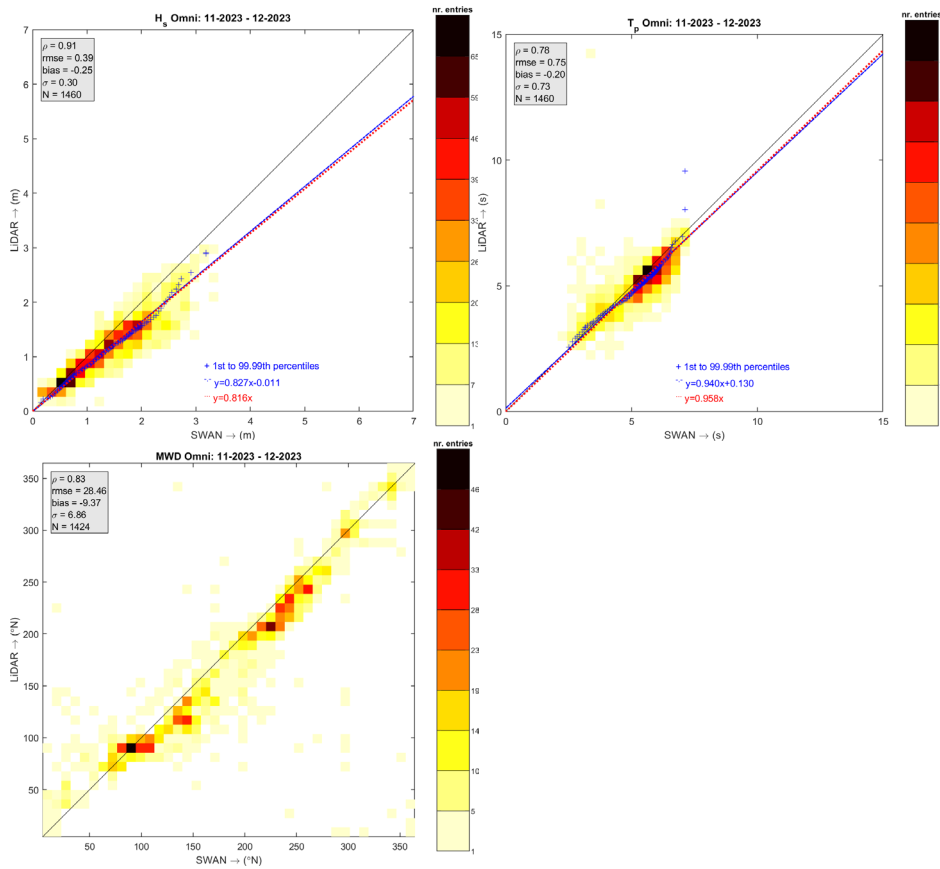


Figure 3-70 Density scatter comparisons (all data) between the buoy observations and the (raw) SWAN results at KFII-3-LB (Kriegers Flak II North OWF). Top left: significant wave height, top right: peak wave period, bottom left: mean wave direction.

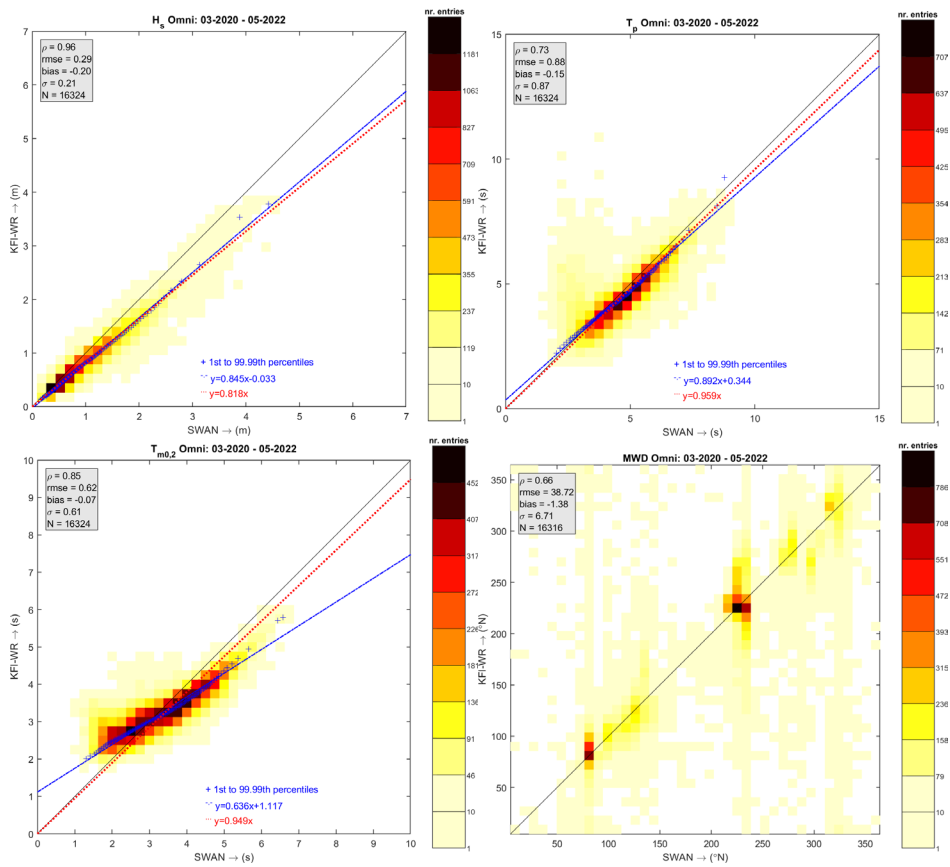


Figure 3-71 Density scatter comparisons (all data) between the buoy observations and the (raw) SWAN results at KFI-WR (Kriegers Flak I OWF). Top left: significant wave height, top right: peak wave period, bottom left: zero-crossing wave period, bottom right: mean wave direction.

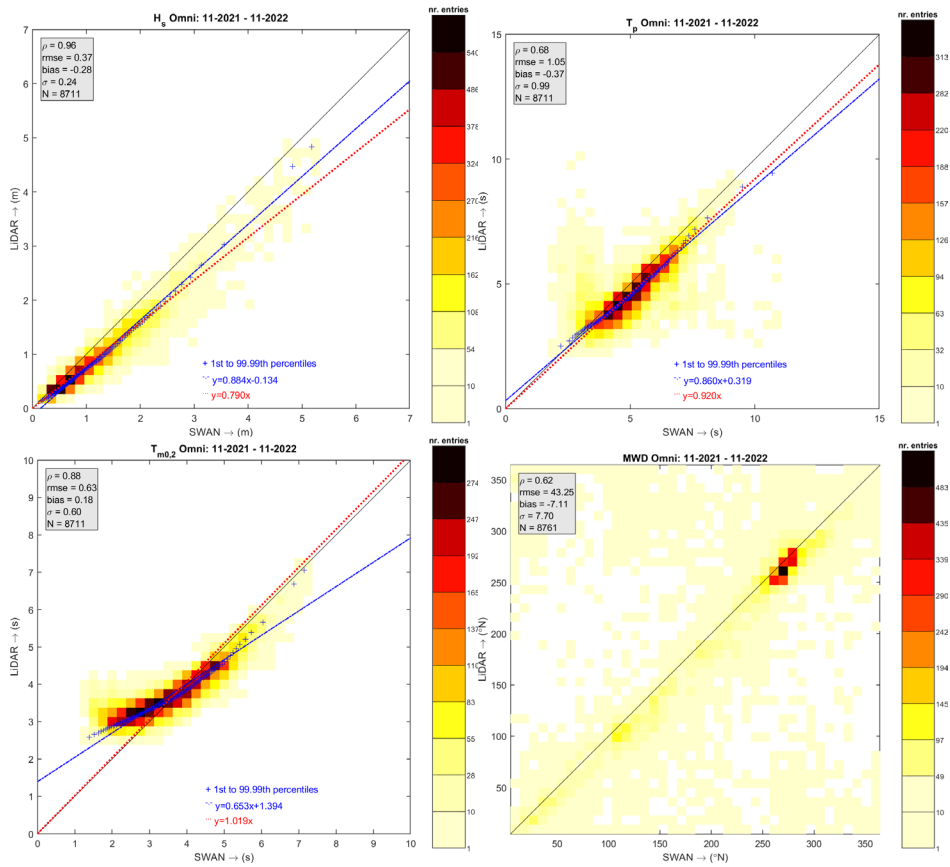


Figure 3-72 Density scatter comparisons (all data) between the buoy observations and the (raw) SWAN results at BHI-1-LB. Top left: significant wave height, top right: peak wave period, bottom left: zero-crossing wave period, bottom right: mean wave direction.

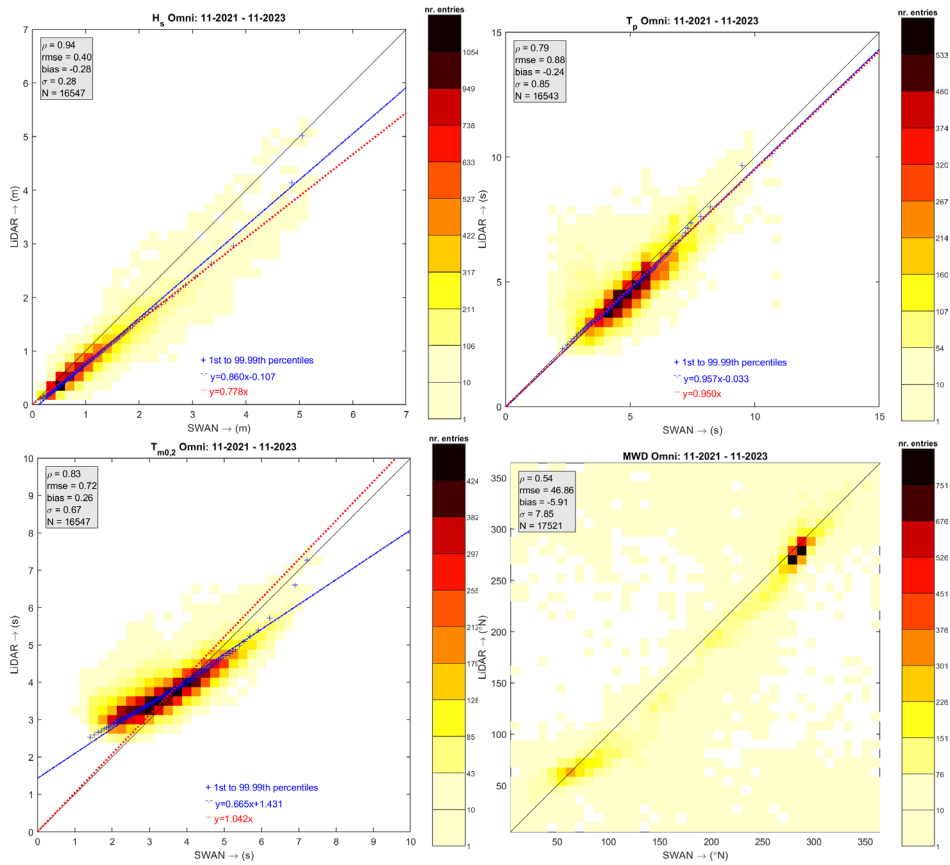


Figure 3-73 Density scatter comparisons (all data) between the buoy observations and the (raw) SWAN results at BHII-1-LB. Top left: significant wave height, top right: peak wave period, bottom left: zero-crossing wave period, bottom right: mean wave direction.

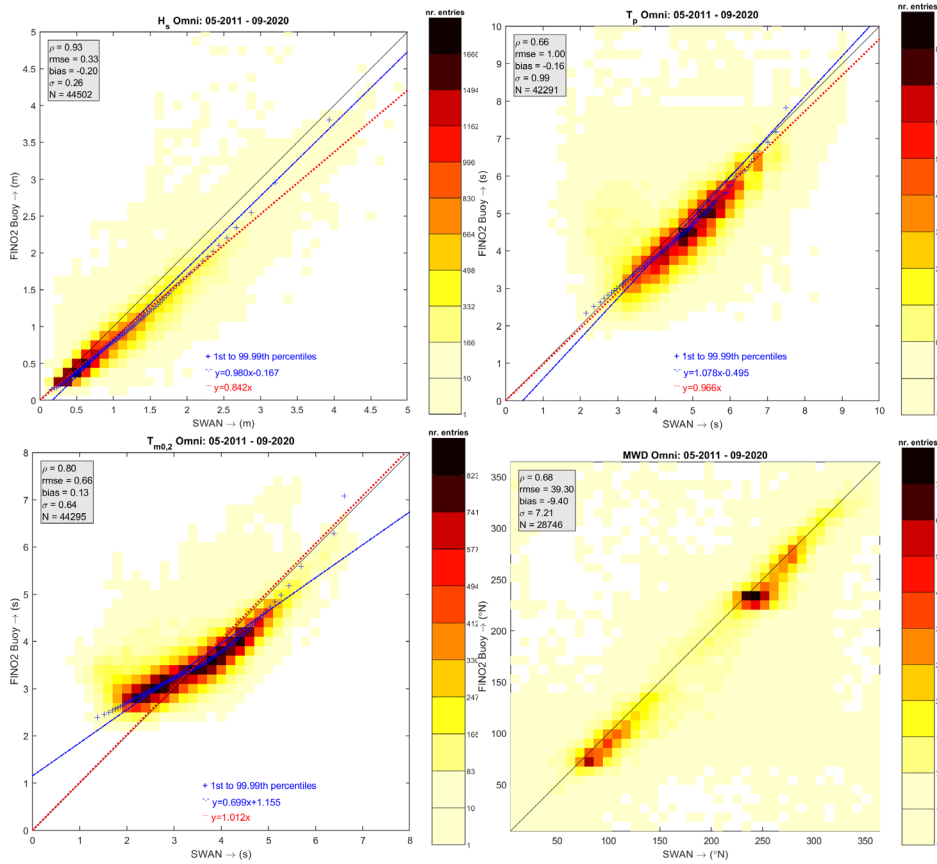


Figure 3-74 Density scatter comparisons (all data) between the buoy observations and the (raw) SWAN results at FINO2 (buoy). Top left: significant wave height, top right: peak wave period, bottom left: zero-crossing wave period, bottom right: mean wave direction.

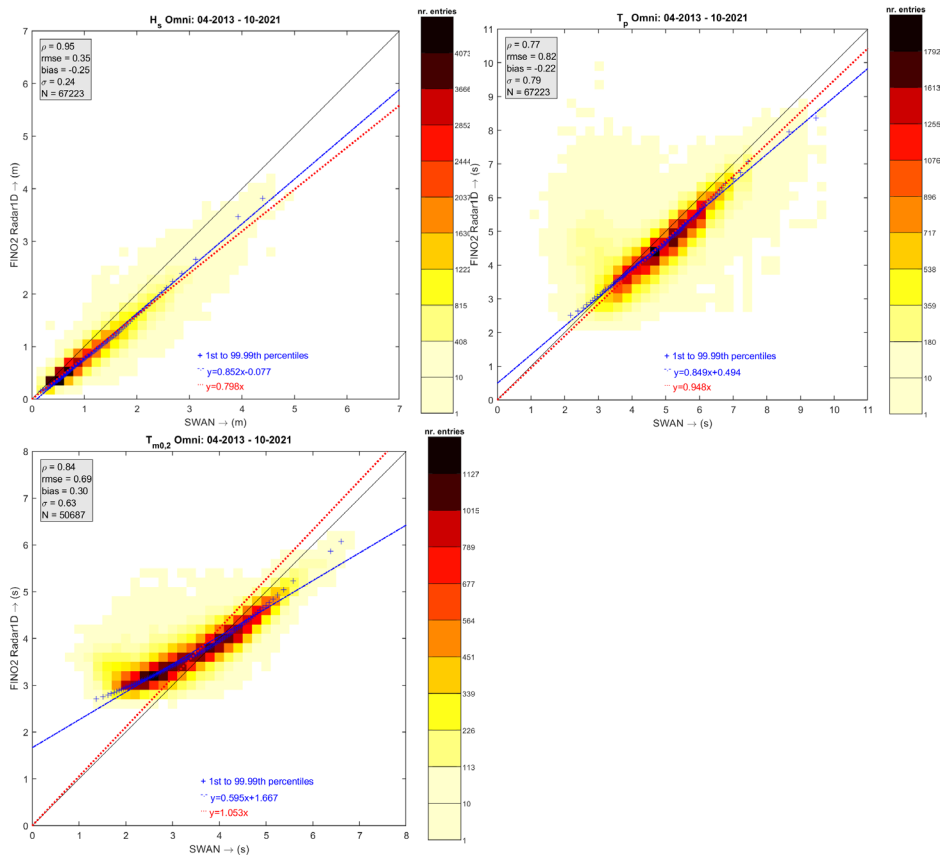


Figure 3-75 Density scatter comparisons (all data) between the buoy observations and the (raw) SWAN results at FINO2 (wave radar). Top left: significant wave height, top right: peak wave period, bottom left: zero-crossing wave period.

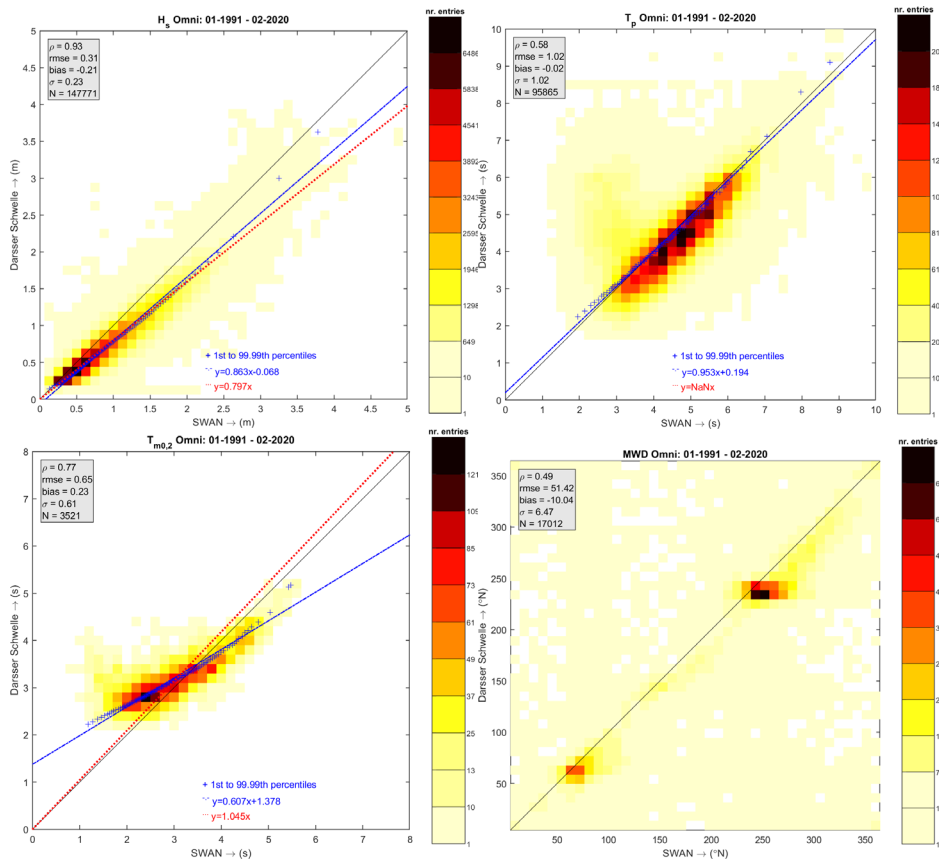


Figure 3-76 Density scatter comparisons (all data) between the buoy observations and the (raw) SWAN results at Darsser-Schwelle. Top left: significant wave height, top right: peak wave period, bottom left: zero-crossing wave period, bottom right: mean wave direction.

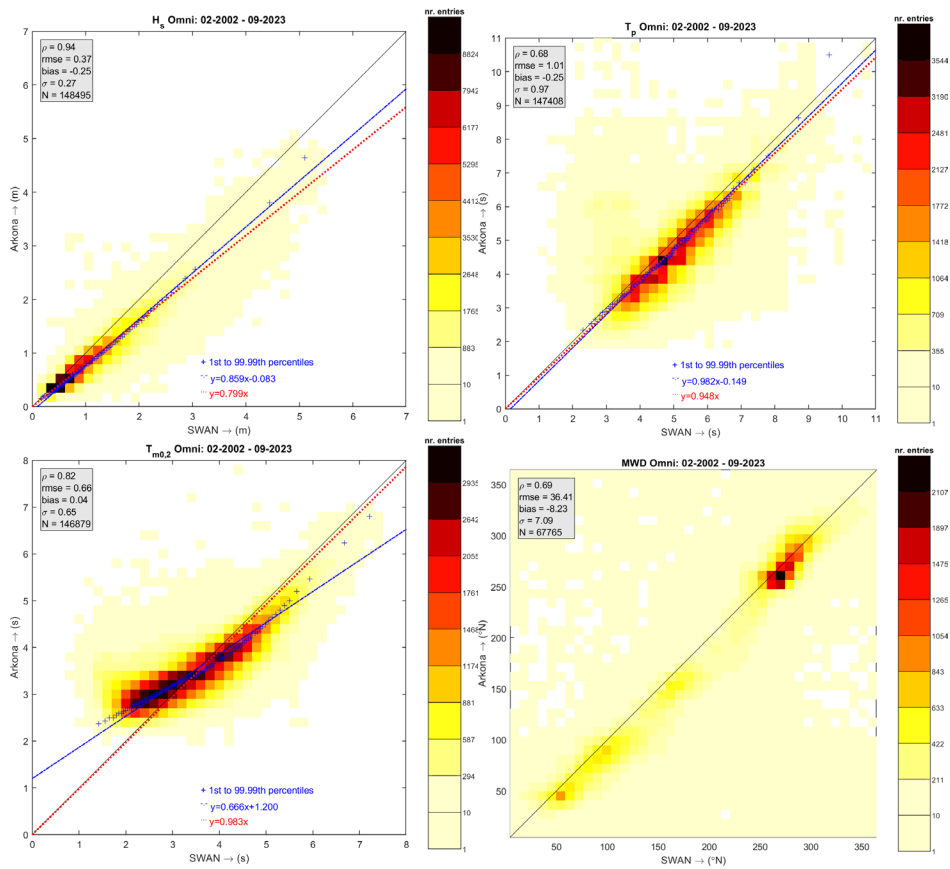


Figure 3-77 Density scatter comparisons (all data) between the buoy observations and the (raw) SWAN results at Arkona. Top left: significant wave height, top right: peak wave period, bottom left: zero-crossing wave period, bottom right: mean wave direction.

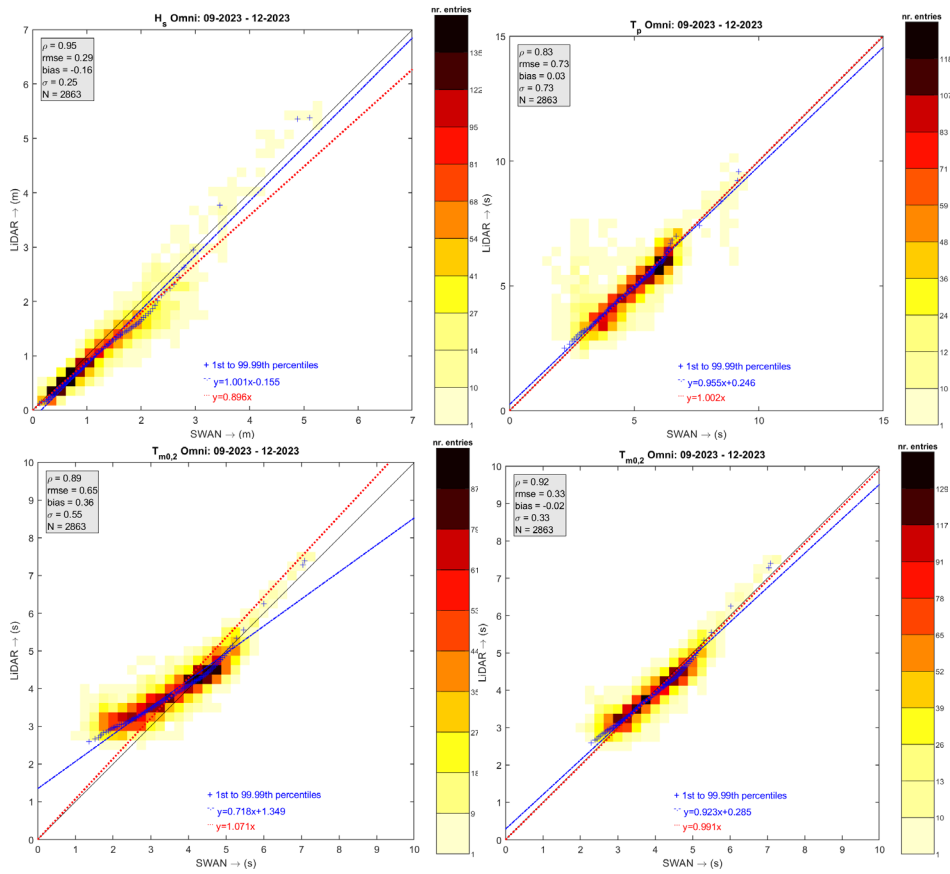


Figure 3-78 Density scatter comparisons (all data) between the buoy observations and the corrected SWAN results at KFII-1-LB (Kriegers Flak II South OWF). Top left: significant wave height, top right: peak wave period, bottom left: zero-crossing wave period (full frequency range, 0.03-1.0 Hz), bottom right: zero-crossing wave period (limited frequency range, 0.04-0.5 Hz).

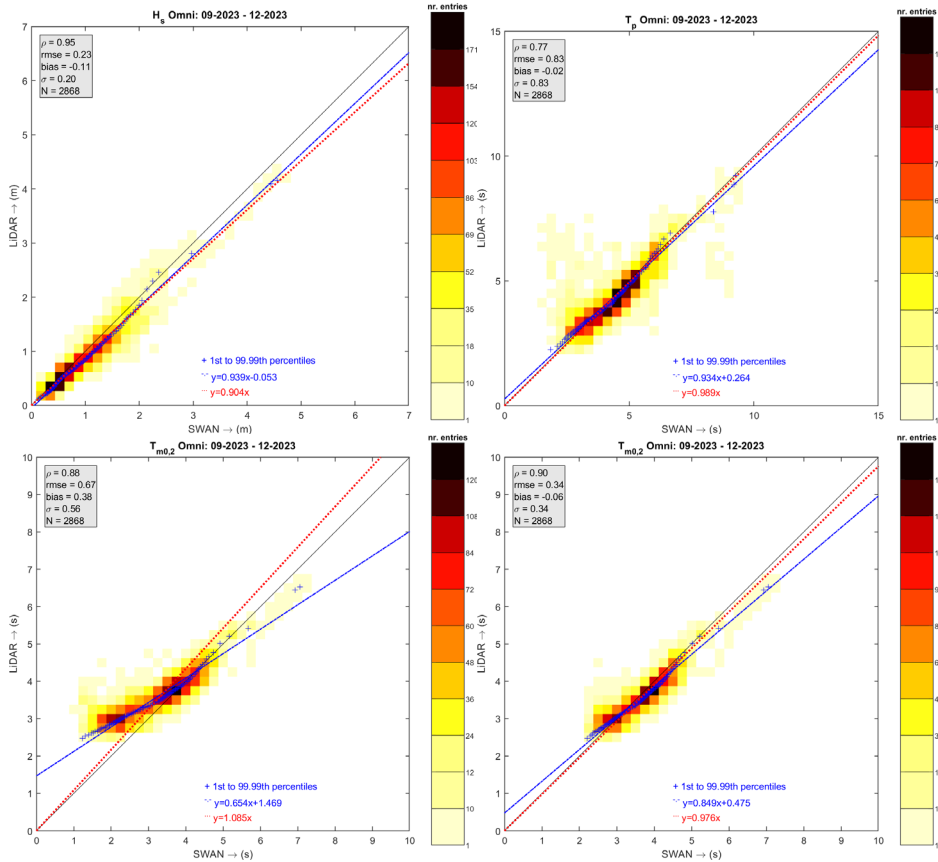


Figure 3-79 Density scatter comparisons (all data) between the buoy observations and the corrected SWAN results at KFI-2-LB (Kriegers Flak II North OWF). Top left: significant wave height, top right: peak wave period, bottom left: zero-crossing wave period (full frequency range, 0.03-1.0 Hz), bottom right: zero-crossing wave period (limited frequency range, 0.04-0.5 Hz).

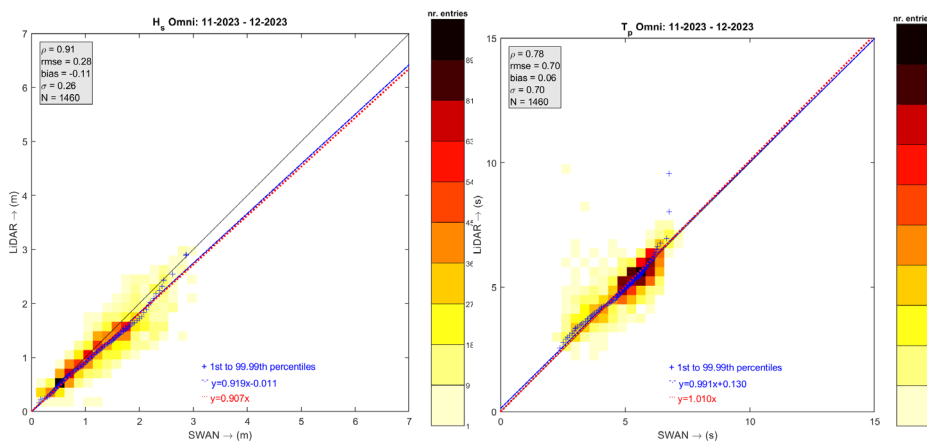


Figure 3-80 Density scatter comparisons (all data) between the buoy observations and the corrected SWAN results at KFI-3-LB (Kriegers Flak II North OWF). Left: significant wave height, right: peak wave period.

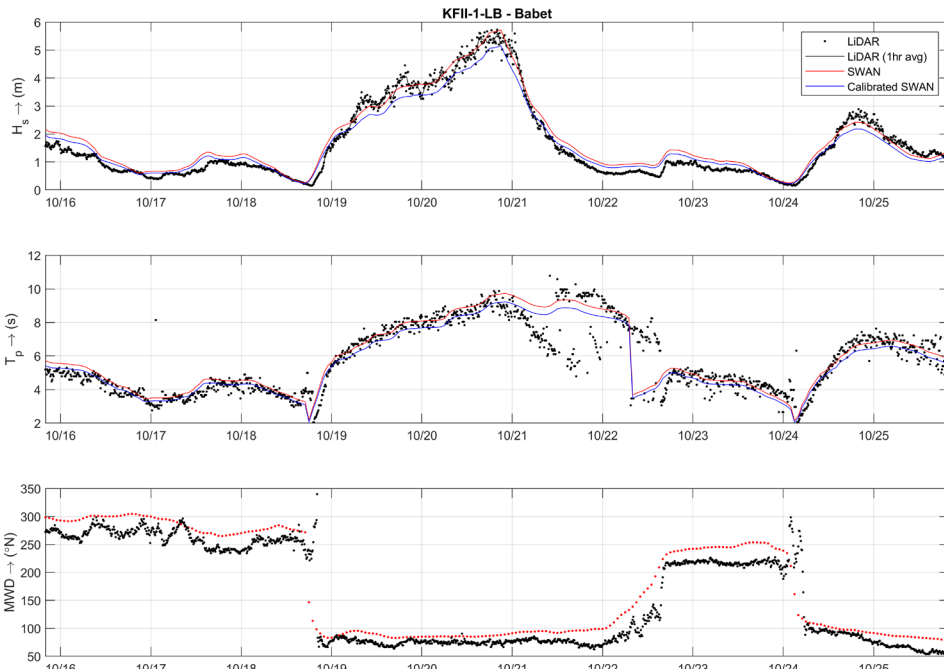


Figure 3-81 Timeseries of the observations and the raw and calibrated SWAN output at KFII-1-LB during the Storm Babet (Oct. 2023).

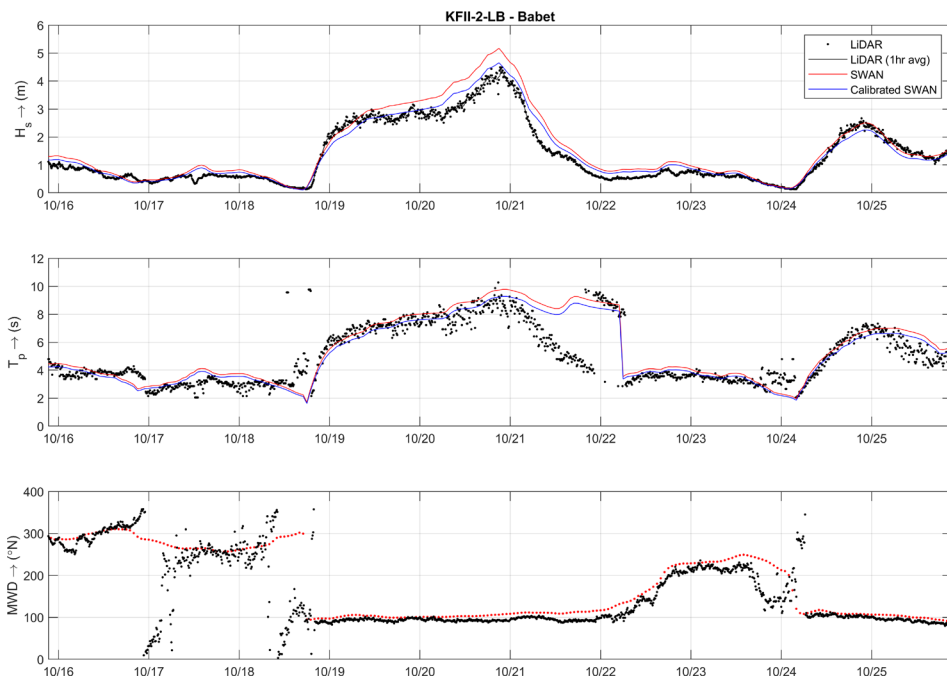


Figure 3-82 Timeseries of the observations and the raw and calibrated SWAN output at KFII-2-LB during the Storm Babet (Oct. 2023).

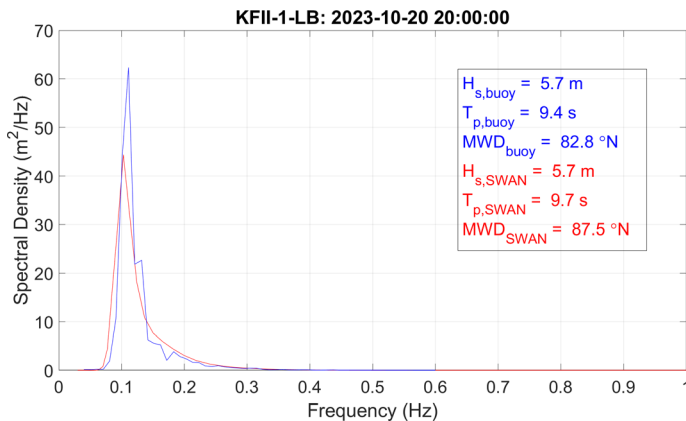


Figure 3-83 Comparison of raw wave spectral data at location KFII-1-LB during the peak of storm Babet (20 October 2023).

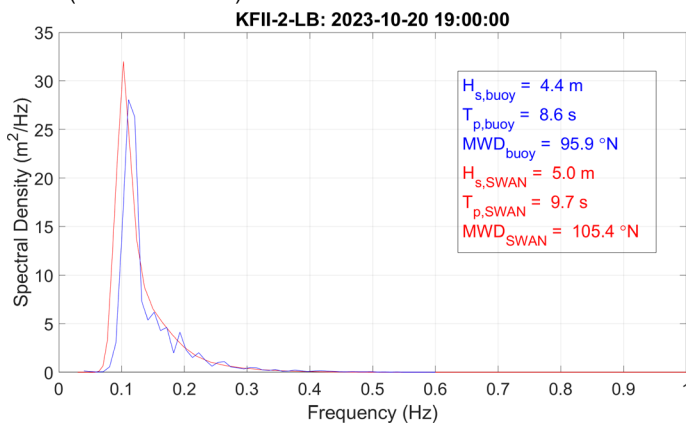


Figure 3-84 Comparison of raw wave spectral data at location KFII-2-LB during the peak of storm Babet (20 October 2023).

3.4.3 The Kriegers Flak II North and South (KFII) OWF wave dataset

Based on the validation and calibration of the SWAN wave data in the KFII OWF area presented in Section 3.4.2, the wave timeseries were derived. The resulting wave timeseries are considered to accurately describe the various wave parameters within the area of the KFII OWFs. These timeseries are provided together with this report as NetCDF files (together with the wind data) at both the reference locations (cf. Table 2-1, including hub-height wind data) and at the output locations within the data delivery area (excluding hub-height wind data) and cover the period from 1979 to 2023 (45 years, 01-01-1979 00:00 – 31-12-2023 23:00) at an hourly interval. At the reference locations, also two-dimensional wave spectra files are delivered for the same period.

The naming of the three types of files follows the following structure:

- **Reference locations (6 in total):**
KriegersFlakIIArea_Point
name_latitudeN_longitudeE_WavesWind_1979_2023.nc
KriegersFlakIIArea_Point
name_latitudeN_longitudeE_WaveSpectra_1979_2023.nc

- **Data delivery area locations (9,318 in total):**
KriegersFlakIIArea_latitudeN_longitudeE_WavesWind_1979_2023.nc

The reference point timeseries are used in Part B (SWECO, 2024) of the study as input for the determination of the normal and extreme wave conditions.

Please note that within the data delivery area data points along the coastline with depths less than 5 m have been excluded as the wave model has not been optimized for such shallow locations.

3.5 Climate change effects

In order to obtain estimates of the effects of climate change during the service life of the wind farm (about 25 years after 2030), we resort to the data from the *Intergovernmental Panel on Climate Change* (IPCC¹⁶) and related publications. In IPCC's newest Assessment Report (AR6) different levels of greenhouse gas emissions and other radiative forcings that might occur in the future and the impact of socioeconomic factors that may change over the next century, such as population, economic growth, education, urbanisation and the rate of technological development are considered in Shared Socioeconomic Pathways (SSPs¹⁷). The SSPs describe a total of nine different possible 21st century pathways of GHG emissions and atmospheric concentrations, air pollutant emissions and land use. They comprise a stringent mitigation scenario (SSP1-2.6), two intermediate scenarios (SSP2-4.5 and SSP3-7.0) and one scenario with high GHG emissions (SSP5-8.5). Scenarios without additional efforts to constrain emissions ('baseline scenarios' or 'business-as-usual scenarios') lead to pathways ranging between SSP3-7.0 and SSP5-8.5. SSP1-2.6 is representative of a scenario that aims to keep global warming likely below 2°C above pre-industrial temperatures.

The AR projections of global mean sea level rise until 2150 (relative to 2000) for five SSP scenarios are presented in Figure 3-85 (IPCC, 2021). The figure shows a projected global mean sea level rise ranging between 0.3 m and 1.0 m by 2100. Sea level rise is, however, not globally uniform and varies regionally. The projections of sea level rise at the Kriegers Flak region were extracted from the *Sea Level projection Tool*¹⁸ developed by NASA (Fox-Kemper et al. 2021, Kopp et al. 2023 and Garner et al. 2021). These are given in Figure 3-86 for the stringent mitigation scenario SSP1-2.6, intermediate scenarios SSP2-4.5 and SSP3-7.0 and the high scenario SSP5-8.5. The figure shows that in the area even for the most pessimist scenario the SLR is projected to be lower than 30 cm by 2055, which is also in line with the projections given in the DMI climate atlas¹⁹. Namely, of a SLR median value of 0.28 cm for scenario SSP5-8.5 in the period 2041-2070.

¹⁶ <https://www.ipcc.ch/>

¹⁷ The illustrative scenarios are referred to as SSPx-y, where 'SSPx' refers to the Shared Socio-economic Pathway or 'SSP' describing the socio-economic trends underlying the scenario, and 'y' refers to the approximate level of radiative forcing (in W m⁻²) in 2100.

¹⁸ <https://sealevel.nasa.gov/ipcc-ar6-sea-level-projection-tool>

¹⁹ <https://www.dmi.dk/klima-atlas/data-i-klimateatlas?maptype=kyst¶mtype=sea>

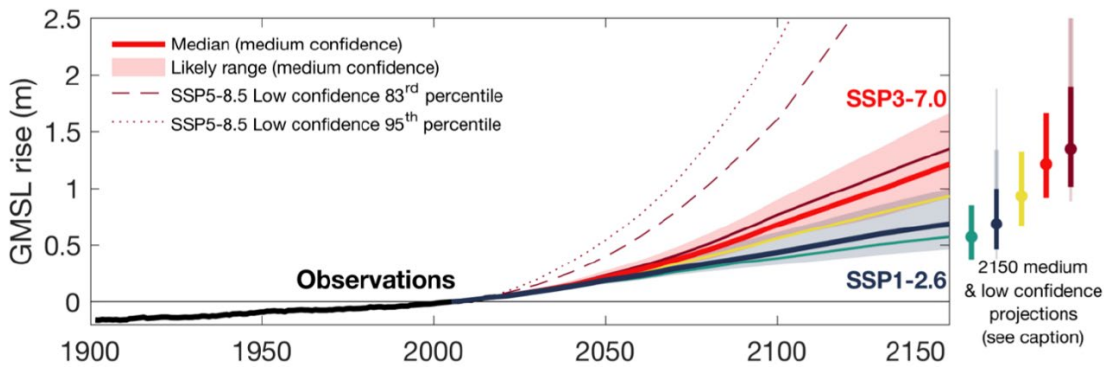


Figure 3-85 Global mean sea level change from 1900 to 2150, observed (1900–2018) and projected under the SSP scenarios (2000–2150), relative to a 1995–2014 baseline. Solid lines show median projections. Shaded regions show likely ranges for SSP1-2.6 and SSP3-7.0. Dotted and dashed lines show respectively the 83rd and 95th percentile low-confidence projections for SSP5-8.5. Bars on the right show, left to right, likely ranges for SSP1-1.9, SSP1-2.6, SSP2-4.5, SSP3-7.0, and SSP5-8.5 in 2150. Lightly shaded thick/thin bars show 17th–83rd/5th–95th percentile low-confidence ranges in 2150 for SSP1-2.6 and SSP5-8.5. Low-confidence range for SSP5-8.5 in 2150 extends to 4.8/5.4 m at the 83rd/95th percentile. (from: IPCC, 2021, Box TS.4, Figure 1a).

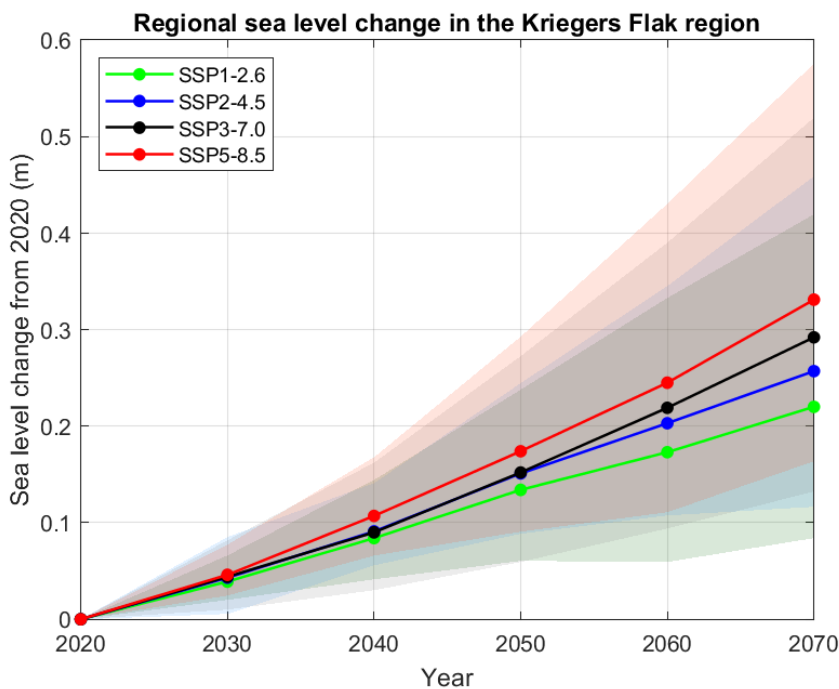


Figure 3-86 Sea level change (in m) relative to 2020 for the Kriegers Flak region for SSP1-2.6, SSP2- 4.5, SSP3- 7.0 and SSP5- 8.5 according to IPCC (2021). The full lines indicate the 50th percentiles and the shadows the 5th to 95th percentile range.

No SLR allowance has been included in the hydrodynamic or wave modelling. Given the relatively low SLR values with relation to the local OWF depths and the uncertainties associated with the given metocean estimates, such an allowance would not lead to significant differences in the model results. Furthermore, Meier et al. (2022) carried out an in-depth review and study of climate change effects in the Baltic Sea region. In terms of wind climate they

refer to a study indicating decreased wind speed in the southern Baltic, but conclude that given the large uncertainties in the projections and the large natural variability, that the Baltic wind speed and directions are not likely to significantly change in the future. With relation to the wave climate, they also report no likelihood of significant changes due to changes in wind. The projected reduction in the seasonal sea ice coverage in the northern Baltic Sea is considered reliable, but also not expected to significantly affect the wave conditions in the Southern Baltic Sea.

With relation to the water properties, climate model projections show a tendency towards future reduced salinity, but due to the large bias in the water balance projections, it is still uncertain whether the Baltic Sea will become less or more saline (Meier et al., 2022). Furthermore, climate model projections show an increase in annual mean sea surface temperature of between 1.1 and 3.2°C, averaged for the Baltic Sea at the end of the century, with the warming being largest in summer in the northern Baltic Sea (Meier et al., 2022).

3.6 Selection of reference locations

Based on the severity and variability of the current and wave conditions in the area, a total of 3 reference locations per OWF have been chosen.

Figure 3-87 to Figure 3-89 show the spatial fields with the 95th percentile values of the significant wave height (H_s), wave load proxy ($H_s \cdot \sqrt{T_p}$) and depth-averaged current speeds (CS) for Kriegers Flak II North respectively. Figure 3-91 to Figure 3-93 do the same for Kriegers Flak II South. In order to make the figures readable, the results are only plotted for a subset of all grid points within the OWF areas. To do so, a secondary grid was defined with a resolution of 0.01° in longitudinal direction and a resolution of 0.005° in latitudinal direction. For this secondary grid, the nearest grid points were determined, which are shown in the figures.

In terms of spatial variations, the gradients are relatively low for all variables. Based on these figures, the reference locations have been defined jointly with the Client, considering the most severe conditions and aiming at a reasonable spatial coverage of the OWF areas. The resulting locations (name, coordinates and depth) are listed Table 3-12 (see Figure 3-90) and Table 3-13 (see Figure 3-94) for Kriegers Flak II North and South respectively.

3.6.1 Kriegers Flak II North

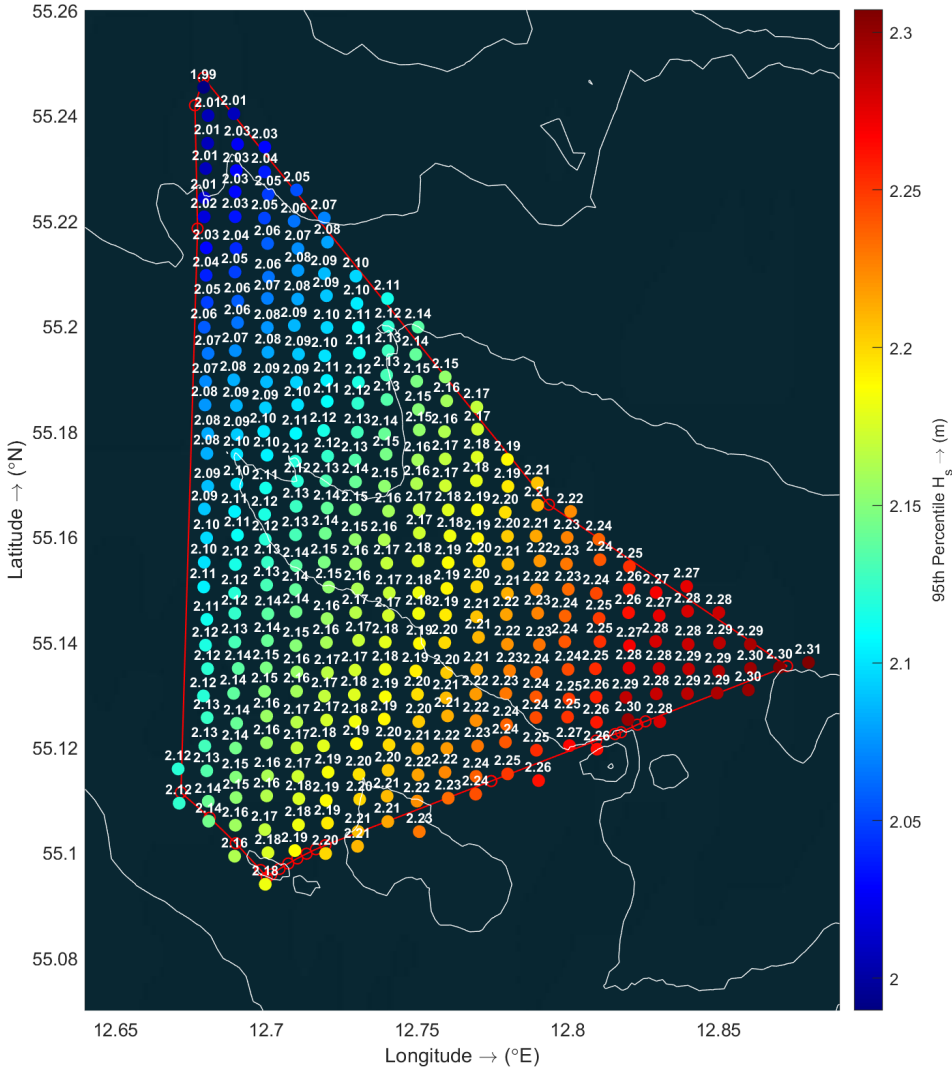


Figure 3-87 95th Percentile of the significant wave height, H_s , of the hourly data from 1979 until 2023 for Kriegers Flak II North OWF.

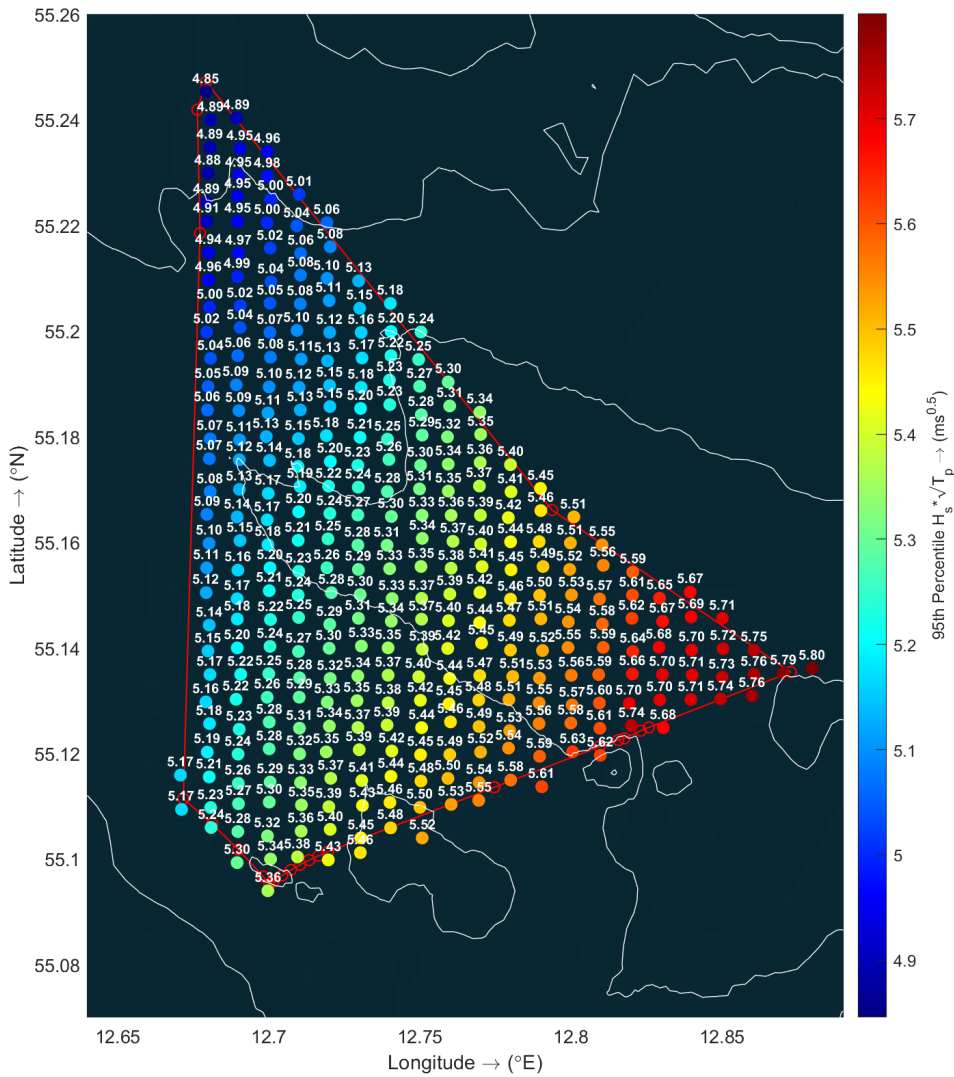


Figure 3-88 95th Percentile of the wave load proxy, $H_s^* \sqrt{T_p}$, of the hourly data from 1979 until 2023 for Kriegers Flak II North OWF.

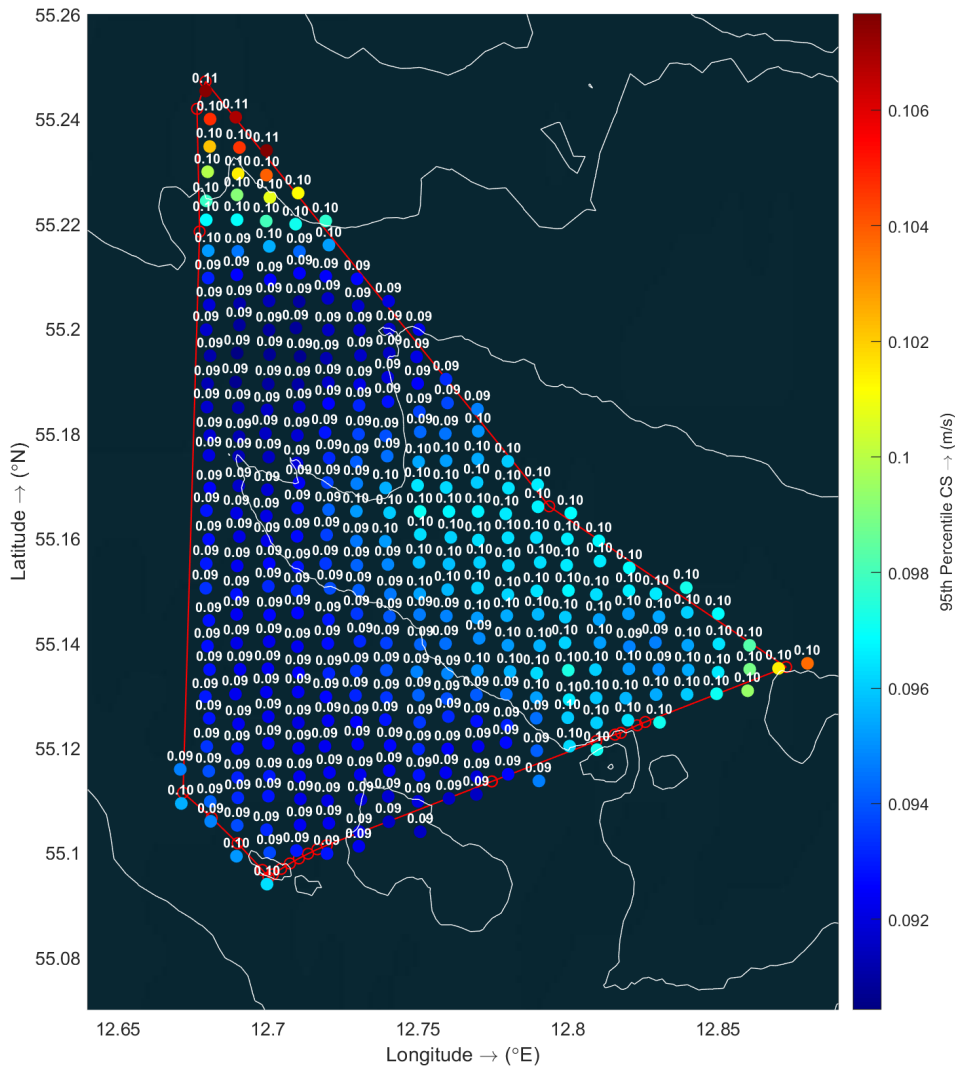


Figure 3-89 95th Percentile of the depth-averaged current speed, CS, of the hourly data from 1979 until 2023 for Kriegers Flak II North OWF.

Table 3-12 Overview of selected reference locations Kriegers Flak II North OWF.

Location-ID	Longitude (°E)	Latitude (°N)	Depth (mMSL)
KFII-N-1	12.8199	55.1252	-32.02
KFII-N-2	12.6905	55.2345	-23.69
KFII-N-3	12.6997	55.0940	-29.66

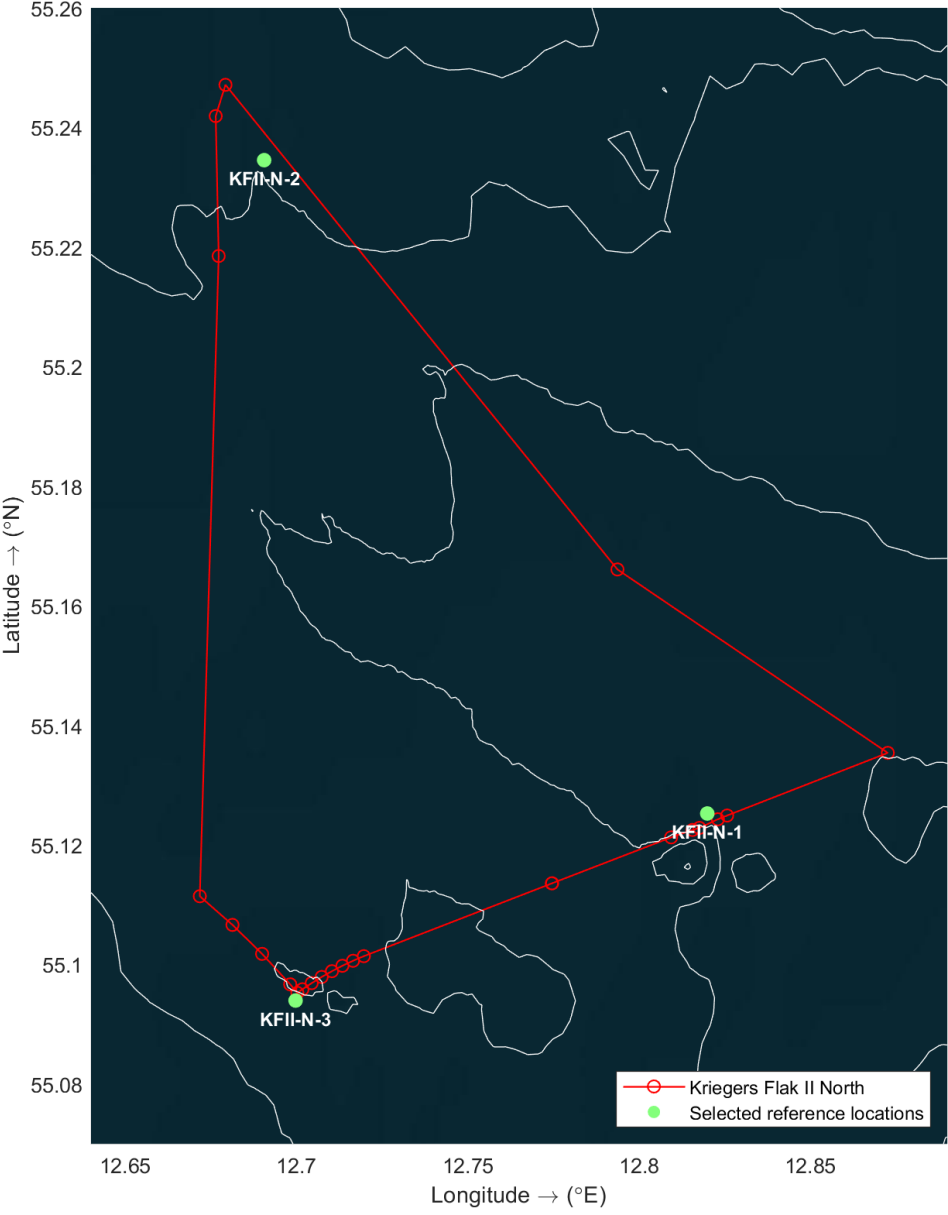


Figure 3-90 Selected reference locations Kriegers Flak II North OWF.

3.6.2 Kriegers Flak II South

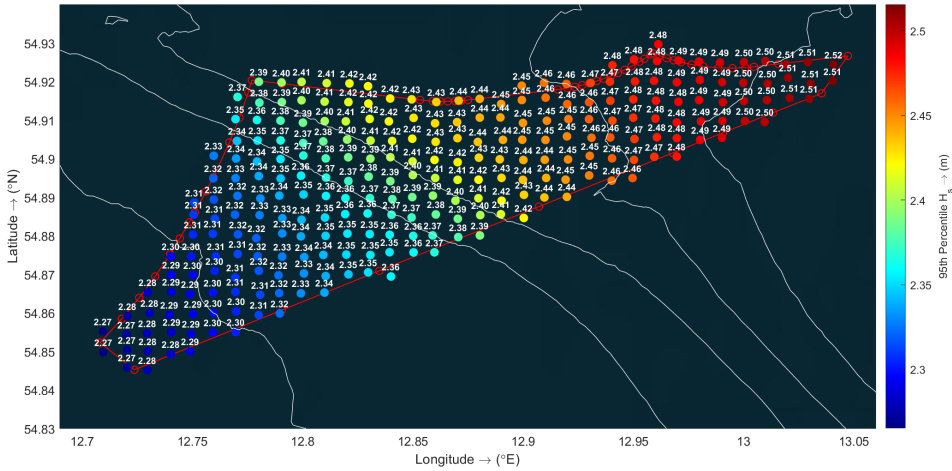


Figure 3-91 95th Percentile of the significant wave height, H_s , of the hourly data from 1979 until 2023 for Kriegers Flak II South OWF.

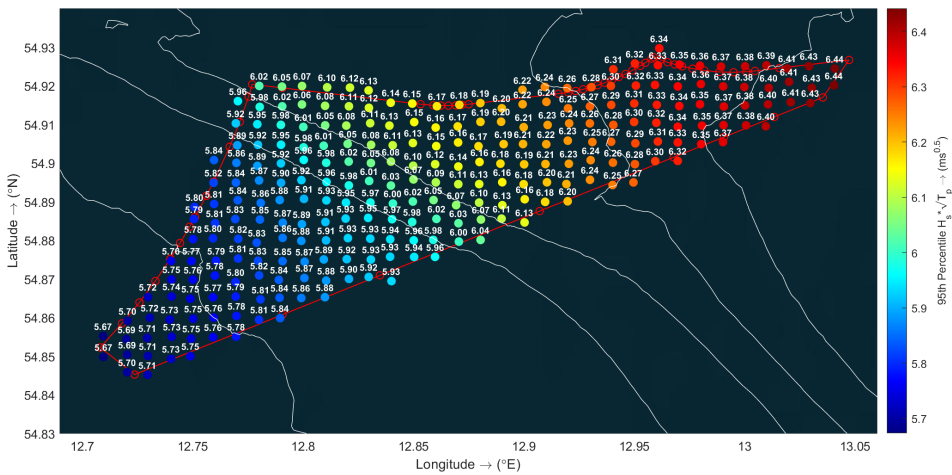


Figure 3-92 95th Percentile of the wave load proxy, $H_s^3 \sqrt{T_p}$, of the hourly data from 1979 until 2023 for Kriegers Flak II South OWF.

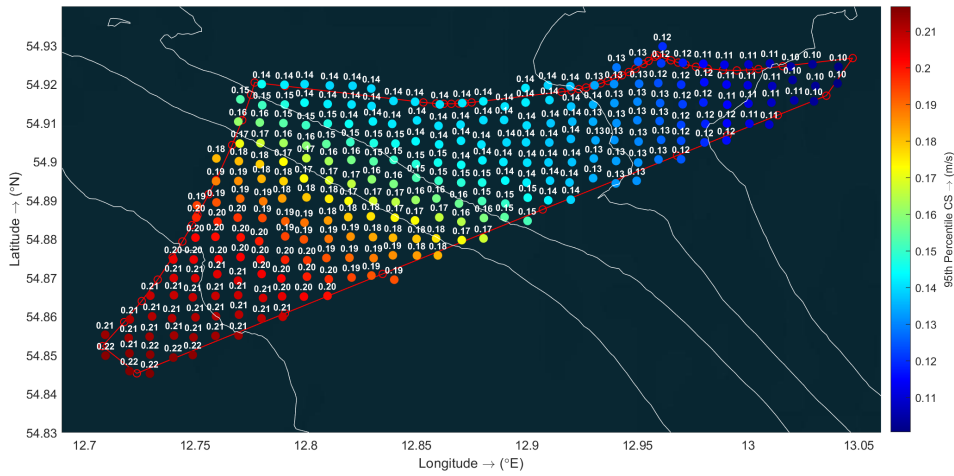


Figure 3-93 95th Percentile of the depth-averaged current speed, CS, of the hourly data from 1979 until 2023 for Kriegers Flak II South OWF.

Table 3-13 Overview of selected reference locations Kriegers Flak II South OWF.

Location-ID	Longitude (°E)	Latitude (°N)	Depth (mMSL)
KFII-S-1	12.9998	54.9197	-39.71
KFII-S-2	12.7802	54.9200	-31.40
KFII-S-3	12.7096	54.8498	-18.43

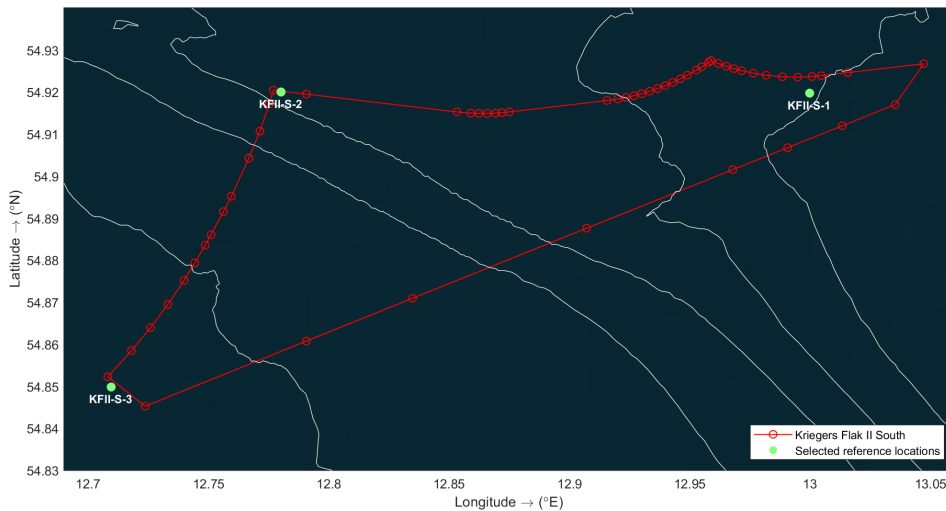


Figure 3-94 Selected reference locations Kriegers Flak II South OWF.

4 References

- Battjes, J. A., and J. P. F. M. Janssen, 1978: Energy loss and set-up due to breaking of random waves, *Coastal Engineering 1978* (pp. 569–588), Am. Soc. of Civ. Eng., New York.
- Caires, S., H. de Waal, G. Groen, N. Wever, C. Geerse, and M. Bottema, 2012: Assessing the uncertainties of using land-based wind observations for determining extreme open-water winds. *J. Wind Eng. Ind. Aerodyn.*, 110, 70–85.
- CMEMS, 2021a, GLOBAL_ANALYSIS_FORECAST_PHY_001_024, <https://doi.org/10.48670/moi-00016>.
- CMEMS, 2021b, BALTICSEA_REANALYSIS_PHY_003_011, <https://doi.org/10.48670/moi-00013>.
- Deltares, 2022: Independent review of the Hydrodynamic Studies on the impact of Lynetteholm on exchange of water and salt through Øresund, Deltares report 11207757-002-HYE-0001.
- Fox-Kemper, B., H. T. Hewitt, C. Xiao, G. Aðalgeirsdóttir, S. S. Drijfhout, T. L. Edwards, N. R. Golledge, M. Hemer, R. E. Kopp, G. Krinner, A. Mix, D. Notz, S. Nowicki, I. S. Nurhati, L. Ruiz, J-B. Sallée, A. B. A. Slangen, Y. Yu, 2021: Ocean, Cryosphere and Sea Level Change. In: *Climate Change 2021: The Physical Science Basis. Contribution of Working Group I to the Sixth Assessment Report of the Intergovernmental Panel on Climate Change* [Masson-Delmotte, V., P. Zhai, A. Pirani, S. L. Connors, C. Péan, S. Berger, N. Caud, Y. Chen, L. Goldfarb, M. I. Gomis, M. Huang, K. Leitzell, E. Lonnoy, J. B. R. Matthews, T. K. Maycock, T. Waterfield, O. Yelekçi, R. Yu and B. Zhou (eds.)]. Cambridge University Press.
- Fugro, 2023a: SWLB measurements - Danish Offshore Wind 2030 - Project Measurement Plan, All Lots, C75516/C75517/C75518.
- Fugro, 2023b: SWLB measurements at Energy Islands - Project Measurement Plan, All Lots, C75486.

- Garner, G. G., T. Hermans, R. E. Kopp, A. B. A. Slangen, T. L. Edwards, A. Levermann, S. Nowicki, M. D. Palmer, C. Smith, B. Fox-Kemper, H. T. Hewitt, C. Xiao, G. Aðalgeirsdóttir, S. S. Drijfhout, T. L. Edwards, N. R. Golledge, M. Hemer, R. E. Kopp, G. Krinner, A. Mix, D. Notz, S. Nowicki, I. S. Nurhati, L. Ruiz, J-B. Sallée, Y. Yu, L. Hua, T. Palmer, B. Pearson, 2021. IPCC AR6 Sea-Level Rise Projections. Version 20210809. PO.DAAC, CA, USA. Dataset accessed 2024-03-27 at <https://sealevel.nasa.gov/>.
- GEOxyz, 2024: Geophysical and Geological Survey Report For Kriegers Flak II North and South, Report BE5376H-711-03-RR, Version 2, 02/02/2024.
- Goda, Y., 1978. The observed joint distribution of periods and heights of sea waves. In Proc. 16th Int. Conf.on Coastal Engineering, Hamburg. ASCE, New York, pp. 227-246.
- Hasselmann K., T.P. Barnett, E. Bouws, H. Carlson, D.E. Cartwright, K. Enke, J.A. Ewing, H. Gienapp, D.E. Hasselmann, P. Kruseman, A. Meerburg, P. Mller, D.J. Olbers, K. Richter, W. Sell, and H. Walden, 1973: Measurements of wind-wave growth and swell decay during the Joint North Sea Wave Project (JONSWAP). *Ergzungsheft zur Deutschen Hydrographischen Zeitschrift Reihe, A(8), Nr. 12*, p.95. Komen, G.J., S. Hasselmann, and K. Hasselmann, 1984: On the existence of a fully developed windsea spectrum, *J. Phys. Oceanogr.*, 14, 1271-1285.
- Karmpadakis, I., C. Swan and M. Christou, 2022: A new wave height distribution for intermediate and shallow water depths, *Coastal Engineering*, 175, <https://doi.org/10.1016/j.coastaleng.2022.104130>.
- Kernkamp, H.W.J.; van Dam, A.; Stelling, G.S. & de Goede, E.D., 2011: Efficient scheme for the shallow water equations on un-structured grids with application to the Continental Shelf. *Ocean Dynamics*, 61, 1175–1188, doi: 10.1007/s10236-011-0423-6.
- Meier, H. E. M., Kniebusch, M., Dieterich, C., Gröger, M., Zorita, E., Elmgren, R., Myrberg, K., Ahola, M. P., Bartosova, A., Bonsdorff, E., Börgel, F., Capell, R., Carlén, I., Carlund, T., Carstensen, J., Christensen, O. B., Dierschke, V., Frauen, C., Frederiksen, M., Gaget, E., Galatius, A., Haapala, J. J., Halkka, A., Hugelius, G., Hünicke, B., Jaagus, J., Jüssi, M., Käyhkö, J., Kirchner, N., Kjellström, E., Kulinski, K., Lehmann, A., Lindström, G., May, W., Miller, P. A., Mohrholz, V., Müller-Karulis, B., Pavón-Jordán, D., Quante, M., Reckermann, M., Rutgersson, A., Savchuk, O. P., Stendel, M., Tuomi, L., Viitasalo, M., Weisse, R., and Zhang, W., 2022: Climate change in the Baltic Sea region: a summary, *Earth Syst. Dynam.*, 13, 457–593, <https://doi.org/10.5194/esd-13-457-2022>, 2022.
- Pawlowicz, R., B. Beardsley and S. Lentz, 2002: Classical tidal harmonic analysis including error estimates in MATLAB using T TIDE. *Computers & Geosciences*, 28 (8): 929 - 937. DOI: [https://doi.org/10.1016/S0098-3004\(02\)00013-4](https://doi.org/10.1016/S0098-3004(02)00013-4), ISSN 0098-3004.
- Ramboll, 2013a: Kriegers Flak Cable Route Geophysical Survey Results, 04/09/2013.
- Ramboll, 2013b: Kriegers Flak OWF Geophysical Survey Results, 22/08/2013.

- Rienecker, M.M. and J.D. Fenton, 1981: A Fourier approximation method for steady water waves. *J. Fluid Mechanics*, 104, 119–137.
- Rogers, W.E., P.A. Hwang, and D.W. Wang. 2003: Investigation of wave growth and decay in the SWAN model: three regional-scale applications, *J. Phys. Oceanogr.*, 33, 366-389.
- SWECO, 2024: Kriegers Flak II – North and South Site Metocean Conditions Assessments: Part B: Analyses and Design Parameters (41011328B_KG_PartB_Analyses_and_Design_Parameters.docx).
- Wu, J., 1982: Wind-stress coefficients over sea surface from breeze to hurricane, *J. Geophys. Res.*, 87 (C12), 9704-9706.
- Zijlema, M., 2010: Computation of wind-wave spectra in coastal waters with SWAN on unstructured grids. *Coastal Engineering*, **57**, 267-277.
- Zijlema, M., G.Ph. van Vledder and L.H. Holthuijsen, 2012: Bottom friction and wind drag for wave models. *Coastal Engineering*, 65, 19-26.

Appendix A Error statistics

Introduction

A particularity of certain environmental data (e.g. wave data) is that they can be classified into *linear data* (e.g. mean wave period and significant wave height) and *circular data* (e.g. mean wave direction and directional spread), and this distinction must be taken into consideration when carrying out error analysis (Van Os and Caires, 2011). The statistical techniques for dealing with these two types of data are different – circular (or directional) data require a special approach. Basic concepts of statistical analysis of circular data are given in the books of Mardia (1972) and Fisher (1993).

Linear variables

Differences between linear variables are often quantified using the following standard statistics:

- the bias: $\bar{y} - \bar{x}$;
- the root-mean-square error: $RMSE = \sqrt{n^{-1} \sum (y_i - x_i)^2}$;
- the scatter index: $SI = \frac{\sqrt{n^{-1} \sum [(y_i - \bar{y}) - (x_i - \bar{x})]^2}}{\bar{x}}$;
- the correlation coefficient: $\rho = \frac{\sum [(x_i - \bar{x}) - (y_i - \bar{y})]}{\sqrt{\sum (x_i - \bar{x})^2 \sum (y_i - \bar{y})^2}}$;
- the symmetric slope: $r = \sqrt{\sum x_i^2 / \sum y_i^2}$.

In all these formulae x_i usually represents observations (or the dataset which is considered less uncertain or baseline), y_i represents the model results (or the dataset which is considered more uncertain or with a certain deviation from the baseline results) and n the number of observations. In this study, when trying to derive calibration expressions, x_i corresponds to the model results.

Circular variables

If we compute an average of angles as their arithmetic mean, we may find that the result is of little use as a statistical location measure. Consider for instance the case of two angles of 359° and 1°; their arithmetic mean is 180°, when in reality 359° is only two degrees away from 1° and the mid direction between the two is 0°. This phenomenon is typical for circular data and illustrates the need for special definitions of statistical measures in general.

When dealing with circular data, each observation is considered as unit vector, and it requires vector addition rather than ordinary (or scalar) addition to compute the average of angles, the so-called mean direction.

Writing

$$C_n = \sum_{i=1}^n \cos x_i \quad \text{and} \quad S_n = \sum_{i=1}^n \sin x_i, \quad (\text{A.1})$$

the *sample resultant vector* R_n of a sample $x = \{x_i, i = 1, \dots, n\}$ is defined as

$$R_n = \sqrt{C_n^2 + S_n^2},$$

and its *sample mean direction* $\bar{x} \equiv \bar{x}_n$ as the direction of R_n :

$$\bar{x} = \text{TAN}^{-1}(S_n/C_n) \quad (\text{A.2})$$

where $\text{TAN}^{-1}(S_n/C_n)$ is the inverse of the tangent of (S_n/C_n) in the range $[0, 2\pi [$, i.e.,

$$\text{TAN}^{-1}\left(\frac{S_n}{C_n}\right) = \begin{cases} \tan^{-1}\left(\frac{S_n}{C_n}\right), & S_n > 0, C_n > 0 \\ \tan^{-1}\left(\frac{S_n}{C_n}\right) + \pi, & C_n < 0 \\ \tan^{-1}\left(\frac{S_n}{C_n}\right) + 2\pi, & S_n < 0, C_n > 0. \end{cases}$$

The *sample mean resultant length* of $x = \{x_i, i = 1, \dots, n\}$ is defined by

$$\bar{R}_n = R_n/n, 0 < \bar{R}_n < 1$$

If $\bar{R}_n = 1$, then all angles coincide.

Eq. (A.1) can be used to compute the bias between two circular variables by substituting x_i by $y_i - x_i$ in Eq. (A.2). In a similar way, the root-mean-square error and standard deviation between two circular variables can be computed.

Since circular data are concentrated on $[0^\circ, 360^\circ]$, and in spite of the analogies with the linear case, it makes no sense to consider a symmetric slope for circular data other than one.

There are several circular analogues of the correlation coefficient, but the most widely used is the one proposed by Fisher and Lee (1983), the so-called *T-linear correlation coefficient*. Given two sets $x = \{x_i, i = 1, \dots, n\}$, $y = \{y_i, i = 1, \dots, n\}$ of circular data, the *T-linear correlation coefficient* between x and y is defined by

$$\rho_T = \frac{\sum_{1 \leq i < j \leq n} \sin(x_i - x_j) \sin(y_i - y_j)}{\sqrt{\sum_{1 \leq i < j \leq n} \sin^2(x_i - x_j) \sum_{1 \leq i < j \leq n} \sin^2(y_i - y_j)}}$$

This statistic satisfies $-1 \leq \rho_T \leq 1$, and its population counterpart (which is not given here but can be seen in Fisher and Lee, 1983) satisfies properties analogous to those of the usual population correlation coefficient for linear data: that is, the population counterpart achieves the extreme values -1 and 1 if and only if the two population variables involved are exactly 'T-linear associated', with the sign indicating discordant or concordant rotation, respectively (see Fisher (1993), p. 146, for these concepts).

For computational ease, we use an equivalent formula for ρ_T , given by Fisher (1993):

$$\rho_T = \frac{4(AB-CD)}{\sqrt{(n^2-E^2-F^2)}\sqrt{(n^2-G^2-H^2)}}$$

where

$$A = \sum_{i=1}^n \cos x_i \cos y_i, \quad B = \sum_{i=1}^n \sin x_i \sin y_i,$$

$$C = \sum_{i=1}^n \cos x_i \sin y_i, \quad D = \sum_{i=1}^n \sin x_i \cos y_i,$$

$$E = \sum_{i=1}^n \cos(2x_i), \quad F = \sum_{i=1}^n \sin(2x_i),$$

$$G = \sum_{i=1}^n \cos(2y_i), \quad H = \sum_{i=1}^n \sin(2y_i).$$

References

Fisher, N.I., 1993. Statistical analysis of circular data. Cambridge Univ. Press, 277 pp.

Fisher, N.I. and A.J. Lee, 1983. A correlation coefficient for circular data. Biometrika, 70, pp. 327-32.

Mardia, K.V., 1972. Statistics of directional data. Academic Press, (London and New York).

Van Os, J. and S. Caires, 2011: How to Carry out metocean studies. Proc. 30th Int. Conf. on Offshore Mechanics and Arctic Eng. (OMAE2011-49066).

Appendix B Delft3D flexible mesh flow module

General

D-Flow is part of the Deltares Delft3D Flexible Mesh (FM) Modelling Suite (Deltares 2024). The D-Flow module can be used to model hydrodynamic conditions by solving the non-linear shallow water equations of unsteady flow and transport phenomena based on the Navier Stokes equations for incompressible free surface flow (Kernkamp et al. 2011; Deltares 2024). The module is designed for flow phenomena where the horizontal spatial and temporal scales are much larger than the vertical scales, such as tidal waves, storm surges or (weakly to non-dispersive) tsunamis. In D-Flow FM, the non-linear shallow water equations are solved in two (depth-averaged, 2DH) or in three dimensions (3D). The 2DH, depth-averaged, calculation is appropriate for many coastal flow model applications, when the water density in the oceans can approximately be regarded as vertically homogeneous. The 3D calculations are needed to accurately simulate vertical gradients in velocity, salinity, temperature and density.

Vertical discretization

D-Flow FM vertical discretization is based on two general vertical grid concepts – 1) the so-called σ -coordinate (terrain-following) and 2) the z-coordinate (geopotential) concept. According to the σ -coordinate concept (σ -layers), a uniform fixed number of layers is present in the entire model domain and the layer interfaces move in time with the varying water level, while the z-coordinate concept (z-layers) uses layer interfaces at fixed vertical positions (Figure B-1a, b; Phillips 1957; Deltares 2024). Furthermore, a combination of both the σ -coordinate and z-coordinate grid concepts can be applied in D-Flow – the so-called z- σ -coordinate concept. According to this concept, z-layers are used in the lower part of the vertical grid (i.e. between the sea bottom and a specified water depth), while in the upper part of the vertical grid (i.e. above the specified water depth) a constant (Figure B-1c) or depth-dependent (Figure B-1d) number of σ -layers is used. This approach prevents the top layer from becoming very thin and a poor vertical grid smoothness in shallow water compared to the case of the σ -coordinate concept.

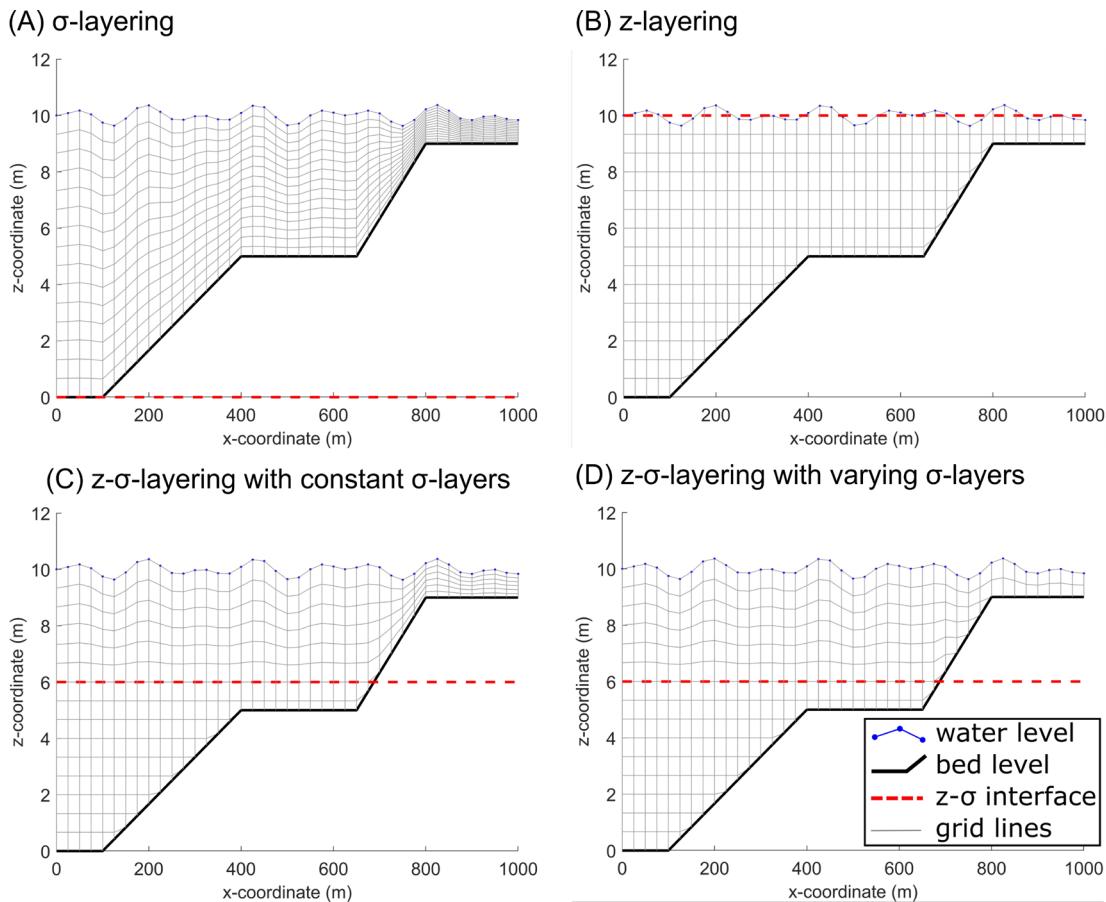


Figure B-1 Illustration of the different vertical grid layering concepts of D-Flow FM including the (A) σ -coordinate concept, (B) z-coordinate concept, (C) z- σ -coordinate concept with a constant number of σ -layers in the upper vertical grid and (D) z- σ -coordinate concept with decreasing σ -layers above a specified water depth (Deltares 2021a).

References

- Deltares 2024: D-Flow Flexible Mesh. D-Flow FM in Delta Shell. User manual, https://content.oss.deltares.nl/delft3d/D-Flow_FM_User_Manual.pdf.
- Kernkamp, H.W.J., A. van Dam, G.S. Stelling and E.D. de Goede, 2011: Efficient scheme for the shallow water equations on un-structured grids with application to the Continental Shelf. *Ocean Dynamics*, 61, 1175–1188, doi: 10.1007/s10236-011-0423-6.
- Phillips, N. A., 1957: A co-ordinate system having some special advantages for numerical forecasting. *Journal of Meteorology*, 14: 184–185.

Appendix B Description of SWAN

General

SWAN is the state-of-the-art third generation shallow water phase-averaging wave model. (Booij et al, 1999) SWAN has been developed at the Delft University of Technology (e.g., Van der Westhuysen, 2010 and Zijlema, 2010) with contributions by Deltares. It computes wave propagation and wave energy evolution efficiently and accurately and it describes several non-linear effects via parameterised formulations. More specifically, SWAN can account for several wave propagation phenomena, including (only the most relevant for the present project mentioned):

- Wave propagation in time and space, shoaling²⁰, refraction²¹ due to current and depth, frequency shifting due to currents and non-uniform depth;
- Wave generation by wind;
- Three- and four-wave interactions²²;
- Energy dissipation by: white-capping, bottom friction and depth-induced breaking.

White-capping is the phenomenon that waves show foam effects at the wave crests due to dissipation of wave energy. It is sometimes called deep-water wave breaking, as opposite to shallow-water wave breaking that can be observed at the beach (depth-induced breaking). Bottom friction causes dissipation of wave energy when the waves are long enough to be influenced by the roughness of the sea bed while propagating. At shallow depths and for longer wave periods bed friction has the largest influence.

Furthermore, SWAN computations can be made on a regular, a curvi-linear grid and a triangular mesh in a Cartesian or spherical co-ordinate system. Nested runs, using input, namely two-dimensional wave spectra, from other (larger scale) models can be made with SWAN.

The SWAN model has been validated and verified successfully under a variety of field cases and is continually undergoing further development. It sets today's standard for nearshore wave modelling.

For more information on SWAN, reference is made to http://swanmodel.sourceforge.net/online_doc/online_doc.htm from where the SWAN scientific/technical documentation and used manual can be downloaded.

In short, the model solves the action balance equation, in Cartesian or spherical coordinates, without any ad hoc assumption on the shape of the wave spectrum. In Cartesian coordinates the equation is

²⁰ Shoaling is the steepening of waves as they approach the coast and reach shallower water. This increases the energy density of the waves, leading to an increase in wave height.

²¹ Refraction is the effect that (non-uniform) bed levels have on the propagation direction of waves.

²² Multiple wave components at different frequencies can interact (in deeper water 4 components, in shallow water 3), leading to a redistribution of wave energy over different wave frequencies. Since it causes energy transfer between components/frequencies these are non-linear processes.

$$\frac{\partial N}{\partial t} + \frac{\partial}{\partial x}(c_x N) + \frac{\partial}{\partial y}(c_y N) + \frac{\partial}{\partial \sigma}(c_\sigma N) + \frac{\partial}{\partial \theta}(c_\theta N) = \frac{S_{tot}}{\sigma},$$

where N is the action density, t is the time, σ is the relative angular frequency, and θ the wave direction. The first term on the left-hand side of the equation above represents the local rate of change of action density in time. The second and third terms represent propagation of action in geographical space. The fourth term represents shifting of the relative frequency due to variation in depth and currents. The fifth term represents depth-induced and current-induced refractions. The quantities c_x , c_y , c_θ and c_σ are the propagation speeds in the geographical x- and y-space, and in the θ - and the σ -space, respectively. The expressions of these propagation speeds are taken from linear wave theory. In the equation above S_{tot} is the energy source term. This source term is the sum of separate source terms representing different types of processes: wave energy growth by wind input, wave energy transfer due to non-linear wave-wave interactions (both quadruplets and triads), and the decay of wave energy due to whitecapping, bottom friction, and depth induced wave breaking. For some source terms more than one formulation is implemented in SWAN, see http://swanmodel.sourceforge.net/online_doc/online_doc.htm.

Drag coefficient

In SWAN the input 10 m wind speeds are converted to surface stress using the drag coefficient. There are two options in SWAN for the drag coefficient parameterization,

1. the drag coefficient from Wu (1982), which corresponds to a roughness of a standard Charnock relation (1955) Charnock with a Charnock parameter of 0.0185 and which is given by the dashed red line in Figure C-2.
2. an approximation of Zijlema et al. (2012) which accounts for a decrease of the drag for wind speeds above 31.5 m/s and which is given by the full red line in Figure C-2.

In this study the approximation of Wu (1982) is applied.

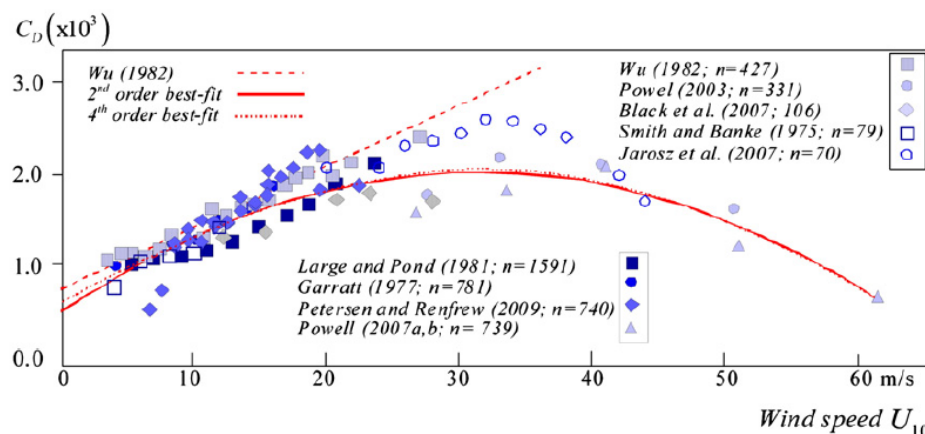


Figure C-2 Observed values of the wind drag coefficient (C_d) from various studies and the weighted best-fit 2nd and 4th-order polynomial (n is the number of independent data points per study). Figure taken from of Zijlema et al. (2012).

Whitecapping

Because it is relevant for the settings that were chosen for the model, a more detail description of the available options for the modelling of wave growth and whitecapping is given.

SWAN's original formulation of dissipation by whitecapping is based on the pulse-based model of Hasselmann (1974), as adapted by the WAMDI group (1988):

$$S_{wcap}(\sigma, \theta) = -\Gamma \bar{\sigma} \frac{k}{k} E(\sigma, \theta),$$

where

$$\Gamma = C_{ds} \left((1 - \delta) + \delta \frac{k}{k} \right) \left(\frac{\bar{s}}{\bar{s}_{PM}} \right)^4,$$

and which can also be written as:

$$S_{wcap}(\sigma, \theta) = C_{ds} \left(\frac{\bar{s}}{\bar{s}_{PM}} \right)^4 \bar{\sigma} \left(\frac{k}{k} \right)^n E(\sigma, \theta),$$

a bar over a variable denotes its mean, k is the wavenumber, and s the wave steepness. The remaining parameters in Γ depend on the wind input formulation that is used and are determined by closing the energy balance of the waves in fully developed conditions.

In SWAN the following options are available:

- For situations in which the formulation recommended Komen et al. (1984) is used,
- $\delta=0$, $n=1$ (default until SWAN version 40.85).
- For situations in which the formulation recommended by Rogers et al. (2003) is used:
- $\delta=1$, $n=2$ (default since SWAN version 40.91).
- For situations in which the formulation recommended by Janssen (1991) is used
- $\delta=0.5$, $n \approx 1.5$.

For $n=1$ the right hand side of the equation above is proportional to $\frac{k}{k}$.

Increasing the parameter n above 1 has the effect of reducing dissipation at lower frequencies while increasing dissipation at higher frequencies, resulting in relatively more low frequency wave energy and larger wave periods. In this study the formulation recommended by Rogers et al. (2003), $\delta=1$ and $n=2$, is applied.

In addition to these formulations based on the expression above, two extra formulations were implemented in SWAN:

- the one suggested by Van der Westhuysen et al., 2007 and referred to as the Westhuysen formulation; which is based on the on the average wave number \bar{k} , and
- the one suggested by Rogers et al. (2012) and referred to as the ST6 (as it is referred to in Source Term package of the WAVEWATCH III® model) formulation.

Numerics

As to SWAN's numerical approach, the integration of the propagation and of the source terms of was implemented with finite difference schemes in all four dimensions (geographical space and spectral space). A constant time increment is used for the time integration. The model propagates the wave action density of all components of the spectrum across the computational area using implicit schemes in geographical and spectral space, supplemented with a central approximation in spectral space. In geographical space the scheme is upwind and applied to each of the four directional quadrants of wave propagation in sequence. Three of such schemes are available in SWAN: a first-order backward space, backward time (BSBT) scheme, a second-order upwind scheme with second order diffusion (the SORDUP scheme) and a second order upwind scheme with third order diffusion (the S&L scheme). The numerical schemes used for the source term integration are essentially implicit. In order to match physical scales at relatively high frequencies and to ensure numerical stability at relatively large time steps, a limiter controlling the maximum total change of action density per iteration at each discrete wave component is imposed.

References

- Aijaz, S., W.E. Rogers and A. V. Babanin, 2016: Wave spectral response to sudden changes in wind direction in finite-depth waters, *Ocean Modelling*, 103, 98-117.
- Booij, N., Ris, R. C., and L. H. Holthuijsen, 1999: A third generation wave model for coastal regions. Part 1. Model description and validation, *J. Geophys. Res.*, 104(C4), 7649-7666.
- Charnock, H., 1955: Wind stress on a water surface. *Q. J. R. Meteorol. Soc.*, 81, 639-640.
- Hasselmann, K., 1974: On the spectral dissipation of ocean waves due to whitecapping, *Bound.-layer Meteor.*, 6, 1-2, 107-127.
- Janssen, P.A.E.M., 1991: Quasi-linear theory of wind-wave generation applied to wave forecasting, *J. Phys. Oceanogr.*, 21, 1631-1642.
- Komen, G.J., S. Hasselmann, and K. Hasselmann, 1984: On the existence of a fully developed windsea spectrum, *J. Phys. Oceanogr.*, 14, 1271-1285.
- Rogers, W.E., P.A. Hwang, and D.W. Wang. 2003: Investigation of wave growth and decay in the SWAN model: three regional-scale applications, *J. Phys. Oceanogr.*, 33, 366-389.
- Rogers, W.E., A.V. Babanin, and D.W. Wang, 2012: Observation-consistent input and whitecapping-dissipation in a model for wind-generated surface waves: Description and simple calculations. *J. Atmos. Ocean. Technol.* 29, 1329- 1346.
- Van der Westhuysen, A. J., 2010: Modeling of depth-induced wave breaking under finite depth wave growth conditions. *J. Geophys. Res.*, 115, C01008, 2010.

Van der Westhuysen, A. J., M. Zijlema and J.A. Battjes, 2007: Nonlinear saturation-based whitecapping dissipation in SWAN for deep and shallow water. *Coastal Engineering*, 54, 151–170.

Zijlema, M., 2010: Computation of wind-wave spectra in coastal waters with SWAN on unstructured grids. *Coastal Engineering*, 57, 267-277.

Zijlema, M., G.Ph. van Vledder and L.H. Holthuijsen, 2012: Bottom friction and wind drag for wave models. *Coastal Engineering*, 65, 19-26

WAMDI group, 1988: The WAM model - a third generation ocean wave prediction model, *J. Phys. Oceanogr.*, 18, 1775-1810.

Wu, J., 1982: Wind-stress coefficients over sea surface from breeze to hurricane, *J. Geophys. Res.*, 87 (C12), 9704-9706.